

RL-TR-95-86
Final Technical Report
May 1995



OPTICAL SWITCHES USING ACTIVE AlGaAs/GaAs RIDGE WAVEGUIDES

University of Minnesota

Sponsored by
Advanced Research Projects Agency
ARPA Order No. 8065



APPROVED FOR PUBLIC RELEASE; DISTRIBUTION UNLIMITED.

19950724 017

The views and conclusions contained in this document are those of the authors and should not be interpreted as necessarily representing the official policies, either expressed or implied, of the Advanced Research Projects Agency or the U.S. Government.

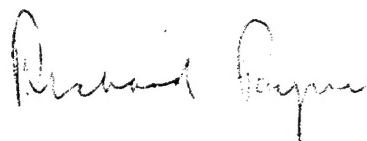
DTIC QUALITY INSPECTED 5

Rome Laboratory
Air Force Materiel Command
Griffiss Air Force Base, New York

This report has been reviewed by the Rome Laboratory Public Affairs Office (PA) and is releasable to the National Technical Information Service (NTIS). At NTIS it will be releasable to the general public, including foreign nations.

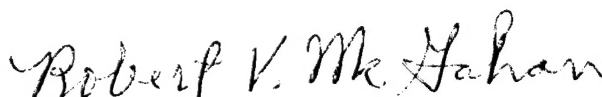
RL-TR-95-86 has been reviewed and is approved for publication.

APPROVED:



RICHARD PAYNE
Project Engineer

FOR THE COMMANDER:



ROBERT V. MCGAHAN
Acting Director
Electromagnetics & Reliability Directorate

If your address has changed or if you wish to be removed from the Rome Laboratory mailing list, or if the addressee is no longer employed by your organization, please notify RL (EROC) Hanscom AFB MA 01731. This will assist us in maintaining a current mailing list.

Do not return copies of this report unless contractual obligations or notices on a specific document require that it be returned.

OPTICAL SWITCHES USING ACTIVE AlGaAs/GaAs RIDGE
WAVEGUIDES

H. Dong
A. Copinath

Contractor: University of Minnesota
Contract Number: F19628-91-K-0044
Effective Date of Contract: 11 June 1991
Contract Expiration Date: 30 August 1994
Short Title of Work: Optical Switches Using Active
AlGaAs/GaAs Ridge Waveguides
Period of Work Covered: Jun 91 - Aug 94

Principal Investigator: A. Copinath
Phone: (612) 625-3054
RL Project Engineer: Dr. Richard A. Soref
Phone: (617) 377-2380

Approved for public release; distribution unlimited.

This research was supported by the Advanced Research
Projects Agency of the Department of Defense and was
monitored by Dr. Richard A. Soref, RL (EROC),
80 Scott Drivem Hanscom AFB MA 01731-2909.

Accession For	
NTIS CRA&I	<input checked="checked" type="checkbox"/>
DTIC TAB	<input type="checkbox"/>
Unannounced	<input type="checkbox"/>
Justification _____	
By _____	
Distribution /	
Availability Codes	
Dist	Avail and/or Special
A-1	

REPORT DOCUMENTATION PAGE

Form Approved
OMB No. 0704-0188

Public reporting burden for this collection of information is estimated to average 1 hour per response, including the time for reviewing instructions, searching existing data sources, gathering and maintaining the data needed, and completing and reviewing the collection of information. Send comments regarding this burden estimate or any other aspect of this collection of information, including suggestions for reducing this burden, to Washington Headquarters Services, Directorate for Information Operations and Reports, 1215 Jefferson Davis Highway, Suite 1204, Arlington, VA 22202-4302, and to the Office of Management and Budget, Paperwork Reduction Project (0704-0188), Washington, DC 20503.

1. AGENCY USE ONLY (Leave Blank)		2. REPORT DATE May 1995		3. REPORT TYPE AND DATES COVERED Final Jun 91 - Aug 94	
4. TITLE AND SUBTITLE OPTICAL SWITCHES USING ACTIVE AlGaAs/GaAs RIDGE WAVEGUIDES				5. FUNDING NUMBERS C - F19628-91-K-0044 PE - 61101E PR - H065 TA - 00 WU - 04	
6. AUTHOR(S) H. Dong and A. Gopinath					
7. PERFORMING ORGANIZATION NAME(S) AND ADDRESS(ES) University of Minnesota Department of Electrical Engineering 200 Union Street, SE Minneapolis MN 55455				8. PERFORMING ORGANIZATION REPORT NUMBER N/A	
9. SPONSORING/MONITORING AGENCY NAME(S) AND ADDRESS(ES) Advanced Research Projects Agency 3701 North Fairfax Drive Arlington VA 22203-1714 Rome Laboratory (EROC) 80 Scott Drive Hanscom AFB MA 01731-2909				10. SPONSORING/MONITORING AGENCY REPORT NUMBER RL-TR-95-86	
11. SUPPLEMENTARY NOTES Rome Laboratory Project Engineer: Dr. Richard A. Soref/EROC/(617) 377-2380					
12a. DISTRIBUTION/AVAILABILITY STATEMENT Approved for public release; distribution unlimited.				12b. DISTRIBUTION CODE	
13. ABSTRACT (Maximum 200 words) We have investigated active optical switches using AlGaAs/GaAs multiple quantum single mode ridge waveguide traveling-wave laser amplifiers. The motivation of this project is to provide the feasibility of the active switches for high-speed optical switching systems in all-optical networks. We have designed a multiple quantum well layer structure and a single mode ridge waveguide, which was used in these active devices. 1x1 (modulator), 1x2 (bifurcation switch), 2x2 (optical crossbar), 1x4 (4-way splitter), and 4x4 (reconfigurable switch) active switches have been designed, fabricated, and tested. In order to analyze and design the ridge waveguide structure, we have developed a numerical technique, based on an integrated finite-difference method combined with the Arnoldi method. The active switches have been fabricated in the Microelectronics Laboratory for Research and Education at the University of Minnesota. The switches have been tested for proper switching functions. A 30 dB extinction ratio and 19 GHz bandwidth of small signal modulation response have been obtained from the 1x1 switch. 28 dB extinction ratio and power splitting have been achieved in the 1x2 test. The 2x2 switch has demonstrated the crossbar switching function. Due to the package problems, the test of the 1x4 and 4x4 switch have not been completed.					
14. SUBJECT TERMS AlGaAs, GaAs, Optical waveguides, Optical switches				15. NUMBER OF PAGES 168	
				16. PRICE CODE	
17. SECURITY CLASSIFICATION OF REPORT UNCLASSIFIED	18. SECURITY CLASSIFICATION OF THIS PAGE UNCLASSIFIED	19. SECURITY CLASSIFICATION OF ABSTRACT UNCLASSIFIED	20. LIMITATION OF ABSTRACT UL		

Table of Contents

Chapter 1.	Introduction.....	1
Chapter 2.	Theory and Design of the Active Optical Switches.....	10
2.1.	Basic Principle of Active Optical Switches.....	11
2.1.1.	Basic Theory of Ridge Waveguide Lasers.....	12
2.1.2.	Basic Theory of Semiconductor Laser Amplifiers.....	18
2.2.	The Active Optical Switch Design.....	21
2.2.1.	Materials for the Active Optical Switches.....	21
2.2.2.	Layer Structure.....	22
2.2.3.	Waveguides.....	31
2.2.3.	Switches.....	39
Chapter 3.	Waveguide Design.....	51
3.1.	Introduction.....	52
3.2.	Discretization.....	54
3.3.	Numerical Technique.....	59
3.4.	Test Examples.....	62
3.5.	Waveguide Design for the Active Optical Switches.....	69

Chapter 4.	Fabrication.....	76
4.1.	Overview of the Fabrication.....	76
4.2.	Ohmic Contacts.....	83
4.3.	Reactive Ion Etching.....	86
4.4.	Airbridge Interconnects by Gold Plating.....	88
4.5.	Antireflection Coating.....	93
Chapter 5.	Measurements.....	98
5.1.	Laser Characterization.....	99
5.1.1.	DC characterization.....	99
5.1.2.	I-V Characterization.....	102
5.1.3.	L-I Characterization.....	105
5.1.4.	Spectrum.....	107
5.1.2.	High Frequency Measurement.....	110
5.2.	Switch Characterization.....	113
5.2.1.	1x1 Switch - Gate Switch/Amplifier/Modulator.....	116
5.2.2.	1x2 Switch.....	120
5.2.3.	2x2 Switch.....	127
5.2.4.	1x4 and 4x4 Switches.....	132

Chapter 6.	Conclusion and Suggestions for Further Studies.....	137
Chapter 7	Personnel and Publications from Project	142
7.1	Personnel	142
7.2	Publications in Journals and Refereed Conferences	142

List of Figures

Figure 2.1.	A diagram of a QW layer structure for a QW laser amplifier.....	19
Figure 2.2.	The diagram of the quantum well layer structure.....	25
Figure 2.3.	Optimization of heights of the barriers between wells in a MQW laser [after Tsang, Ref. 2.32].....	26
Figure 2.4.	Layer structure.....	30
Figure 2.5.	The ridge waveguide structure.....	33
Figure 2.6.	The contour plot for the ridge waveguide.....	35
Figure 2.7.	The doping profile of the layer structure.....	36
Figure 2.8.	A diagram of a half ridge for current spreading effect...	38
Figure 2.9.	The cross section of the switch structure.....	40
Figure 2.10.	The structure of a single mode multiple quantum well ridge waveguide laser.....	41
Figure 2.11.	The structure of an 1×1 switch/modulator.....	42
Figure 2.12.	The structure of an 1×2 switch.....	43
Figure 2.13.	The structure of a 2×2 switch.....	45
Figure 2.14.	Mask layout of a 1×4 switch.....	46
Figure 2.15.	Mask layout of a 4×4 switch.....	47
Figure 3.1.	A cell of the box integration method.....	55

Figure 3.2.	A square waveguide. Normalized propagation constant $B=((\beta/k)^2-\epsilon_0)/(\epsilon_1-\epsilon_0)$ vs. normalized frequency $V=ka(\epsilon_1-\epsilon_0)^{1/2}$, k is the free space wave vector, $a=1\mu\text{m}$, $\epsilon_1=13.1\epsilon_0$	63
Figure 3.3.	The distribution of H_x for the fundamental mode of the square dielectric waveguide.....	64
Figure 3.4.	The distribution of H_x for the first mode of the square dielectric waveguide.....	65
Figure 3.5.	A channel waveguide. Normalized propagation constant $B=((\beta/k)^2-\epsilon_1)/(\epsilon_2-\epsilon_0)$ vs. normalized frequency $V=2b(\epsilon_2-\epsilon_0)^{1/2}/\lambda$, λ is the free space wave length, $a=2b=6\mu\text{m}$, $\epsilon_1=2.13\epsilon_0$, $\epsilon_2=2.25\epsilon_0$	66
Figure 3.6.	The distribution of H_x for the fundamental mode of the channel waveguide.....	67
Figure 3.7.	The distribution of H_x for the first mode of the channel waveguide.....	68
Figure 3.8.	A multiple quantum well single mode ridge waveguide, $w=3\mu\text{m}$, $d=0.9\mu\text{m}$	71
Figure 3.9.	Normalized propagation constant $B=((\beta/k)^2-\epsilon_{\text{clad}})/(\epsilon_{\text{core}}-\epsilon_{\text{clad}})$ vs. normalized frequency $V=dk(\epsilon_{\text{core}}^2-\epsilon_{\text{clad}}^2)^{1/2}$, k is the free space wave vector, ϵ_{clad} is the maximum dielectric constant in the clad layers, the ϵ_{core} is the maximum dielectric constant in the guided region, and d is the thickness of the core.....	72
Figure 3.10.	The distribution of H_x for the fundamental mode of the quantum well single mode waveguide.....	73
Figure 4.1.	The device structure corresponding to the fabrication flow chart.....	78

Figure 4.2.	Mask layout for p-type and n-type ohmic contacts, and ridge etching.....	79
Figure 4.3.	Fabrication flow chart.....	81
Figure 4.3.	continued.....	82
Figure 4.4.	The alloyed ohmic contact test pattern for the p-type (top) and n-type (button).....	85
Figure 4.5.	Etched ridge by RIE system.....	88
Figure 4.6.	Basic concept of gold plating.....	90
Figure 4.7.	Airbridged connect by gold plating.....	92
Figure 4.8.	Top view of the ridge waveguide laser.....	93
Figure 4.9.	Measured reflectivity vs. wavelength.....	96
Figure 5.1.	Test setup for the ridge waveguide laser diode.....	101
Figure 5.2.	Measured current through the ridge waveguide laser diode vs. forward bias voltage across the diode.....	102
Figure 5.3.	Measured currents through the laser diode vs. the reverse bias voltage across the diode.....	104
Figure 5.4.	Measured light power emitted from the laser diode vs. pulse current through the laser.....	105
Figure 5.5.	Measured light power emitted from the laser diode vs. CW current through laser.....	106
Figure 5.6.	Optical spectrum of the ridge laser.....	108
Figure 5.7.	Near field mode of the laser diode at $I = 1.5I_{th}$	109

Figure 5.8.	Equivalent circuit model for the diode.....	110
Figure 5.9.	Measured S_{11} parameter vs. frequency from 45MHz to 26.5GHz for the laser diode at $I = 1.33I_{th}$	111
Figure 5.10.	Small signal modulation response of the ridge waveguide laser at $1.1 I_{th}$ (solid line), $1.5 I_{th}$ (dash line) and $1.8 I_{th}$ (dotted line).....	113
Figure 5.11.	Setup of DC and RF characterization for optical switches.....	114
Figure 5.12.	A top view of 1×1 , 1×2 , 2×2 , 1×4 and 4×4 switches....	115
Figure 5.13.	Measured light power emitted from the 1×1 switch vs. pulse current at 1KHz with 1% duty cycle through the device.....	117
Figure 5.14.	Power gain/attenuation as a function of bias current for a 500 micron long 1×1 optical switch/modulator.....	118
Figure 5.15.	Small signal frequency response of a 1×1 switch/modulator biased at 60 mA.....	119
Figure 5.16.	Diagram of 1×2 switch test setup.....	121
Figure 5.17.	Output gain of the 1×2 switch with DC arm pulsed-biased (1KHz and 10% duty cycle) vs. the (CW) current through one of the switch arms. The solid line is for $I = 100$ mA, and dashed line is for $I = 120$ mA.....	122
Figure 5.18.	Output gain of the 1×2 switch with CW biased DC arm vs. the (CW) current through one of the switch arms. The solid line is for $I = 60$ mA, dashed line is for $I = 80$ mA, and dotted line is for $I = 100$ mA.....	123

Figure 5.19.	Output gain of the 1×2 switch vs. the current through one of the switch arms and DC arm simultaneously.....	124
Figure 5.20.	Top view of the 1×2 switch with biased DC arm and biased/unbiased one of the switch arms.....	125
Figure 5.21.	The end view from output guides of the 1×2 switch with DC arm biased at 100 mA pulsed and 40 mA biased/unbiased switch arms.....	126
Figure 5.22.	A packaged 2×2 switch with a 1×2 switch together....	128
Figure 5.23.	Measurement diagram for 2×2 switches.....	129
Figure 5.24.	Relative output power vs. current through the switch arms of parallel section and cross section, respectively, for DC arms biased at $I = 100$ mA and 150 mA. The top two curves are for parallel switch arms, and low two are for cross switch arms.....	130
Figure 5.25.	Top view of a 2×2 switch for parallel through and exchange routine switching.....	131
Figure 5.26.	Diagram of signal distribution for the test of 1×4 and 4×4 switches.....	133
Figure 5.27.	Packaged 1×4 and 4×4 switches.....	134
Figure 5.28.	Wire bonded 1×4 and 4×4 switches.....	134
Figure 5.29.	Top view of the 1×4 switch with a proper bias.....	135
Figure 5.30.	Top view of the 4×4 switch with a proper bias.....	135

CHAPTER 1

INTRODUCTION

For many years, cables and free space radio links were the standard means of signal transmission and processing. This dominance has been challenged by optical fiber systems. Since lasers provided a stable source of coherent light, the optical fiber waveguides were developed to carry high data rate signal with low attenuation. These optical fiber systems have several advantages over the conventional cable and radio systems, and some of these are: immunity from electromagnetic interference, freedom from electrical short circuits or ground loops, safety in combustible environment, security from tapping, low-loss transmission, large bandwidth, small size, light weight, and inexpensive systems. During the last 15 years, these communication systems with semiconductor laser diodes used as the optical source, and optical fibers used as the transmission medium have improved enormously. Signals are transmitted point-to-point over optical fibers, coded in pulses of light. To provide high-speed and broadband service of optical fiber communications, high performance switch systems are required.

Optical switches can be categorized into two types, passive and active. In passive optical switches, the optical signals do not experience any signal gain, but in an active switches, the signals may be amplified.

Passive optical switches have been studied on LiNbO_3 , III-V semiconductors, and polymers. Lithium niobate has excellent optical and electrooptic properties. A 40 GHz bandwidth [1.1,1.2] and 50 GHz bandwidth [1.3] had been obtained on LiNbO_3 modulator by employing different velocity matching techniques, respectively. In the last two decades, studies of switches and modulators in LiNbO_3 have resulted in commercially-available high-performance [1.4]. In III-V semiconductors, the microwave-optical velocity mismatch is smaller than in LiNbO_3 , and therefore, the switches and modulators on III-V semiconductors potentially have large bandwidth and excellent figures of merit. Velocity matched modulators on GaAs beyond 20 GHz had been demonstrated [1.5-1.7]. A bandwidth greater than 100 GHz has been achieved in a velocity-matched GaAs modulator with 288 volts of modulation voltage [1.8]. The devices on polymers have inherent velocity-matching, and have been shown with bandwidths greater than 40 GHz [1.9]. The optical switching functions on the three different types of the materials for passive optical switches are achieved by varying the waveguide effective refractive index. This results long coupling lengths, usually about 1 centimeter, and requires high fabrication accuracy. Losses in passive optical switches is a major problem, which limits the switch performances. The passive switches require high switching voltage, usually 15 V to 30 V. Other types of switches based on the quadratic electro-optical effect require switching voltage, but loss remains a problem.

To overcome some of the above problems, active optical switches may be utilized. The switches are based on integrated semiconductor laser amplifiers, and appear to offer superior performance. The signal gain and loss are controlled by the injection current, and the optical signal is switched directly. With injected current above transparency, the light signal is amplified, and with zero or negative bias, the signal is absorbed. The advantages of these active optical switches are simple switch structure, compact physical size, zero loss or signal gain, low crosstalk, nanosecond switching time, low insertion loss, large bandwidth with high isolation [1.10, 1.11], equal power in point-to-point, and multipoint operation with nonblocking architecture. The amplifiers in the active switches are used for switching, amplification, and monitoring.

Fabry-Perot and traveling wave semiconductor laser amplifiers are suitable for use as ON/OFF switches due to their large extinction ratio and nanosecond switching time [1.10, 1.11]. The Fabry-Perot semiconductor laser amplifier is basically a conventional laser diode which is biased just below the threshold level. Although the amplifiers are easy to fabricate, the optical gain is very sensitive to variations in amplifier temperature and input optical frequency [1.10]. Thus, they require very careful stabilization of temperature and injection current. Traveling-wave semiconductor laser amplifiers have been used more widely, because they have a large optical bandwidth, high saturation power, and low polarization sensitivity [1.11]. However, they have a lower signal gain, and have higher spontaneous emission noise than Fabry-Perot semiconductor laser amplifiers, because of their low facet

reflectivity. In addition they are difficult to fabricate because high-quality reflection coatings are needed on the facets. Nevertheless, the large optical bandwidth, high saturation output power, and stable operation of the traveling-wave semiconductor laser amplifiers make them preferable as active optical switches.

Active optical switches using semiconductor laser amplifiers have been studied for several years by many research groups around world [1.12-1.24]. Low loss hybrid as well as monolithic space switches and switches with gain have been presented [1.12-1.24]. The size of the switch matrix has been raised up to 4×4 and 1×16 [1.14-1.24]. The improvement in the performance of the active optical switches has progressed dramatically. Two recent results on monolithically integrated 4×4 active switches have been reported on InGaAsP/InP laser amplifiers and AlGaAs laser amplifiers [1.25-1.26], which represent the latest development in active optical switches. Gustavsson *et. al.* presented monolithic integrated 4×4 InGaAs/InP laser amplifier gate switch arrays [1.25], with a nonblocking tree-structure. 16 amplifier gates are used in the interconnection region to control the switch state and four booster amplifiers are included immediately the inputs, and before the outputs. The switches are fabricated in the InGaAs/InP material system, and the fabrication process involved regrowth. Balestra *et. al.* demonstrated a monolithic semiconductor active waveguide optical switch on GaAs semiconductor [1.26]. A traveling-wave semiconductor laser amplifier was used as an optical gain/absorption switch. A monolithic 4×4 optical crossbar switch based on these amplifiers was fabricated. This device is

completely nonblocking can be operated in either a point-to-point or broadcast mode. It consists of ridge waveguides, etched-facet turning mirrors, and etched T-branches laid out into an all-optical-path network. This device was fabricated from a single GaAs quantum well/AlGaAs GRINSCH epitaxial structure on an N+ GaAs substrate.

In this report, we have investigated monolithic active optical switches using GaAs multiple quantum-well traveling-wave semiconductor laser amplifiers on a semi-insulating substrate. 1×1 , 1×2 , 2×2 , 1×4 , and 4×4 switches were designed, fabricated, and tested in Department of Electrical Engineering in University of Minnesota. The 1×1 , 1×2 , and 2×2 switches were studied as the basic elements for high dimensional switch structures. The 1×4 and 4×4 switches have also been constructed with these basic building blocks. The 1×1 switches performs as gate switch, a traveling-wave amplifier, and a modulator. The 1×2 switches are typically branch switches for zero loss power splitting. The 2×2 switch is the crossbar switch, and may form any higher dimensional switch structure. Multiple quantum well layer structures were used in these active switches, for high gain and short device length. The semi-insulating substrate made the devices easy integrable with other electronic or optoelectronic devices.

The organizations of this report is as follows: Chapter 2 presents the basic principle of the active optical switches and the design of our active optical switches, which includes choice of materials, layer structure design, waveguide design and switch design, and theory of the semiconductor lasers and switches. In Chapter 3, the waveguide

numerical analysis and design are developed for this project are discussed. The fabrication techniques are presented in Chapter 4. The measurement of the active optical switches are discussed in Chapter 5, and Chapter 6 provides conclusions and suggestion for further studies.

References

- [1.1] S. K. Korotky, G. Eisenstein, R. S. Tucker, J. J. Veselka, and G. Raybon, "Optical intensity modulation to 40 GHz using a waveguide electrooptic switch," *Appl. Phys. Lett.*, vol. 50, no. 23, pp. 1631-1633, 1987.
- [1.2] D. W. Dolfi and M. Nazarathy, "40 GHz electro-optic modulator with 7.5 V drive voltage," *Electronics Lett.*, vol. 24, pp. 528-529, 1988.
- [1.3] D. W. Dolfi and T. R. Ranganath, "50 GHz velocity-matched broad wavelength LiNbO₃ modulator with multimode active section," Topic meeting on Integrated Photonics Research, New Orleans, Louisiana, April 13-16, 1992.
- [1.4] R. L. Jungeman, C. A. Johnsen, D. J. McQuate, K. Salomaa, M. P. Zurakowski, R. C. Bray, G. Conrad, D. Cropper, and P. Hernday, "High-speed optical modulator for application in instrumentation," *J. Lightwave Tech.*, vol. 8, pp. 1363-1370, 1990.
- [1.5] R. G. Walker, "High-speed III-V Semiconductor Intensity Modulators," *IEEE J. of Quantum Elect.*, vol. 27, no. 3, march 1991.
- [1.6] S. Y. Wang, S. H. Lin, and Y. M. Houn, "GaAs traveling-wave polarization electro-optic waveguide modulator with bandwidth in excess of 20 GHz at 1.3 μ m," *Appl. Phys. Lett.*, vol. 51, pp. 83-85, 1987.
- [1.7] R. G. Walker, I. Bennion, and A. C. Carter, "50 Ω GaAs/AlGaAs traveling-wave modulator with bandwidth exceeding 25 GHz," *Elect. Lett.*, vol. 25, pp. 1549-1550, 1989.
- [1.8] J. Nees, S. Williamson, and G. Mourou, "100 GHz traveling-wave electro-optic phase modulator," *Appl. Phys. Lett.*, vol. 54, no. 20, pp. 1962-1964, 1989.
- [1.9] C. C. Teng, M. G. Scatturo, and T. K. Findakly, "Very high speed polymeric external modulator with more than 40 GHz of 3-dB electrical bandwidth and low drive voltage," Topic meeting in Integrated Photonics Research, paper TuG2, 1992.
- [1.10] M. Ikeda, "Laser diode switch," *Electron. Lett.*, vol. 17, pp. 899-900, 1981.
- [1.11] M. Ikeda, "Optical properties for an antireflection-coated LD optical switch," *Electron. Lett.*, vol. 19, pp. 826-828, 1983.

- [1.12] M. Kobayashi, A. Himeno, H. Terui, "Guided-wave optical gate matrix switch," Proc. IOOC-ECOC '85, post-deadline paper, pp.73-76, 1985.
- [1.13] M. Ikeda, "Proposal of laser diode integrated-optical matrix switches," Trans. IECE Japan, vol. E 69, pp.1072-1074, 1986.
- [1.14] M. Ikeda, O. Ohguchi, K. Yoshino, "Monolithic LD optical matrix switches," Proc. 13th European Conf. on Optical communication, pp. 227-230, 1987
- [1.15] S. Oku, K. Yoshino, M. Ikeda, "Design and performance of monolithic LD optical matrix switches," Proc. Photonic Switching, pp. 98-100, 1990.
- [1.16] I. H. White, J. J. S. Watts, J. E. Carroll, C. J. Armistead, D. J. Moule, J. A. Champelovier, "InGaAsP 400×200 μm active crosspoint switch operating at 1.5 μm using novel reflective Y-coupler components", Electron. Lett. vol. 26, pp. 617-618, 1990.
- [1.17] H. Terui, T. Kominato, M. Kobayashi, "Lossless 1×4 laser diode optical gate switch", J. Lightwave Technol. vol. 9, pp. 1518-1522, 1991.
- [1.18] M. Janson, L. Lundgren, A.-C. Morner, M. Rask, B. Stoltz, M. Gustavsson, L. Thylen, "Monolithic integrated 2×2 InGaAsP/InP laser amplifier gate switch arrays", Electron. Lett. vol. 28, pp. 776-778, 1992.
- [1.19] J. Singh, I. D. Henning, P. S. Mudhar, M. A. Fisher, S. Perrin, D. A. H. Mace, M. J. Adams, "A novel twin-ridge-waveguide optical amplifier switch", IEEE Photo. Technol. Lett., vol. 4. pp. 128-129, 1992.
- [1.20] J. D. Burton, P. J. Fiddymont, M. J. Robertson, P. Sully, " Low loss monolithic 2×2 laser amplifier gate switch matrix", Proc. 13th IEEE International Semiconductor Laser Conf., pp.128-129, 1992.
- [1.21] M. G. Young, U. Koren, B. I. Miller, M. A. Newkirk, M. Chien, M. Zirngibl, C. Dragone, B. Glance, T. L. Koch, B. Tell, K. Brown-Goebeler, G. Taybon, "A 1×16 photonic switch operating at 1.55 micron wavelength based on optical amplifiers and a passive optical splitter", OSA Proc. Optical Amplifiers and their Applications, post-deadline paper, pp. 43-46, 1992.
- [1.22] M. Gustavsson, B. Lagerstrom, L. Thylen, M. Janson, L. Lundgren, A.-C. Morner, M. Rask, B. Stoltz, "Monolithically integrated 4×4 InGaAsP/InP laser amplifier gate switch arrays",

- OSA Proc. Optical Amplifiers and their Applications, post-deadline paper, pp. 38-42, 1992.
- [1.23] D. A. O. Davies, P. S. Mudhar, M. A. Fisher, D. A. H. Mace, M. J. Adams, "Integrated lossless 1 to 4 optical splitter/combiner operating at 1.55 μm ", OSA Proc. Optical Amplifiers and their Applications, post-deadline paper, pp. 43-46, 1992.
 - [1.24] D. K. Probst, L. G. Perrymore, B. C. Johnson, R. J. Blackwell, J. A. Priest, and C. L. Balestra, "Demonstration of an integrated, active 4 \times 4 photonic crossbar," IEEE Photonics Tech. lett., vol. 4, No. 10, p. 1139 (1992).
 - [1.25] M. Gustavsson, W. van Berlo, L. Lundgren, and M. Janson, "Monolithic integrated 4 \times 4 InGaAsP/InP laser amplifier gate switch arrays", OSA CLEO, paper IO1.2, 1993.
 - [.26] C. L. Balstra, R. J. Blackwell, B. C. Johnson, and L. G. Perrymore, "Monolithic semiconductor active waveguide optical switch," SPIE Conf. on Photonics for Space Environments 1953-18, Orlando (1993).

CHAPTER 2

THEORY AND DESIGN OF THE ACTIVE OPTICAL SWITCHES

In Chapter 2, we briefly present the principle of the active optical switches in Section 2.1, which include the theories of the semiconductor laser diode, and the semiconductor laser amplifiers in Sections 2.1.1 and 2.1.2, respectively. We then discuss the design of our active optical switches which use AlGaAs/GaAs traveling-wave laser amplifiers with a single mode ridge waveguide on a semi-insulating substrate in Section 2.2. The design of active optical switches involves the choice of semiconductor materials for the active switches discussed in Section 2.2.1, the design of quantum well structure for the active regions, in Section 2.2.2, design of the ridge waveguide, in Section 2.2.3, and the switch structure design for 1×1 , 1×2 , 2×2 , 1×4 , and 4×4 switches, in section 2.2.4. The switch structures, which considered in this report, are 1×1 , 1×2 , 2×2 , 1×4 , and 4×4 structures. The 1×1 structure is an optical gate switch/amplifier/modulator, the 1×2 , and 1×4 structures are for the signal splitting with negligible loss or gain. The 2×2 switch is a crossbar switch. The 4×4 switch is a four dimensional optical switch matrix composed of five 2×2 crossbar switches.

2.1. Basic Principle of Active Optical Switches

The switches we consider here are two-port structures with a low transmission state which is the 'off' state and a high transmission state which is the 'on' state, and the ratio of the corresponding states defines the extinction ratio. The active optical switches we have built are based on semiconductor waveguide laser amplifiers. The semiconductor laser amplifier used in our switches is a traveling-wave design, which is composed of a laser with antireflection coatings on both facets. The reflectivity of the Fabry-Perot cavity has to be less than 1% in order to obtain the gain stability [2.1]. The low reflectivity also results in high saturation output power and low polarization sensitivity [2.2].

The active region of the amplifier is composed of AlGaAs/GaAs separate-confinement multiple quantum wells embedded in heterostructure layers as cladding. The quantum wells of GaAs are separated by three Al_{0.2}Ga_{0.8}As barrier layers, with the quantum wells which form core. The wavelength of the optical signal is chosen to be within the spectrum of the quantum well structure, so that the light can be absorbed by the quantum well structure along the propagation direction, and this corresponds to the off-state of the switches. Since the separate confinement layers and cladding layers have wider bandgap than the quantum wells, the light energies are required to be less than the energy of these bandgaps, which results in negligible absorption loss of the optical signals. With current drive through the quantum wells, at or above transparency, population inverse in quantum wells occurs, and the

input optical signal experiences transparency, i.e. negligible loss, corresponding to the on-state of the switch. With further increase in current drive, the optical signals experience gain from the quantum wells, and the gain value depends on the drive level above transparency. The amplifier can also be used to monitor the optical signal without bias or with reverse bias.

A single transverse mode ridge waveguide structure is employed in these switches to eliminate the mode dispersion. The optical signals are confined and guided by the ridge waveguide. This waveguide with the quantum well layer structure determines the confinement factor, which is the ratio of signal power guided by the quantum wells to the total power the signal.

All our active optical switches are composed of traveling-wave laser amplifiers, with a single mode ridge waveguide structure on a semi-insulating substrate. All the ridges are active, and each switch arm on the waveguide is individually biased.

In the following two sections, the basic principles of a semiconductor lasers and semiconductor laser amplifiers are presented respectively. The concepts of laser and laser device physics are presented in references [2.3, 2.4] in detail and rigor.

2.1.1. Basic theory of ridge waveguide lasers

Rate equations can adequately describe the behavior and some import limitations of a laser diode. Expression of the rate equations may

be at various levels of complexity. We describe the rate equation of our lasers based on their structure, so that the expressions are simple, without losing the necessary accuracy. The ridge waveguide in our lasers supports only the fundamental mode, which is a single mode, and the Fabry-Perot cavity is uniform with two facets. The current injection is assumed uniform over the whole laser, and the variation of carrier density and carrier diffusion effects in the lateral and transverse directions are ignored. The photon and carrier variation along the cavity length are also ignored. Under these assumptions, the rate equations which govern the photon and carrier densities inside the laser medium can be expressed as follows [2.4]:

$$\frac{dS}{dt} = (G - \gamma) S + R_{sp} \quad (2.1)$$

$$\frac{dN}{dt} = \frac{I}{q} - \gamma_e N - G S \quad (2.2)$$

where N is the carrier density, S is the photon density, I is the current through the junction, G is the gain, R_{sp} is the rate at which spontaneously emitted photons are added to the intracavity photon population, q is electron charge, γ_e is the carrier-recombination rate which defines the spontaneous carrier lifetime τ_n , $\gamma_e = 1/\tau_n$, and γ is the photon decay rate, given by

$$\gamma = v_g(\alpha_{int} + \alpha_m) = 1/\tau_p \quad (2.3)$$

where v_g is the group velocity, α_{int} and α_m are the internal loss in the cavity and mirror loss respectively, and τ_p is the photon lifetime.

An advantage of semiconductor lasers is the convenience of direct modulation of the light intensity. The modulation may be simply carried out by modulating the current through the laser diode. The following part will concentrate on the high speed modulation properties of the single mode lasers. The derivations indicate the parameter effecting the bandwidth of frequency response for a laser diode.

The modulation response can be analyzed by small signal approach, i.e. the steady-state values of N and S are perturbed by a small amount δS and δN respectively. The rate equations (2.1) and 2.2) are linearized by neglecting the quadratic and higher powers of δS and δN , and expressed as follow:

$$\frac{d\delta S}{dt} = \Gamma_p \delta S + (G_N S + \frac{\partial R_{sp}}{\partial N}) \delta N \quad (2.4)$$

$$\frac{d\delta N}{dt} = -\Gamma_N \delta N - (G + G_p S) \delta S \quad (2.5)$$

where

$$\Gamma_p = R_{sp}/S - G_p S \quad (2.6)$$

$$\Gamma_N = \gamma_e + N (\partial \gamma_e / \partial N) + G_N S \quad (2.7).$$

The gain $G(N, S)$ is approximated by

$$G(N, S) \approx G + G_N \delta N + G_P \delta S \quad (2.8)$$

where $G_N = \partial G / \partial N$ and $G_P = \partial G / \partial S$. The assumption of sinusoidal variation for δS and δN is made:

$$\delta S(t) = \delta S_0 \exp(j\Omega_R t) \quad (2.9)$$

$$\delta N(t) = \delta N_0 \exp(j\Omega_R t) \quad (2.10)$$

where δS_0 and δN_0 are the perturbation values. Substituting equations (2.8), (2.9), and (2.10) into equations (2.4) and (2.5), The solution of the linearized rate equations (2.4) and (2.5) for the angular frequency of relaxation oscillations is:

$$\Omega_R = \left[(G + G_P S) \left(G_N S + \frac{\partial R_{sp}}{\partial N} \right) - \frac{(\Gamma_N - \Gamma_P)^2}{4} \right]^{1/2} \quad (2.11)$$

In equation (2.11), note that the $GG_N S$ dominates by several orders of magnitude so that a good degree of approximation to Ω_R is follow:

$$\Omega_R = (GG_N S)^{1/2} \quad (2.12).$$

It is desirable for this approximation to be expressed in terms of the device current for the practical purpose. The steady-state of S is obtained from equation (2.2) by setting the time derivative to zero,

$$S = (I - I_{th}) / (qG) \quad (2.13)$$

where $I_{th} = q\gamma_e N_{th}$. Substituting equation (2.13) into equation (2.12), we then obtain:

$$\Omega_R = \left[\frac{G_N (I - I_{th})}{q} \right]^{1/2} \quad (2.14)$$

where the G_N can be expressed as

$$G_N = \Gamma v_g g_0 / V \quad (2.15)$$

where g_0 is differential gain and V is the active volume. Now the relaxation frequency can be written in terms of photon life time, carrier lifetime, differential gain, and the device current as

$$\Omega_R = \left[\frac{1 + \Gamma v_g g_0 N_0 \tau_p}{\tau_n \tau_p} \left(\frac{I}{I_{th}} - 1 \right) \right]^{1/2} \quad (2.16)$$

where the N_0 is the transparency value of the carrier density.

With low parasitics of a laser device structure and package, the relaxation frequency of a laser diode is given by equation (2.16). This

expression clearly indicates that the bandwidth of a laser can be increased by one or all of the following means: increasing the differential gain constant, decreasing the photon life time, or operating the laser diode at high device current.

The differential gain constant is a measure of how much the gain increases if the carrier density is increased, and depends critically on the density of states at the quasi-Fermi levels of the electrons and holes. The differential gain constant in a quantum well can be a factor of four larger than in bulk material due to the low dimensional density of states in a quantum well [2.6]. It can be further increased by doping the active region into a p-type region [2.7]. Low temperature [2.8] operation of a laser diode also increases the bandwidth because of a sharpened carrier distribution and an increase of the differential gain constant.

Photon lifetime can be shortened by reducing the mirror reflectivity or reducing the cavity length. A short photon lifetime increases the gain which is necessary to achieve lasing action. Since the maximum gain which can be obtained from one quantum well is limited, multiple quantum wells in the active region are necessary. A short photon lifetime also increases the threshold current. The power dissipated in the diode and resulting thermal effects ultimately limits the practical lower value of the photon lifetime [2.9]. This limit could be lowered through efficient heat-sinking or by restricting operation of the laser diode to a pulsed mode [2.10].

2.1.2. Basic theory of semiconductor laser amplifiers

The basis of our active optical switches is a AlGaAs/GaAs laser amplifier. When the devices are biased, they amplify an external optical signal, which propagates along the active area. Semiconductor laser amplifiers are basically divided into two types. The simplest class of device is the Fabry-Perot laser amplifier (FPLA), which is merely a Fabry-Perot laser that is operated below threshold. FPLA has an implicit filtering effect from the Fabry-Perot cavity. However, the positions of its passbands are carrier and temperature dependent [2.11] requiring sophisticated control equipment to maintain tuning to the input signal. If the facets of FPLA are antireflectance coated, then a second class of device is obtained, i.e. traveling-wave laser amplifier (TWLA). TWLAs have a nonresonant cavity, and so provide a virtually flat frequency response, large optical bandwidth, high saturation power, and low polarization sensitivity. Therefore, TWLAs are promising device for the optical communication systems.

Theoretical characterization of semiconductor laser amplifiers have been studied for two decades. In this section we are not going to overview all these studies of amplifiers, we only focus on multiple quantum (MQW) well laser amplifiers and study the dynamic behavior of the amplifiers by a simple model. MQW amplifiers have large saturation power [2.12, 2.13] and a rapid gain recovery process [2.14], which is attributed to replenishment of carriers in the quantum wells via diffusion of carriers stored in the barrier and cladding regions [2.14, 2.15]. The

dynamic response of the amplifier is determined by the gain recovery process.

Figure 2.1 shows a layer structure of a MQW laser amplifier. Three QWs are separated by two barrier layers, and embedded into separate confinement heterostructure (SCH) layers capped by two cladding layers. When the bias current is large enough, carriers are present not only in the QWs, but also in the barrier and separate-confinement regions. These carriers stored in the separate-confinement barriers which function as the carrier storage reservoirs [2.14-2.16] can rapidly replenish, via diffusion, carriers removed from the QWs by stimulated emission caused by the input optical signal.

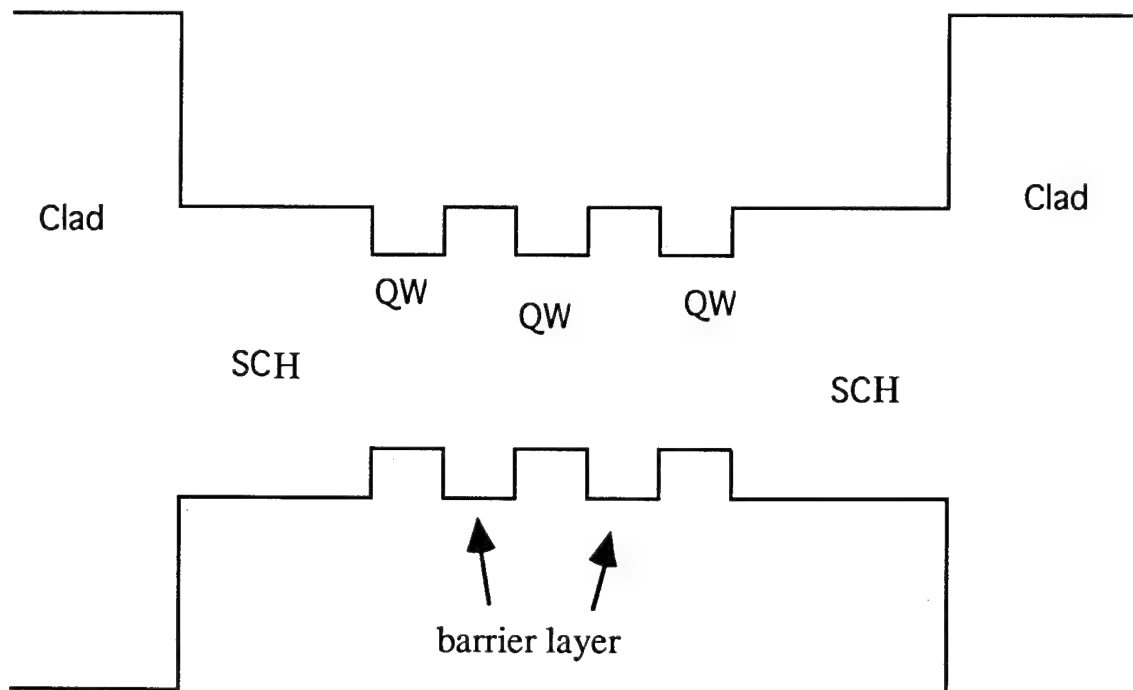


Figure 2.1. A diagram of a QW layer structure for a QW laser amplifier.

A simple rate equation model [2.17] is applied to the amplifier as following:

$$\frac{dN_b}{dt} = \frac{I}{e} - \frac{N_b}{\tau_b} - k_{Dl} (N_b - \eta N_w) \quad (2.17)$$

$$\frac{dN_w}{dt} = r (k_{Dl} (N_b - \eta N_w) - \frac{N_w}{\tau_w} - g S N_w) \quad (2.18)$$

where N_w and N_b are numbers of carriers in the QWs and the total number of carriers in barrier regions, respectively. τ_b and τ_w are the nonradiative recombination time in the barrier and the wells respectively. I is the injected current, e is electron charge, k_D is the rate constant of diffusion in the barriers to replenish carrier into the gateway states (which are the states in quantum wells occupying energies above the bandgap of the barrier material.), S is the photon density incident on the amplifier, g is the differential gain. The η is the steady-state ratio of carrier number, N_b^0 , in the barriers to that, N_w^0 , in the wells in the absence of an input optical signal, and given by

$$\eta = N_b^0 / N_w^0 \quad (2.19)$$

and r is given by

$$r = \rho / (\rho + 1) \quad (2.20)$$

where r is the ratio of steady-state carrier number in the wells to the gateway states, and l is the ratio of width of the gateway to that the barriers and cladding and given by

$$l = L_G/L_B \quad (2.21)$$

where L_G and L_B are the width of the barrier and cladding layers.

When the input signal is step function at $t=0$, then the solution of equations (2.17) and (2.18) is

$$N_w(t) = N_w^0 (A_0 + A_f \exp(-t/t_f) + A_s \exp(-t/t_s)) \quad (2.22)$$

where $t_f = (k_D S r \eta)^{-1}$ and $t_s \approx \tau_b$ are the fast and slow time constants for gain recovery, and A_f and A_s are the associated amplitudes [2.14, 2.15]. Both of the time constants have to be measured from experiments, usually are in picosecond ranges [2.18]. A_0 is the steady-state carrier density ratio achieved for input signal S . The equation (2.22) describe the replenishment process in the amplifier.

2.2. The active optical switch design

2.2.1 Materials for the active optical switches

Active optoelectronic devices may only be fabricated in the semiconductor materials which are capable of generating light. This

limits the choice of the materials to direct band gap semiconductors, and currently, these are the III-V and II-VI compound semiconductors. Considerable amount of research in optoelectronic devices has been performed on AlGaAs/GaAs devices because the lattice mismatch between the two compounds is small. At room temperature, the lattice mismatch between GaAs and $\text{Al}_x\text{Ga}_{1-x}\text{As}$ ($0 < x \leq 1.0$) is less than 0.15% [2.19], which is insignificant compared to the concentration of undesirable interface states. AlGaAs/GaAs have excellent optical properties, and the material growth of these materials are well developed in the molecular beam epitaxy (MBE) system and metal organic chemical vapor deposition (MOCVD) system.

In this report, we adopted AlGaAs/GaAs semiconductors for the active optical switches. The main reason for this choice is that the fabrication technique is mature, and hence the demonstration of the idea for the active optical switches is simple. The wavelength which we use in our active optical switches is approximately 0.86 μm .

2.2.2 Layer Structure

Since our active optical switches are based on semiconductor laser amplifiers, the aim of our design for the layer structure is to design a high-speed and ultralow threshold quantum well structure for a AlGaAs/GaAs quantum well laser. The critical factors besides low threshold current for the design of the laser are high differential gain for

larger bandwidth, short cavity for a small photon life time, and tight optical mode confinement for higher photon densities.

An AlGaAs/GaAs separate confinement multiple quantum well layer structure was used in our active optical switches. The use of QW as the active layer has several advantages compared with conventional heterostructure active layers as follow [2.20]. The wavelength emitted may be reduced by changing the width of quantum well. The low dimensional structure of the QW structures offers much lower current density for inversion populations for the transparency condition when compared with the conventional heterostructure devices. This results in lower current drive for transparency condition of the QW structure, and higher gain, and lower temperature sensitivity. Therefore, the QW structure is more efficient, and provides higher differential gain, and a faster switching rate from the transparency to attenuation. The differential gain represents how quickly the gain responds to changes in the total carrier density, which is related to the ultimate modulation speed of a QW. The quantum well structure also provides gain with less change in refractive index than bulk structures because of lower drive current, which results in lower chirping. The QW structure has a narrower linewidth than bulk structures because of lower internal loss and lower broadening condition. The narrow linewidth improves the coherency of the emitted light. The quantum well structure also possesses the larger modulation bandwidth and superior mode stability.

The superior gain properties of QW structures are the biggest advantage that QW layer designs offer. The difference between the

single quantum well (SQW) and multiple quantum well (MQW) structures is of particular interest. The lowest laser threshold current density has been achieved in SQW lasers [2.21]. However, the lowest threshold carrier density for a QW structure can be obtained in a MQW structure with maximum optical confinement. Thus, the highest differential gain may be obtained in the MQW, which determines the bandwidth of the switches, and the superior properties of QW gain can be obtained in such a structure. Although Auger recombination and nonuniformity of the epitaxial layers become more harmful to the operational characteristics, mature epitaxial growth technology could mitigate those issues.

The shorter the photon life time determines, the higher the modulation speed, and a short cavity results a short photon life time. Therefore, a short cavity with low current loading is highly desirable for high speed modulation, especially for high speed optoelectronic integrated circuits. For a specific cavity length, the number of quantum wells has to be optimized corresponding to the low current loading. Engelmann *et. al.* have theoretically proved that the minimum threshold current can be obtained in the optical waveguide which contains the highest QW number, and the cavity length has to be optimized to the QW number [2.22]. The MQW structure also leads to high characteristic temperature [2.23, 2.24] (low temperature sensitivity of threshold) and high modulation bandwidth [2.25-2.27]. In order to obtain minimum linewidth operation the laser should be at higher injection levels, and the number of QWs is limited to a low value in order to improve the

coherency (small linewidth and low noise), and to reduce chirping during modulation [2.28-2.30].

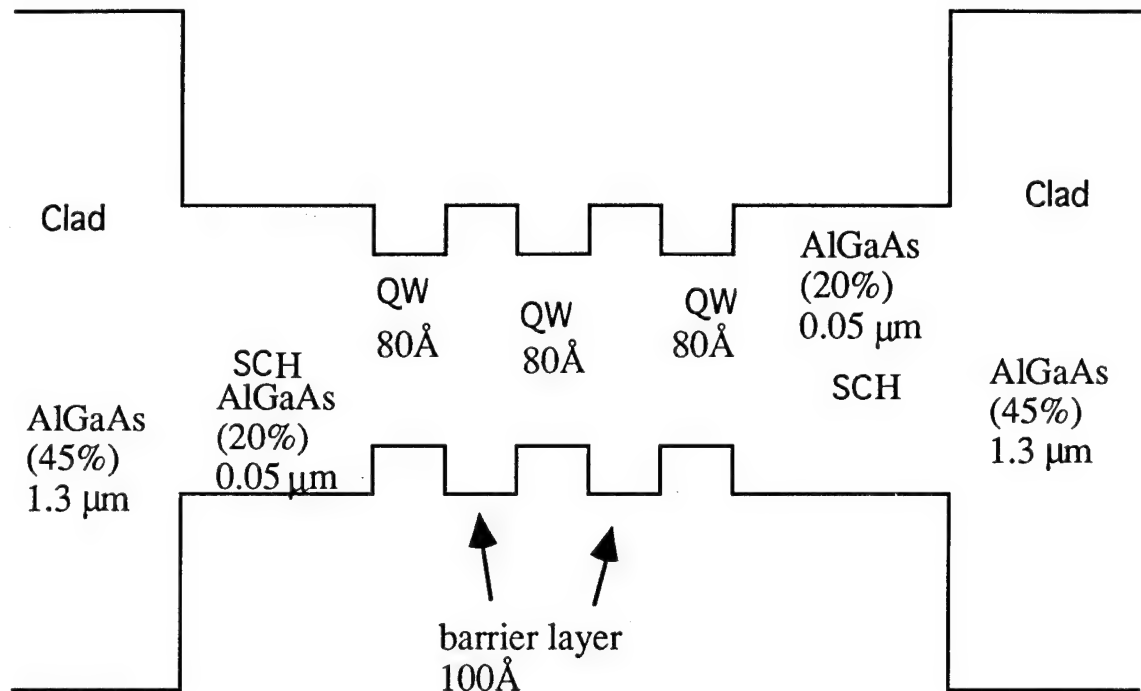


Figure 2.2. The diagram of the quantum well layer structure.

Three quantum wells have been used in our design in order to take advantage of the high differential gain coefficient at low injection carrier densities just above the transparency level. The three QW structure which we have used is suitable for the devices with the length of a few hundred micrometers [2.23]. The width of the quantum wells is 80 Å each. A design with an increased number of QW's is particularly advantageous when considering devices with very short cavities for integrated optics. Currently, we limit the device lengths between 500 μm

and 1 mm. Figure 2.2 shows the diagram of the AlGaAs/GaAs separate confinement multiple quantum well layer structure.

In 1981, Tsang discovered that the high thresholds of MQW lasers were mainly due to the inefficiency in injecting carriers over the barriers existing between wells [2.31]. He optimized barrier heights and thicknesses and used greater Al content in the outer layers to obtain separate confinement of the optical energy. In his optimization of barrier heights between the wells, the 20% Al in the barrier provided the minimum threshold current. Figure 2.3 shows the optimization of the threshold current vs. Al mole fraction in the barrier.

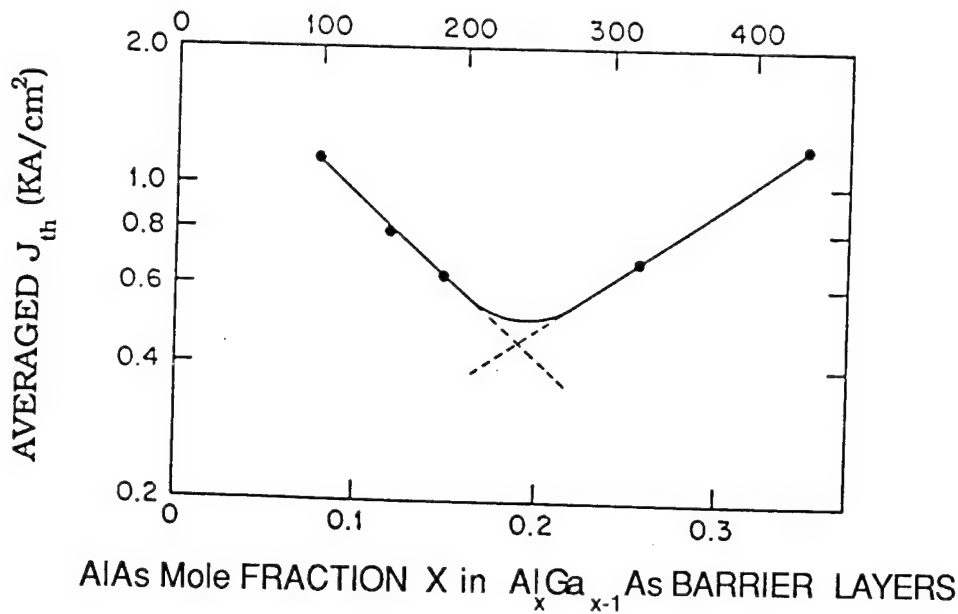


Figure 2.3. Optimization of heights of the barriers between wells in a MQW laser[after Tsang, Ref. 2.32].

It is very important to minimize the carrier transport times across the separate confinement heterostructure (SCH) and barrier layers, in order to maximize the modulation bandwidth of a quantum well laser. Therefore, the thickness of the SCH and barrier layers plays a crucial role, in addition to the high differential gain, the short photon life time, and large optical mode confinement for determination of the modulation bandwidth.

The carriers are injected into the undoped SCH and active region from the doped cladding region, and subsequently travel across the barriers and recombine in the QWs. The carrier transport dynamics for the structure shown in figure 2.1 is governed by a set of coupled rate equations which are [2.33]:

$$\frac{dN_s}{dt} = \frac{I}{qV} - \frac{N_s}{\tau_s} - \frac{N_s}{\tau_n} \quad (2.23)$$

$$\frac{dN_1}{dt} = \frac{N_s}{\tau_s} - \frac{N_1}{N_2 \tau_c} - \frac{N_1}{\tau_n} - g(N_1, P_1) (1 - \epsilon S) S \quad (2.24)$$

$$\frac{dN_2}{dt} = \frac{N_1 - N_2}{\tau_c} - \frac{N_2 - N_3}{\tau_c} - \frac{N_2}{\tau_n} - g(N_2, P_2) (1 - \epsilon S) S \quad (2.25)$$

$$\frac{dN_3}{dt} = \frac{N_2 - N_3}{\tau_c} - \frac{N_3}{\tau_n} - g(N_3, P_3) (1 - \epsilon S) S \quad (2.26)$$

$$\begin{aligned} \frac{dS}{dt} = & \Gamma g(N_1, P_1) + g(N_2, P_2) \\ & + g(N_3, P_3) (1 - \epsilon S) S - \frac{S}{\tau_p} \end{aligned}$$

$$+ \frac{\Gamma\beta}{\tau_n} (N_1 + N_2 + N_3) \quad (2.27)$$

where N_s , N_1 , N_2 , N_3 , and S are the electron densities in SCH, the three quantum wells, and photon density in the cavity, respectively. P_1 , P_2 , and P_3 are the hole densities in the three quantum wells respectively. The other terms are g for the gain, ϵ for the nonlinear parameter, Γ for optical confinement factor per well, τ_n for carrier recombination lifetime, τ_p for photon lifetime, τ_s for the carrier transport time across the SCH, and τ_c for the carrier transport time across the barrier. τ_n is given by:

$$\tau_n = \tau_{SCH} + \tau_{cap} \quad (2.28)$$

where τ_{SCH} and τ_{cap} are the diffusion time across the SCH and the electron capture time by the nearest quantum well respectively. τ_c is given by

$$\tau_c = [1/(\tau_{ther} + \tau_{bar} + \tau_{cap}) + 1/\tau_{tun}]^{-1} \quad (2.29)$$

where τ_{ther} , τ_{bar} , and τ_{tun} are thermionic emission time, the diffusion time across the barrier, and the tunneling time through the barrier.

The coupled rate equation for P_1 , P_2 , and P_3 have equivalent expressions. All of the coupled rate equations have to be solved simultaneously with the assistance of the experimental measurement and theoretical simulation for all of the parameters used in the coupled rate

equations, and these simulation had been carried out in reference [2.33]. The simulation on the electron and hole transport times across barriers showed the dominant effects of different thicknesses of the barrier. When the barriers are sufficiently narrow ($<50\text{\AA}$), tunneling dominates the carrier transport across the barriers. As the thickness increases, the hole transport is mainly by thermionic emission and kept almost constant times while the electron transport is still dominated by the tunneling. For the thick barrier ($>250\text{\AA}$), both carrier transport times are dominated by thermionic emission and kept approximately constant. Thus, the modulation bandwidth for thick barrier is not sensitive with barrier width. We chose the thickness of the barriers for our layer structure to be 100\AA , so that both carrier transport times are in the range of picoseconds.

The small signal solution of the rate equations is carried out for the slower carrier, i.e., holes [2.33]. The -3 dB bandwidth which is influenced by the thickness of the SCH had been characterized in the simulation [2.33]. For a specific number of QWs, there is an optimum SCH width for the maximum modulation bandwidth. For a narrow SCH the optical confinement is poor, which results in larger threshold gain and threshold carrier density, and consequently a lower differential gain. For a wide SCH, the diffusion time across the SCH increases so that the bandwidth is reduced. For our structure the maximum bandwidth is obtained at about 500\AA thick SCH.

The reference [2.33] revealed that the carrier transport time for graded index SCH is at least as twice large as the one in ungraded SCH. And the experimental results proved that the transport time in graded

SCH is 3 to 4 times larger than that for the SCH without graded index [2.34].

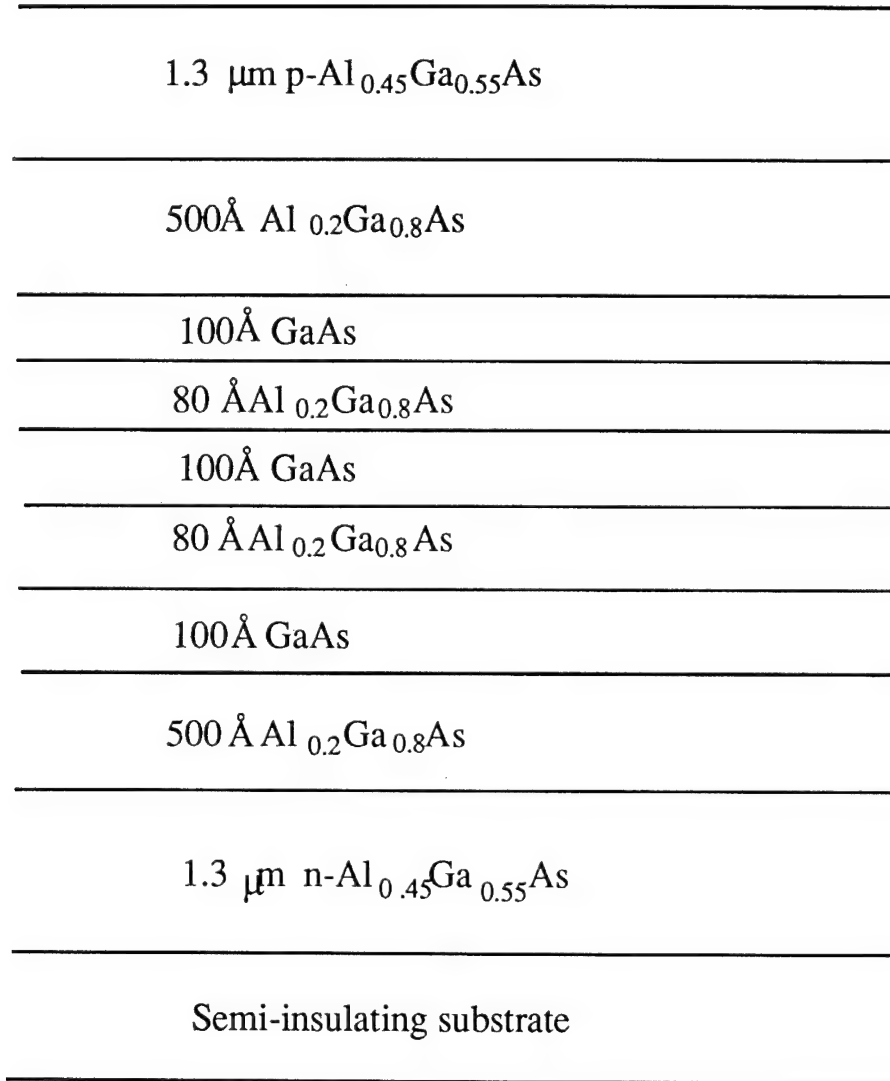


Figure 2.4. Layer structure

In order to obtain high optical mode confinement, the AlGaAs with high Al mole fraction is used in the cladding layers. The higher Al

mole fraction the cladding layer is, the higher confinement factor is. But the AlGaAs with high Al mole fraction has a low mobility, and the requirement of single mode ridge waveguide structure also limits the amount of the Al mole fraction in the AlGaAs.

The cladding layers are 45% AlGaAs doped p or n type corresponding to the contacts. The thickness of the cladding layers and separate confinement layers has been optimized for maximum optical confinement in the transverse direction. Figure 2.4 shows the layer structure.

2.2.3. Waveguides

An optical waveguide is a structure which is used to confine and guide the light in the waveguide device. The simplest optical waveguide is a three-layer slab waveguide, and the three layers are called cladding layer, guiding layer, and substrate, respectively. The guiding layer has the largest refractive index among these layers, the refractive index of substrate is usually equal or larger than the one in cladding layer. Therefore light can be confined in guiding layer surrounded by cladding layer and substrate. The light signals are transmitted through the waveguide in the form of guided modes of the waveguide. A slab waveguide performs well as an optical waveguiding device, and is easy to fabricate, but the planar optical waveguide provides no optical confinement within the film plane. Adding lateral optical confinement

leads to the channel waveguide. Channel waveguides are used in many active and passive devices including lasers, modulators, switches, and directional couplers. The additional confinement helps to bring about desirable device characteristics such as savings in drive power and drive voltage. There are many types of channel waveguides, i.e., buried channel, raised strip, embedded strip, ridge guide, etc. The ridge waveguide is the simplest to fabricate for use in semiconductor lasers, since it does not require regrowth.

Optical waveguides which can support more than the fundamental guided mode are called multi-mode waveguides. In multi-mode waveguides, mode interference and undesired mode conversion due to small disturbances reduce waveguide device performance significantly. To avoid these drawbacks, our waveguides are single-mode waveguides supporting only the fundamental TE and TM modes.

Figure 2.5 shows the ridge waveguide structure which is employed in our active optical switches. The proper etched-depth of the ridge ensures the single-mode requirement for the waveguide. The lateral optical confinement is due to the etching of the ridge. However, the optical signal is weakly guided in the lateral direction, and strongly guided in the transverse direction due to the abrupt change of Al mole fraction between the cladding layers and guided region. A smaller etch depth of the ridge leads to the guided mode spreading along the lateral direction. This increases the overlap area of optical field on quantum well along lateral direction away from the ridge. The section of quantum wells immediately under ridge can be pumped efficiently by current, to

obtain gain [2.35]. The remaining sections of the quantum wells, away from the ridge, are lossy to the optical fields, due to the inefficient pumping. Over-etching of the ridge leads to a multi-mode waveguide [2.36]. The tolerance of the etching depth is a very important parameter for waveguide fabrication. Relatively large tolerances are desirable for successful fabrication. We designed the waveguide with $0.9\text{ }\mu\text{m}$ etch depth within $0.1\text{ }\mu\text{m}$ tolerance. The calculation and analysis details for the waveguide design are presented in Chapter 3.

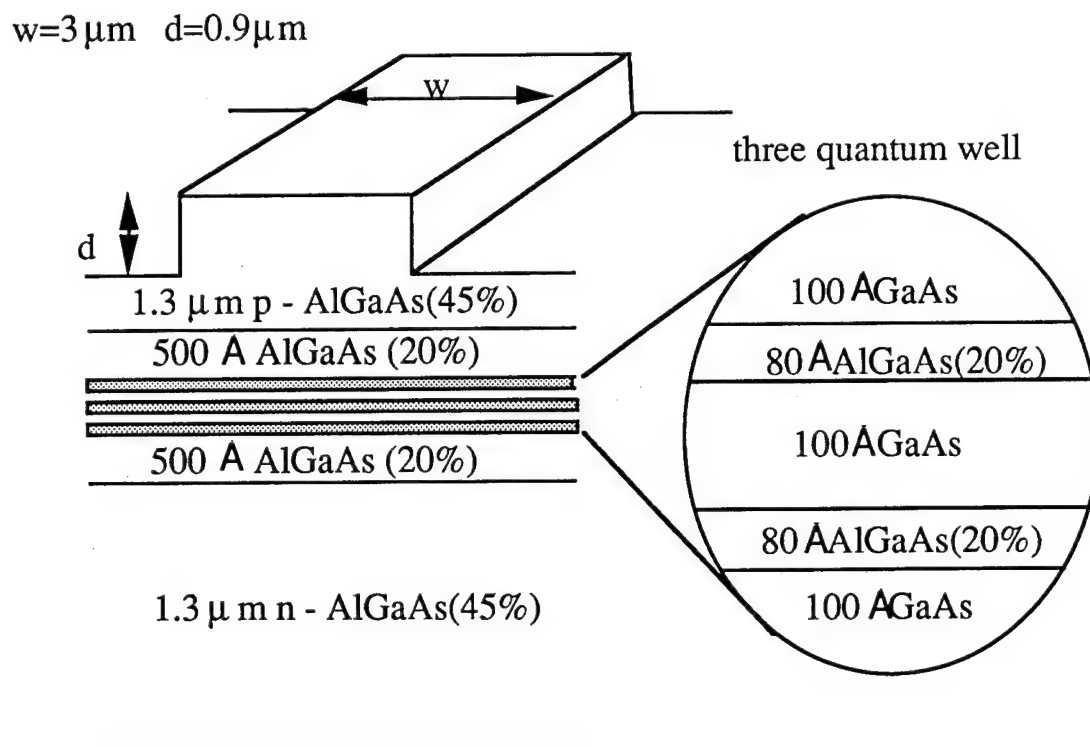


Figure 2.5. The ridge waveguide structure

The fundamental TE and TM modes are the only modes supported by this waveguide. To avoid mode dispersion between them, the structure must be designed such that the two modes have about the same propagation constant or have a negligible difference between the two propagation constants. For our waveguides there is 10^{-9} difference between the two propagation constants for the wavelength for which we are interested (see Chapter 3 for the calculation details).

Since fabrication errors are always possible, tolerance for the width of ridge is also importance. Our waveguides are single mode for the width range of $3\text{ }\mu\text{m}$ to $5\text{ }\mu\text{m}$ at the ridge etch depth of $0.9\text{ }\mu\text{m}$.

Holes are injected into the active region through the p-doped top cladding layer which forms the ridge structure, and the electrons arrive in the quantum wells by injection through the n-doped lower cladding layer. The doping profile in the ridge layer structure is one of most important parameters in the design. The lower the doping in the cladding layers, the bigger the series resistance of the diode. This causes a relatively large voltage drop in the cladding layers, which creates heat and limits device performance. Heavier doping in the cladding layers reduces the series resistance dramatically, but the optical loss increases as a result. Consequently, the current loading necessary for transparency increases, since the optical field is confined in the core region. The best strategy is to avoid the heavier doping in areas where the optical field is strong. Figure 2.6 shows the contour plot of the optical field for the switch waveguide. The optical field decays exponentially in the cladding layers. At the regions near the top and the bottom of cladding layers, the optical

field is almost zero, and we therefore dope these regions as heavily as possible. For the region where the optical field is small but nonzero, we have reduced the doping, and Figure 2.7 shows the doping profile for our layer structure. We put highly doped GaAs layers on the very top and very bottom for reduced ohmic contact resistance, and $5 \times 10^{19} \text{ cm}^{-3}$ and $3 \times 10^{18} \text{ cm}^{-3}$ are the doping densities are used for p-type and n-type cladding layers, respectively. These doping densities result in resistivity less than $2 \times 10^{-3} \Omega\text{-cm}$ [2.45]. The doping densities for the top half of the top cladding layer and lower half of the bottom cladding layer are $3 \times 10^{18} \text{ cm}^{-3}$, and the doping densities for remaining parts of the both cladding layers are 1×10^{17} , where we have to consider the current spreading effect under the ridge, which is discussed next. Both SCH layers are undoped, since the diffusion lengths for electron and holes are much longer than their thickness. The quantum wells are doped at $3 \times 10^{18} \text{ cm}^{-3}$ for higher differential gain [2.33]

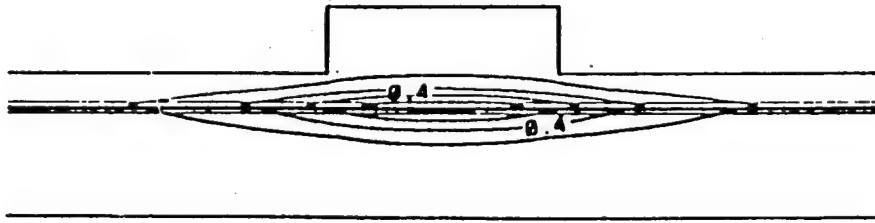


Figure 2.6. The contour plot for the ridge waveguide

0.2 μm p-GaAs	$5 \times 10^{19} \text{ cm}^{-3}$
0.9 μm p-Al _{0.45} Ga _{0.55} As	$3 \times 10^{18} \text{ cm}^{-3}$
0.4 μm p-Al _{0.45} Ga _{0.55} As	$1 \times 10^{17} \text{ cm}^{-3}$
500Å Al _{0.2} Ga _{0.8} As	(undoped)
100Å GaAs	$3 \times 10^{18} \text{ cm}^{-3}$
80 Å Al _{0.2} Ga _{0.8} As	(undoped)
100Å GaAs	$3 \times 10^{18} \text{ cm}^{-3}$
80 Å Al _{0.2} Ga _{0.8} As	(undoped)
100Å GaAs	$3 \times 10^{18} \text{ cm}^{-3}$
500 Å Al _{0.2} Ga _{0.8} As	(undoped)
0.9 μm n-Al _{0.45} Ga _{0.55} As	$1 \times 10^{17} \text{ cm}^{-3}$
0.4 μm n-Al _{0.45} Ga _{0.55} As	$3 \times 10^{18} \text{ cm}^{-3}$
1.0 μm n-Ga As	$3 \times 10^{18} \text{ cm}^{-3}$

Semi-insulating substrate

Figure 2.7. The doping profile of the layer structure.

Although the ridge structure has some advantages over certain other geometries, there is no lateral current confinement in this structure, so that the drive current spreads along the lateral direction under the ridge as it injected into the active region. Therefore, the threshold current density is higher in these device, compared to those structures with lateral current confinement. An analytical model for analysis the current spreading had been carried out for a strip-contact injection laser in reference [2.37]. Here we applied this model to our ridge waveguide for current spreading effect. Figure 2.8 shows a diagram of current spreading for a half ridge structure. Let V is the potential at point o (see Figure 2.8), and i is the spreading current. For $x > 0$, we can write following two equations to approach the spreading effect:

$$\frac{dV}{dx} = -R_s i \quad (2.30)$$

$$\frac{di}{dx} = -j(x) = -j_0 \exp(Ve/nkT) \quad (2.31)$$

where R_s is the sheet resistant, J_0 is the current through the laser, e is the electron charge, n is the ideality factor for the diode, k is the Planck's constant, and T is temperature. The analytical solution of these equations which describes the current spreading beyond the ridge is

$$i(x=0) = 20.5 \frac{nkT}{R_s x_0 e} \quad (2.32)$$

where the x_0 is given by

$$x_0 = \left(\frac{nkT}{R_{sj}0e} \right)^{0.5} \quad (2.33)$$

This current is equal to the amount which would go through an additional ridge width, Δw , which is given by

$$\Delta w = 2^{3/2} x_0 \quad (2.34)$$

using the our data into equation (2.34), we get about 3 micrometers additional width on each side of the ridge, and this is in agreement with our calculations discussed in Chapter 3.

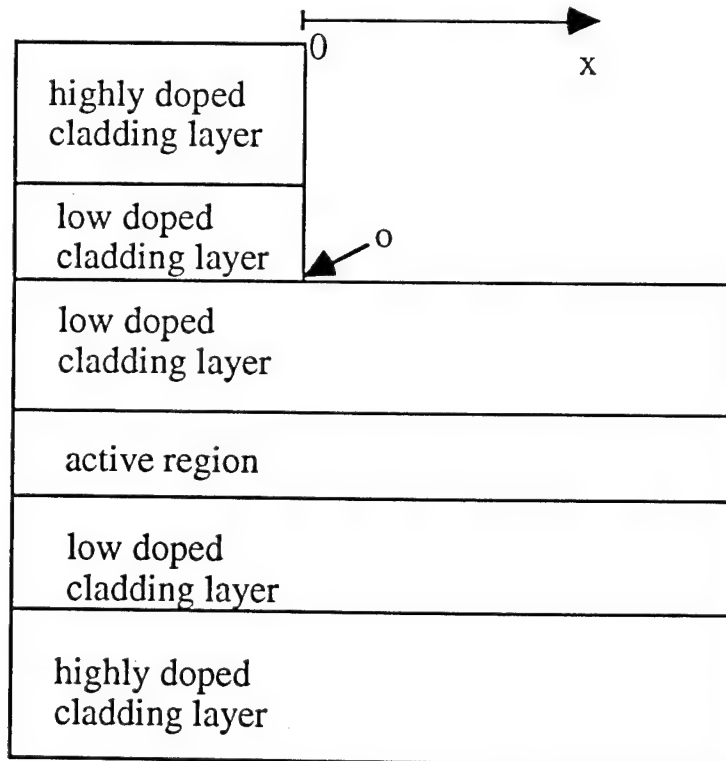


Figure 2.8. A diagram of a half ridge for current spreading effect.

2.2.4. Switches

The active switches which we designed in this project are monolithic 1×1 , 1×2 , 2×2 , 1×4 , and 4×4 switches. They are completely nonblocking switch structures, i.e. all inputs can simultaneously reach all outputs even if the outputs are different. These switches can be operated in either a point-to-point or broadcast mode, and simultaneously link any combination of input/output ports on one side with any combination of ports on the other. The 1×1 switch is a gate switch/amplifier, and it also can also be used as a modulator, with proper DC bias across it to encode income optical signals. The 1×2 switch is a branch switch splitting optical power with negligible loss or gain. The 2×2 switch is the crossbar switch, which may be used to build any complicated optical switch matrix with proper interconnects, and these optical crossbar switches are reconfigurable, with the reconfiguration of the electrical connects for the 2×2 switches. The 1×4 switch is a four-way power splitter with negligible loss or gain, and composed of three 1×2 switches. The 4×4 switch is a reconfigurable four-way optical switch matrix and composed of five 2×2 switches. In common with other types of semiconductor devices, the response of the switch may be affected by chip parasitics at very high frequencies. The chip parasitics are stray capacitance and the resistance associated with the semiconductor material surrounding the active region. The most significant effect of chip parasitics is the high-frequency shunting of the modulation current around the active region.

Chip parasitics are strongly structure-dependent. The details of the chip parasitic resistance and capacitance depend strongly on the device structure. The width of the ridge in our design for the switches is about 3 μm . The p-type ohmic contact on top of the ridge has a similar size so that the ridge structure has lower capacitance. Because the p-type ohmic contact is narrow, the sheet resistance on the top of the ridge with airbridged connection is relatively high. This causes nonuniform pumping current distribution to the switch. We put dielectric material on each side of the ridge, and enlarged the width of the top metal contact to be about 13-15 μm in width. This dramatically reduces the sheet resistance, but increases the parasitic capacitance. Figure 2.9. shows the structure in detail.

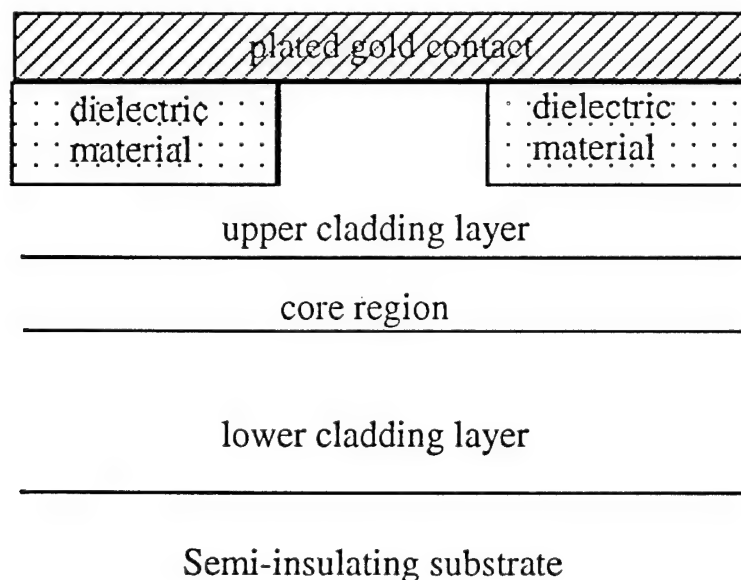


Figure 2.9. The cross section of the switch structure.

Our switches are fabricated on a semi-insulating substrate and have lower parasitic capacitance than one fabricated on the n-type substrates. The two oppositely-biased electrode pads are almost co-planar and are on semi-insulating material.

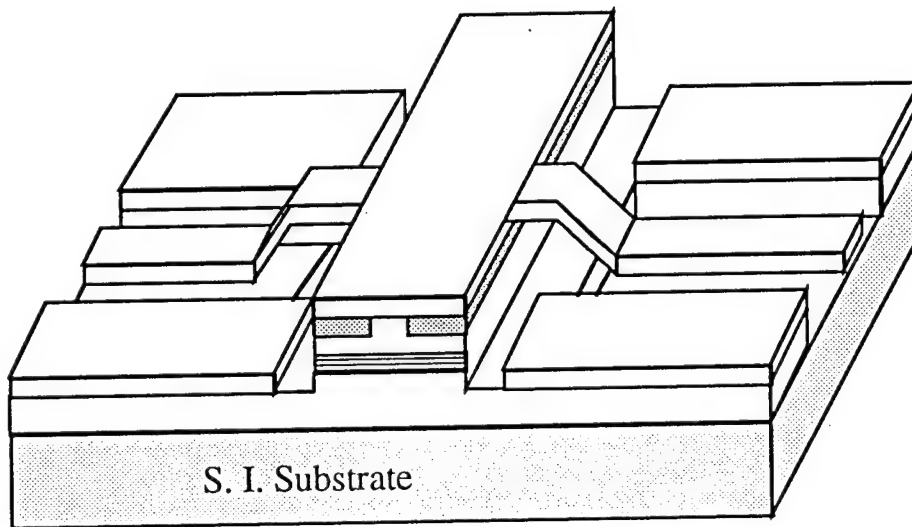


Figure 2.10. The structure of a single mode multiple quantum well ridge waveguide laser.

Since our active optical switches are based on semiconductor lasers, the ridge waveguide laser was designed first, and the design of active optical switches are based on the laser structure. However, by testing the diode for the characterization of DC and RF, we obtain the information of current loading and dynamic response for the switches. A single mode multiple ridge waveguide laser diode is shown in Figure 2.10. There are three contact pad on each side of the ridge for wire bonding or probing test. The middle pads on each side of the ridge are

for source, and the remainder are ground pads. The source pads are connected to ridge top by airbridges, and the thickness of all pads and airbridges including the ridge top metal is about $2\text{ }\mu\text{m}$. The geometry of the pads is matched to RF probes, so that the device can be directly probed by the RF probes without any packaging.

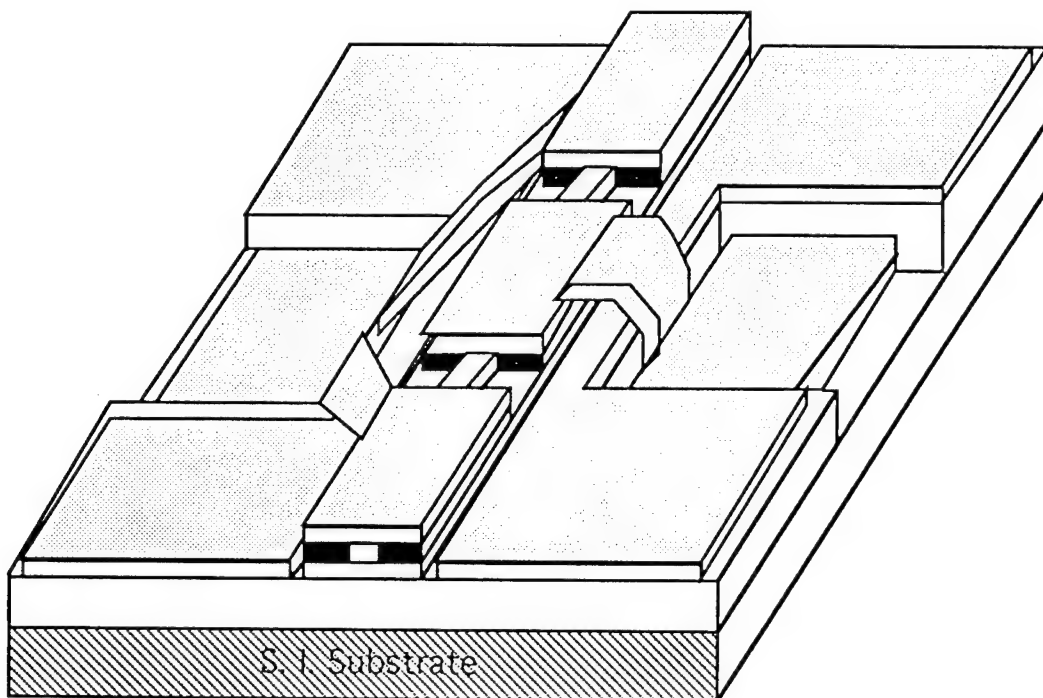


Figure 2.11. The structure of an 1×1 switch/modulator.

Figure 2.11 shows a 1×1 switch, which is similar to the ridge waveguide laser diode shown in Figure 2.10. The longer arm is for the DC section which is transparent to the incoming optical signal. The short area is the switch arm, and will be biased separately. The length of this

section is 50 μm , 75 μm , or 100 μm , respectively, which result 5 dB, 7 dB, and 10 dB extinction ratios, respectively. The gap between any two sections is for the electrical discontinuity, and about 5 μm long, and the total size of the device is 500 $\mu\text{m} \times 500 \mu\text{m}$. This device shown in Figure 2.11 can act as a switch for optical signals with proper biasing current. It may also be used as a modulator when the biasing current just above transparency, has a modulated signal added to it. The output optical signal carries the information of the modulated current.

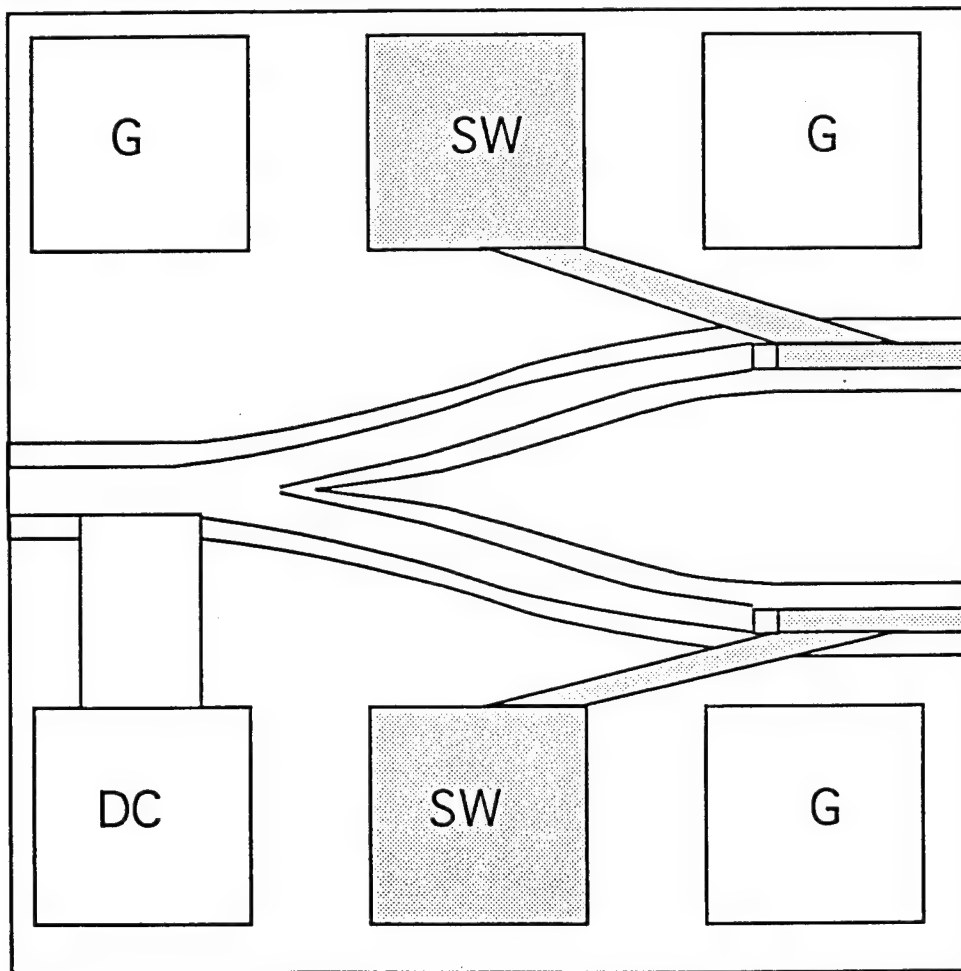


Figure 2.12. The structure of an 1×2 switch.

A top view of the 1×2 switch is shown in Figure 2.12. The waveguide is split into two ridge waveguides from a single ridge waveguide. The radius of the curvature used is as large as possible, to minimize the bending loss. Since our switches are active devices, the loss from bending is no longer a problem at all. The spacing between output two parallel ridges is $100\ \mu\text{m}$. The small sections on the ridges near the ends of ridges are the switch arms, which are $50\ \mu\text{m}$, $75\ \mu\text{m}$, and $100\ \mu\text{m}$ long, respectively. The long split regions on the ridges is the DC section. Both of the DC arm and switch arms are connected to electrode pads by airbridges. The switch electrode pads are between ground pads so that the RF probes may be used. The total size of this device is $500\ \mu\text{m} \times 500\ \mu\text{m}$. The device can route the incoming optical signals to either one of the two parallel waveguides.

Figure 2.13 shows a top view of a 2×2 switch. There are two parallel waveguides which are connected to each other by an 'x' shape waveguide, with the angle of the 'x' shape at 90 degree. There are two small switch sections on the middle of the two parallel waveguides. The switch section is $100\ \mu\text{m}$ long, and always biased oppositely to 'x' shape switch section. There are four electrode pads on each side of the two parallel waveguides, and these are connected to the corresponding pads by airbridges, except for ground pads. The size of the device is $500\ \mu\text{m} \times 500\ \mu\text{m}$. When the parallel switch sections are in the on-state, the incoming optical signals at 1_i and 2_i go through the two parallel waveguides to 1_o and 2_o with no crossing. When they are in the off-state, and the 'x' shape waveguide is in on-state, the incoming optical signals

on the two waveguides are routed to the other guide, with 1_i signal going to 2_o , and 2_i signal to 1_o .

The crosstalk from the 'x' shape waveguide is small, and it has previously been theoretically and experimentally tested to be less than 1% [2.38].

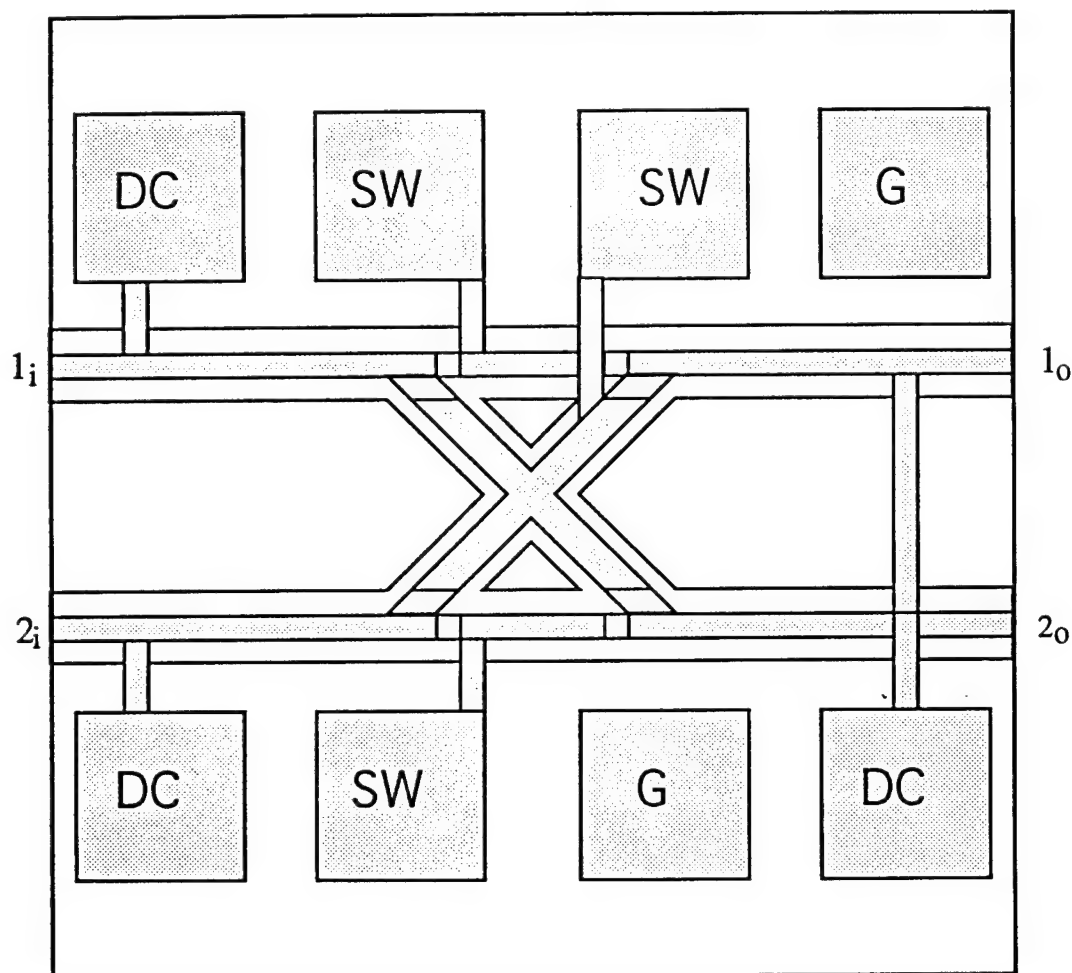


Figure 2.13. The structure of a 2x2 switch.

The 1×4 switch is composed of three 1×2 switches. The figure 2.14 shows the mask layout of a 1×4 switch, with the narrow lines shows the waveguides. The wider lines are the ground connecting path. All of the top ridge sections are connected to electrode pads by airbridges. All of the switch sections are $100\mu\text{m}$ long, and the size of the 1×4 switch is $1\text{ mm} \times 0.5\text{ mm}$. This device can be extended by more 1×2 switch to $1 \times N$ switch, and may act as an optical signal splitter.

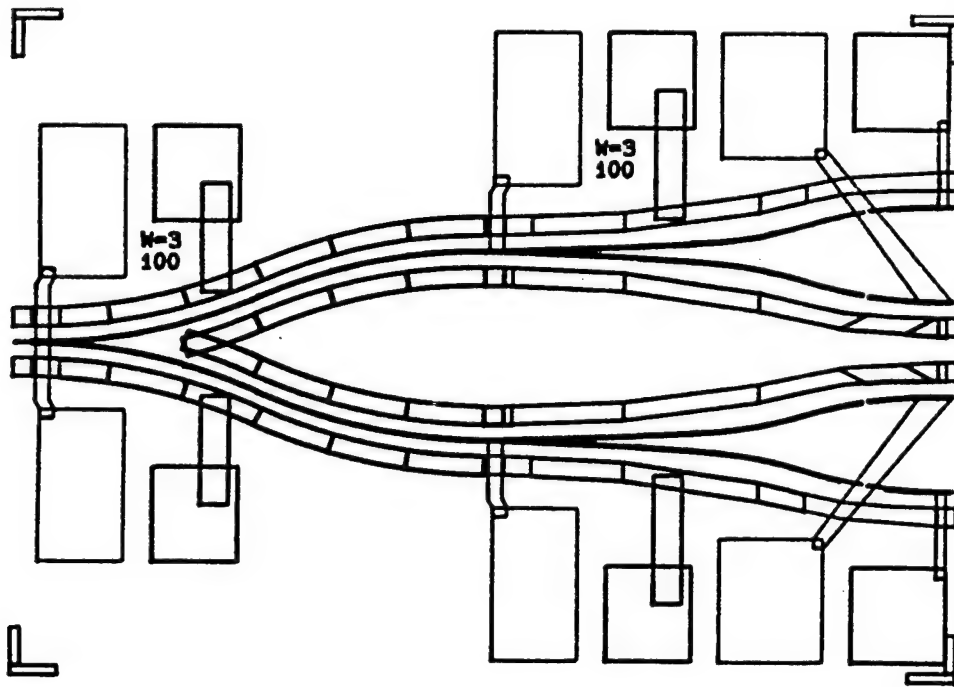


Figure 2.14. Mask layout of a 1×4 switch.

The 4×4 switch is composed of five 2×2 switches and is an extended version of the 2×2 switches. Figure 2.15 shows the mask layout of the device, and the chip size of the device is 1 mm × 0.5 mm.

The antireflection coating adopted for our switches is a single layer SiO_x and the thickness is about 0.18 μm , which meets the requirement of quarter wave window, and the coating is deposited by electron beam evaporation.

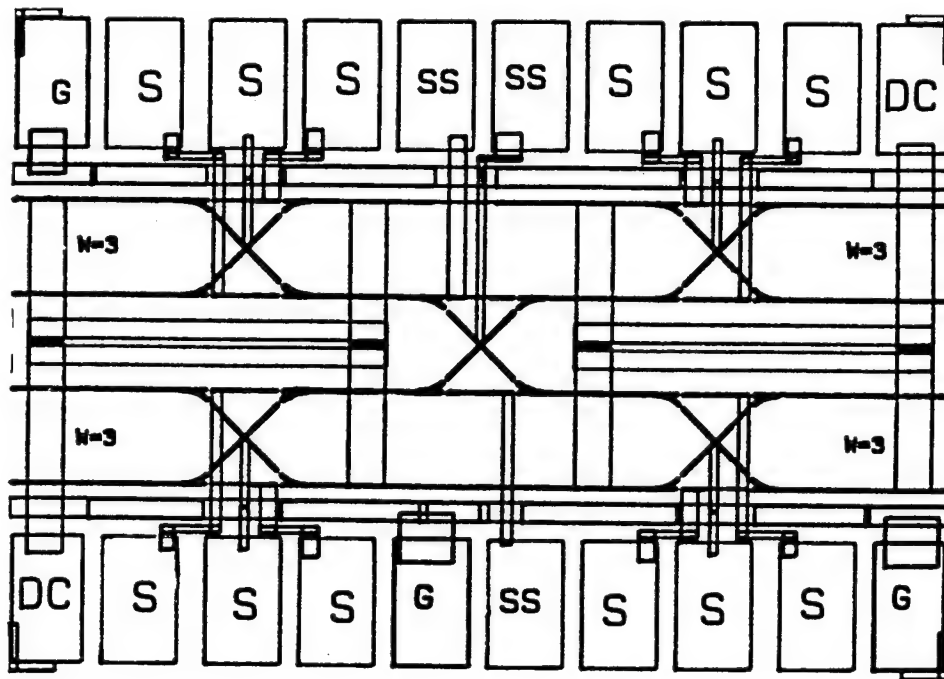


Figure 2.15. Mask layout of a 4×4 switch.

REFERENCES

- [2.1] T. Mukai, and Y. Yamamoto, "Gain, frequency bandwidth, and saturation output power of AlGaAs DH laser amplifiers", IEEE J. Quantum Electron., QE-17, pp. 1028-1034, 1981.
- [2.2] M. Ikeda, "Optical properties for an antireflection-coated LD optical switch," Electron. Lett., vol. 19, no. 20, pp. 826-828., 1983.
- [2.3] A. Yariv, Optical Electronics, 3rd ed. Holt, Reinehart and Winston, New York, 1985.
- [2.4] G. H. B. Thompson, Physics of Semiconductor Laser Devices, Wiley, New York, 1980.
- [2.5] T. Ikegami and Y. Suematsu, Proc. IEEE 55, p. 122 (1967).
- [2.6] Y. Arakawa and A. Yariv, IEEE J. Quantum Electron. QE-21, p. 1666 (1985).
- [2.7] K. J. Vahala and C. E. Zah, Appl. Phys. Lett. 52, p. 1945 (1988).
- [2.8] K. Y. Lau, Ch. Harder, A. Yariv, Appl. Phys. Lett. 44, p. 273 (1987).
- [2.9] J. E. Bowers, Solid-State, Electron. 30, p. 1 (1987).
- [2.10] K. Uomi, N. Chinone, T. Ohtoshi, and T. Kajimura, Jpn. J. Appl.
- [2.11] M. Osinski and J. Buus, "Linewidth broadening factor in semiconductor lasers - An overview," IEEE J. Quantum Electron., QE-23, pp. 9-29, 1987.
- [2.12] G. Eisenstein, U. Koren, G. Raybon, T. L. Koch, J. M. Wiesenfeld, M. Wegener, R. S. Tucker, and B. I. Miller, "Large- and small- signal gain characteristics of 1.5 μm multiple quantum well optical amplifiers," Appl. Phys. Lett., vol. 56, pp. 1201-1203, 1990.
- [2.13] M. Bagley, G. Sherlock, D. M. Cooper, I. D. Westdook, D. J. Elton, H. J. Wickes, P. C. Spurdens, and W. J. Devlin, "Broadband operation of InGaAsP-InGaAs GRIN-SC-MQW-BH amplifier with 115 mW output power," Electron. Lett., vol. 26, pp. 512-513, 1990.
- [2.14] G. Eisentein, J. M. Wiesenfeld, M. Wegener, G. Sucha, D. S. Chemla, S. Weiss, G. Raybon, and U. Koren, "Ultrafast gain dynamics in 1.5 μm multiple quantum well optical amplifiers," Appl. Phys. Lett., vol. 58, pp. 158-160, 1991.

- [2.15] S. Weiss, J. M. Wiesenfeld, D. S. Chemla, G. Raybon, G. Sucha, M. Wegener, G. Eisenstein, C. A. Logan, and T. Tanbun-Ek, "Carrier capture times in 1.5 μm multiple quantum well optical amplifiers," *Appl. Phys. Lett.*, vol. 60, pp. 9-10, 1992.
- [2.16] G. Eisenstein, R. S. Tucker, J. M. Wiesenfeld, P. B. Hansen, G. Raybon, B. C. Johnson, T. J. Bridges, F. G. Storz, and C. A. Burrus, "Gain recovery time of traveling-wave semiconductor optical amplifiers," *Appl. Phys. Lett.* vol. 54, pp. 454-456, 1989.
- [2.17] J. M. Wiesenfeld, A. H. Gnauck, G. Raybon, and U. Koren, "High-speed multiple-quantum-well optical power amplifier," *IEEE Photonics Tech. Lett.*, vol. 4, no. 7, pp. 708-711, 1992.
- [2.18] J. Hegarty and K. A. Jackson, "High-speed modulation and switching with gain in a GaAs traveling-wave optical amplifier," *Appl Lett.* vol. 45, no. 12, pp. 1314-1316, 1984.
- [2.19] S. Adachi, "GaAs, AlAs, and $\text{Al}_x\text{Ga}_{1-x}\text{As}$: material parameters for use in research and device applications," *J. Appl. Phys.*, vol. 58(3), pp. R1-R29, 1985.
- [2.20] Y. Arakawa and A. Yariv, *IEEE J. Quantum Electron.* QE-22, 1887 (1986).
- [2.21] P. W. A. McIlroy, A. Kurobe, and Y. Uemastu, *IEEE J. Quantum Electron.* QE-21, 1958 (1985).
- [2.22] R. W. H. Engelman, C-L Shieh, and C. Shu, *Quantum well Lasers*, ed. P. S. Zory, Jr., Academic Press, pp. 131-186, 1993.
- [2.23] L. D. Zhu, B. Z. Zheng, Z. Y. Xu, and G. A. B. Feak, *IEEE J. Quantum Electron.* 25, 1171 (1989).
- [2.24] P. S. Zory, A. R. Reisinger, R. G. Waters, L. J. Mawst, C. A. Zmudzinski, M. A. Emunuel, M. E. Givens, and J. J. Coleman, *Appl. Phys. Lett.* 49, 16 (1986).
- [2.25] T. Yuasa, T. Yamda, K. Asakawa, M. Ishii, M. Uchida, *Appl. Phys. Lett.* 50, 1122 (1987).
- [2.26] H. D. Wolf, H. Lang, and L. Korte, *Electron. Lett.* 25, 1246 (1989).
- [2.27] H. Lang, H. D. Wolf, L. Korte, H. Hedrich, C. Hoyler, and C. Thannner, *IEE Proc.*, Part J 138, 171 (1991).
- [2.28] S. Hausser, W. Idler, E. Zielinski, M. H. Pilkuhn, G. Weimann, and W. Schlapp, *IEEE J. Quantum Electron.* QE-25, 1469 (1989).

- [2.29] N. K. Dutta, H. Temkin, T. Tanbun-Ek, and R. Logan, Appl. Phys. Lett. 57, 1390 (1990).
- [2.30] T. Takahashi, J. N. Schulman, and Y. Arakawa, Appl. Phys. Lett. 57, 1390 (1990).
- [2.31] W. T. Tsang, Appl. Phys. Lett. 39, 786 (1981).
- [2.32] W. T. Tsang, C. Weisbuch, R. C. Miller, R. Dingle, "Current injection GaAs-Al_xGa_{1-x}As multi-quantum-well heterostructure lasers prepared by molecular epitaxy," Appl. Phys. Lett. vol. 39, pp. 786-788, 1981.
- [2.33] R. Nagarajan, T. Fukushima, S. W. Corzine, and J. Bowers, "Effects of carrier transport on high-speed quantum well lasers," Appl. Phys. Lett. vol. 59, no. 15, pp. 1835-1837, 1991.
- [2.34] S. Weiss, J. M Wiesenfeld, D. S. Chemla, G. Raybon, G. Sucha, G. Eisenstein, C. A. Burrus, A. G. Dentai, U. Koren, B. I. Miller, H. Temkin, R. A. Logan, and T. Tanbun-Ek, Conference on Quantum Electronics Laser Science (QELS), Baltimore, paper QThD3, 1991.
- [2.35] W. P. Dumke, "Current thresholds in stripe-contact injection lasers," Solid-State Electronics, vol. 16, pp. 1279-1281, 1973.
- [2.36] B. Koch, K. Johnson, H. Dong, and A. Gopinath, OSA Integrated Photonics Research, San Francisco, Feb. 17-19, ThF8, 1994.
- [2.37] S. M. Sze, Physics of Semiconductor Devices, 2nd Ed., John Wiley & Sons, Inc. 1981.
- [2.38] C. L. Balestra, R. J. Blackwell, B. C. Johnson, and L. G. Perrymore, "Monolithic semiconductor active waveguide optical switch," SPIE Conference on Photonics for Space Environments 1952-18, Orlando, 1993.

CHAPTER 3

WAVEGUIDE DESIGN

The waveguide structure is a very important part of the design of active optical switches, since all these are based on a planar guide structure. All the optical signals are manipulated, amplified/attenuated and split in these waveguides. The waveguide structure used in the active optical switches is a single mode ridge waveguide, the guided structure is easily fabricated with no regrowth. The single mode structure was ensured by careful analysis, and numerical calculation for eliminating the mode dispersion. A wide tolerance range of the parameters of the single mode structure is desirable for device fabrication. The range of the parameters of ridge waveguide enhances the possibility of successful fabrication of the single mode ridge waveguide. The degeneracy for the fundamental TE and TM modes is also desirable for polarization insensitivity.

The design of the single mode ridge waveguide used in the active optical switches is presented in this chapter. The numerical technique used for designing the waveguides is introduced in section 3.1. The numerical calculation and analysis of waveguide is presented in detail in sections 3.2 and 3.3, respectively. Two examples of dielectric waveguides were used for testing the accuracy and efficiency of the numerical scheme, shown in section 3.4. The design of single mode

ridge waveguide for the active optical switches is presented in section 3.5.

3.1. Introduction

The active waveguide is analyzed at transparency since the gain and loss constants are an order of magnitude smaller than the mode propagation constant. Thus, we analyze dielectric waveguides in this chapter and these are of interest in a variety of integrated microwave and optical integrated circuits. The guided modes are the very basic physical variable to be determined. Analysis of the modes of dielectric waveguides are necessary for the design of many optoelectronic devices. In most cases, the analytical solution for the modes is not available, thus the use of numerical analysis becomes necessary. For dielectric waveguides with a step index profile, the mode-matching technique [3.1], finite-element analysis [3.2-3.4], and the finite-difference method [3.5-3.7] have been developed for solving the wave equations. In this chapter, we present an integrated finite-difference method [3.8] to discretize the wave equation, and the Arnoldi method [3.9,3.10] coupled with multiple deflation [3.10], followed by the inverse power method [3.11] combined with an iterative solver [3.12], for the calculation of eigenvalues and eigenvectors.

The integrated finite-difference approach is formulated in terms of transverse components of the vector magnetic (\mathbf{H}) field. A nonuniform mesh is used in the cross section of the waveguide. The wave equation

for each component of the H field is integrated over each cell of the mesh by the box integration method [3.8] in the finite difference scheme to discretize the wave equation. The boundary conditions at the interfaces with the nearest neighbor cells are enforced by employing continuity of the transverse and longitudinal components of the H field. The discretization of these boundary conditions together with the wave equation creates a sparse banded asymmetric matrix, which has two diagonal sections for H_x and H_y , and two off-diagonal sections for the coupling between the H_x and H_y . The exponential decay of the H field within the clad layers is accounted for by choosing a nonuniform mesh within these regions, but the mesh within the guide region is uniform. Only the nonzero elements of the matrix are stored.

The size of the matrix with coupling between the transverse components is about four times larger than the matrix without this coupling. Solving for all the eigenvalues of the matrix for a large number of nodes is very computationally intensive. Frequently the mode structure of the waveguide is such that only a few positive eigenvalues need to be obtained. Therefore, finding a method for accurately computing only a few eigenvalues of the matrix is highly desirable. We use the modified Arnoldi method [3.9] with multiple deflation to calculate a few extreme eigenvalues, and the corresponding eigenvectors by computing a suitable smaller matrix. With the multiple deflation [3.10], the calculation of eigenvalues only follows the few desired ones. For the strongly guided modes, the convergence of the calculation is fast and accurate. However, for single mode waveguides or weakly-guided

modes, techniques to improve the convergence of the calculation must be employed for rapid convergence. We use the inverse power method [3.11] to continue the calculation after the Arnoldi iteration yields the initial eigenvalues. This strategy makes the convergence of the calculation very fast. The s-step method [3.12] is combined with the inverse power method to avoid directly inverting the original matrix.

3.2. Discretization

Wave propagation in an inhomogeneous dielectric waveguide may be formulated in terms of longitudinal components of the \mathbf{E} or \mathbf{H} fields, or alternatively by using the transverse components [3.13]. In order to eliminate all spurious modes, the zero divergence relation of the \mathbf{H} field must be enforced in the process of the solving of wave equation. The formulation in terms of the transverse components H_x and H_y of the \mathbf{H} field may be used [3.13] to circumvent the problem of spurious modes.

We assume harmonic wave propagation, yielding a $\exp(-j\beta z)$ factor, where z is the axial direction and the β is the propagation constant. The z -component dependence of the \mathbf{H} field can be separated from the x and y components. For each region, the Helmholtz wave equation can be written as:

$$\nabla^2 H_x + (kn)^2 H_x = \beta^2 H_x \quad (1)$$

$$\nabla^2 H_y + (kn)^2 H_y = \beta^2 H_y \quad (2)$$

where H_x and H_y are the transverse components of the \mathbf{H} field, k is the wave number in free space, n is the index of refraction, and $\nabla = (\partial/\partial x, \partial/\partial y)$.

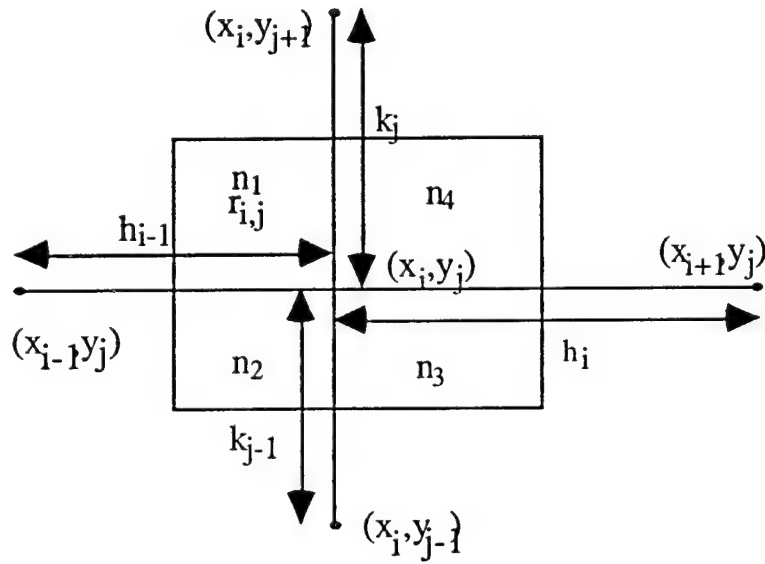


Figure 3.1. A cell of the box integration method.

We divide the cross section of the waveguide into rectangular cells, and each cell is divided into four regions based on a box integration method [3.8] (see Figure 1). In each region, the index of refraction is assumed to be constant. We integrate equations (1) and (2) over each region as follows:

$$\iint_{r_{i,j}} \nabla^2 H_a dx dy + \iint_{r_{i,j}} (k^2 n^2 - \beta^2) H_a dx dy = 0 \quad (3a)$$

Applying Gauss's theorem to equation (3a), we get the follow expressions for the wave equations:

$$\int_{c_{i,j}} \nabla H_a \cdot \hat{u} \, ds + \iint_{r_{i,j}} (k^2 n^2 - \beta^2) H_a \, dx dy = 0 \quad (3b)$$

where a is x or y , $c_{i,j}$ is the boundary of region $r_{i,j}$, and \hat{u} is the unit outward normal of $c_{i,j}$.

The transverse and longitudinal continuity of the \mathbf{H} field and the longitudinal continuity of the electrical field are used to meet the continuity boundary conditions at each internal boundary in a cell. The longitudinal components of the \mathbf{H} field and \mathbf{E} fields can be expressed in terms of H_x and H_y by using

$$\nabla \cdot \mathbf{H} = \partial H_x / \partial x + \partial H_y / \partial y - i\beta H_z = 0 \quad (4)$$

and

$$\partial H_y / \partial x - \partial H_x / \partial y = i\omega \epsilon H_z \quad (5)$$

where ϵ is the dielectric constant, and ω is angular frequency. The longitudinal continuity of the \mathbf{H} and \mathbf{E} fields along each interface between region i and j can be expressed as

$$(\partial H_x / \partial x + \partial H_y / \partial y)_i = (\partial H_x / \partial x + \partial H_y / \partial y)_j \quad (6)$$

$$\frac{1}{\epsilon_i} (\partial H_y / \partial x - \partial H_x / \partial y)_i = \frac{1}{\epsilon_j} (\partial H_y / \partial x - \partial H_x / \partial y)_j \quad (7)$$

respectively, at each interface.

Combining the equations (3b), (6), and (7) by using finite-difference formula as indicated in a box-integration method [3.8], we discretize the wave equations for the H_x and H_y as follows:

$$\begin{aligned} & \frac{1}{2k_j} \left(h_{i-1} \frac{n_2}{n_1} + h_i \frac{n_3}{n_4} \right) H_x(i, j+1) + \frac{1}{2k_{j-1}} \left(h_{i-1} \frac{n_2}{n_1} + h_i \frac{n_3}{n_4} \right) H_x(i, j-1) + \\ & + \frac{1}{4h_{i-1}} \left[k_j \left(\frac{n_2}{n_1} + \frac{n_3}{n_4} \right) + k_{j-1} \left(\frac{n_2}{n_1} + \frac{n_3}{n_4} \right) \right] H_x(i-1, j) + \\ & + \frac{1}{4h_i} \left[k_j \left(\frac{n_2}{n_1} + \frac{n_3}{n_4} \right) + k_{j-1} \left(\frac{n_1}{n_2} + \frac{n_4}{n_3} \right) \right] H_x(i+1, j) \\ & - \left[\frac{1}{2k_j} \left(h_{i-1} \frac{n_2}{n_1} + h_i \frac{n_3}{n_4} \right) + \frac{1}{2k_{j-1}} \left(h_{i-1} \frac{n_2}{n_1} + h_i \frac{n_3}{n_4} \right) \right] \\ & + \frac{k_j}{4h_{i-1}} \left(\frac{n_2}{n_1} + \frac{n_3}{n_4} \right) + \frac{k_{j-1}}{4h_{i-1}} \left(\frac{n_2}{n_1} + \frac{n_3}{n_4} \right) \\ & + \frac{k_j}{4h_i} \left(\frac{n_2}{n_1} + \frac{n_3}{n_4} \right) + \frac{k_{j-1}}{4h_i} \left(\frac{n_1}{n_2} + \frac{n_4}{n_3} \right) \\ & + \frac{k^2}{4} (k_{j-1} + k_j) (h_{i-1} n_1 n_2 + h_i n_3 n_4)] H_x(i, j) \\ & + 0.5 \left(\frac{n_2}{n_1} - \frac{n_1}{n_2} \right) H_y(i-1, j) + 0.5 \left(\frac{n_4}{n_3} - \frac{n_3}{n_4} \right) H_y(i+1, j) \\ & - \left[0.5 \left(\frac{n_2}{n_1} - \frac{n_1}{n_2} \right) + 0.5 \left(\frac{n_4}{n_3} - \frac{n_3}{n_4} \right) \right] H_y(i, j) \\ & = \beta^2 \left[\frac{h_{i-1}}{4} \left(k_j \frac{n_2}{n_1} + k_{j-1} \frac{n_1}{n_2} \right) + \frac{h_i}{4} \left(k_j \frac{n_3}{n_4} + k_{j-1} \frac{n_4}{n_3} \right) \right] H_x(i, j) \end{aligned} \quad (8)$$

$$\frac{1}{2h_{i-1}} \left(k_{i-1} \frac{n_3}{n_2} + k_j \frac{n_4}{n_1} \right) H_y(i-1, j) + \frac{1}{2h_i} \left(k_{i-1} \frac{n_3}{n_2} + k_j \frac{n_4}{n_1} \right) H_y(i+1, j) +$$

$$\begin{aligned}
& + \frac{1}{4k_{j-1}} \left[h_{i-1} \left(\frac{n_3}{n_2} + \frac{n_4}{n_1} \right) + h_i \left(\frac{n_2}{n_3} + \frac{n_1}{n_4} \right) \right] H_y(i,j-1) + \\
& + \frac{1}{4k_j} \left[h_{i-1} \left(\frac{n_3}{n_2} + \frac{n_4}{n_1} \right) + h_i \left(\frac{n_2}{n_3} + \frac{n_1}{n_4} \right) \right] H_y(i,j+1) \\
& - \left[\frac{1}{2h_{i-1}} \left(k_{i-1} \frac{n_3}{n_2} + k_j \frac{n_4}{n_1} \right) + \frac{1}{2h_i} \left(k_{i-1} \frac{n_2}{n_3} + h_i \frac{n_1}{n_4} \right) \right] \\
& + \frac{h_i}{4k_{j-1}} \left(\frac{n_3}{n_2} + \frac{n_4}{n_1} \right) + \frac{h_i}{4k_{j-1}} \left(\frac{n_2}{n_3} + \frac{n_1}{n_4} \right) \\
& + \frac{h_i}{4k_{j-1}} \left(\frac{n_3}{n_2} + \frac{n_4}{n_1} \right) + \frac{h_i}{4k_{j-1}} \left(\frac{n_2}{n_3} + \frac{n_1}{n_4} \right) \\
& + \frac{k^2}{4} (h_{i-1} + h_i) (k_{j-1} n_3 n_2 + k_j n_1 n_4)] H_y(i,j) \\
& - 0.5 \left(\frac{n_3}{n_2} - \frac{n_2}{n_3} \right) H_x(i,j-1) - 0.5 \left(\frac{n_1}{n_4} - \frac{n_4}{n_1} \right) H_x(i,j+1) \\
& + \left[0.5 \left(\frac{n_3}{n_2} - \frac{n_2}{n_3} \right) + 0.5 \left(\frac{n_1}{n_4} - \frac{n_4}{n_1} \right) \right] H_x(i,j) \\
& = \beta^2 \left[\frac{k_{j-1}}{4} \left(h_{i-1} \frac{n_3}{n_2} + h_i \frac{n_2}{n_3} \right) + \frac{k_j}{4} \left(h_{i-1} \frac{n_4}{n_1} + h_i \frac{n_1}{n_4} \right) \right] H_y(i,j) \tag{9}
\end{aligned}$$

We restate the equations (8) and (9) in terms of matrices as:

$$CU = \lambda BU \tag{10}$$

or

$$\begin{bmatrix} C_{xx} & C_{yx} \\ C_{xy} & C_{yy} \end{bmatrix} \begin{bmatrix} H_x \\ H_y \end{bmatrix} = \lambda \begin{bmatrix} B_{xx} & \\ & B_{yy} \end{bmatrix} \begin{bmatrix} H_x \\ H_y \end{bmatrix} \tag{11}$$

where C_{xx} and C_{yy} are banded matrices, each a block tridiagonal matrix which is similar to a tridiagonal matrix with two sets of off-tridiagonal elements on the upper and low tridiagonal respectively. C_{xy} and C_{yx} are

a three-diagonal matrix, and both B_{xx} and B_{yy} are each a diagonal matrix in which only the diagonal elements are nonzero. This eigenvalue problem can be easily transformed to the standard eigenvalue problem given by:

$$A x = \lambda x \quad (12)$$

where $A = B^{-1} C$ and $x=U$.

3.3. Numerical Technique

For a dielectric waveguide, only the guided modes are of significance, which implies that the few largest positive eigenvalues are desired. The Arnoldi method [3.9] can be used to efficiently compute these few eigenvalues and the corresponding eigenvectors of the matrix A of size $n \times n$ for the guided modes.

The Arnoldi algorithm is based on the Arnoldi recursion for reducing a real asymmetric matrix A to an upper Hessenberg matrix. The basic Arnoldi procedure can be viewed as the Gram-Schmidt orthogonalization of the Krylov subspace basis $\{q_1, Aq_1, \dots, A_{m-1}q_1\}$. Furthermore, for each m ,

$$H_m = Q_m^T A Q_m \quad (13)$$

is the orthogonal projection of A onto the subspace spanned by the Arnoldi vectors $Q_j = \{q_1, \dots, q_m\}$ such that $Q_m^T Q_m = I_m$ where I_m is the identity matrix of order m . The upper Hessenberg H_m matrix is formed in the Arnoldi algorithm. The eigenvalues of the upper Hessenberg matrices H_m are called Ritz values of A (in Q_m). Several of the extreme eigenvalues of A , i.e., several of the algebraically-largest or algebraically-smallest of the eigenvalues of A , are well approximated by eigenvalues of the matrices H_m . The Ritz vector $Q_m Z$ ($=x$) obtained from an eigenvector Z of a given H_m is an approximation to a corresponding eigenvector of A . Based on the Arnoldi method [3.9], we form matrices H of size $m \times m$ and a matrix V of size $n \times m$, where m is much smaller than n . The extreme eigenvalues λ_1^m of H are approximations of the extreme eigenvalues of A . Let μ be an extreme eigenvalue (of largest or smallest size) of H and Z the corresponding eigenvector. Then μ is an approximation to an extreme eigenvalue of A and VZ is its corresponding eigenvector. The error predicted from the Arnoldi method [3.14] can be evaluated by

$$\|(A - \mu I)VZ_i\| = h_{m+1,m} e_m^T Z_i \quad i=1, \dots, m, \quad (14)$$

where $e_m^T = (0, \dots, 1)$ and Z_i is the i th eigenvector of H . This evaluation can be used in a stopping criterion.

After having obtained the first largest positive eigenvalue λ_1 , we can compute the second largest eigenvalue by using a deflation [3.10] process.

Let

$$A_1 = A - \lambda_1^m (VZ_1)^T VZ_1 \quad (15)$$

As a consequence of the Schur-Wielandt [3.10] deflation, the largest eigenvalues of A_1 is an approximation to the second largest positive eigenvalue of A . Repeating this process we can accurately approximate several positive eigenvalues of the matrix A .

For a diagonally dominant matrix (true for strong guided modes), the convergence of the Arnoldi process is rapid. However, for the case where diagonal dominance no longer exists (weakly guided modes), acceleration of the convergence of the eigenvalue calculation is needed. We accelerate the modified Arnoldi process by the inverse power method [3.11]. First we apply the Arnoldi method to get an approximation to the (current) largest positive eigenvalue μ and the corresponding eigenvector Z . We then apply the inverse power method by iteratively solving linear systems of the form

$$(A - \mu I) x = b \quad (16)$$

using the s-step orthomin(k) method [3.12]. The standard orthomin(k) method did not work well in the weakly guided case due to the lack of diagonal dominance in A . This inverse power technique significantly enhances the accuracy in the approximation of the eigenvalues and eigenvectors.

The numerical technique is suitable for a very large and sparse matrix, and is also flexible for different discretization methods. It is presumed that this method will be more powerful with preconditioning either in the Arnoldi method (Polynomial) or in the inverse iteration (ILU). Currently we use this method to analyze step index profile dielectric waveguides. It is also suitable for continuously variable index profile waveguides, by using the first-order approximation of a Taylor expansion of the index.

3.4. Test examples

In order to exam this numerical technique of waveguide analysis and calculation for accuracy and efficiency, we used two different dielectric waveguide structures which are representative of dielectric waveguides selected for the purpose of comparison with previously published numerical approaches [3.5-3.7].

The spacing of the mesh in the clad layers is exponentially increased, and uniform in the guided region. We use a 64×64 node mesh for all of the three structures. All the computations were carried out on a CRAY X-MP.

The first example is a square dielectric waveguide (see Figure 3.2). The transverse mode structure is invariant under 90 degree rotation, so first two largest positive eigenvalues, TE_{11} and TM_{11} (or H_{11}^y and H_{11}^x), are degenerate (the solid line shown in Figure 3.2). The normalized propagation constant vs. normalized frequency is shown in Figure 3.2.

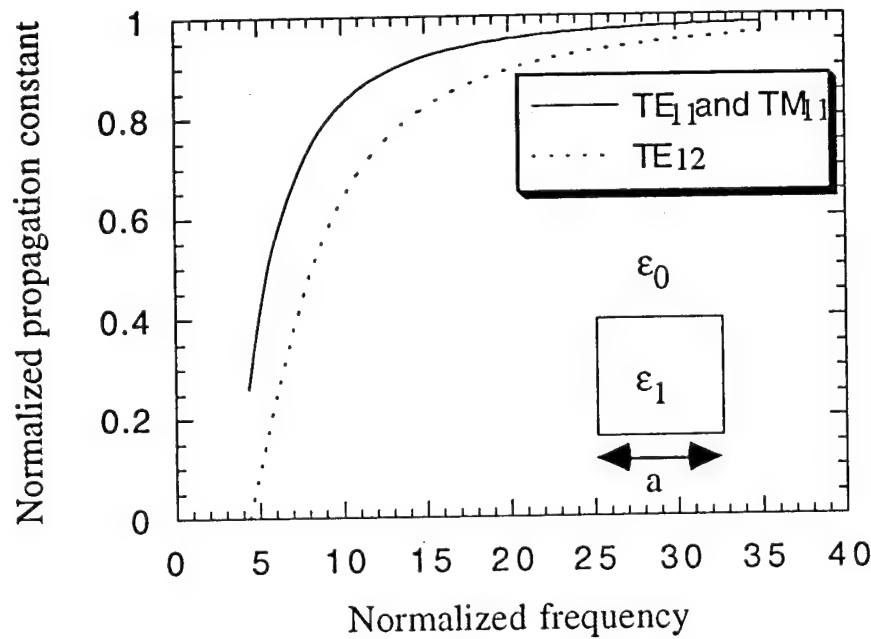


Figure 3.2. A square waveguide. Normalized propagation constant $B = ((\beta/k)^2 - \epsilon_0) / (\epsilon_1 - \epsilon_0)$ vs. normalized frequency $V = ka(\epsilon_1 - \epsilon_0)^{1/2}$, k is the free space wave vector, $a = 1\mu\text{m}$, $\epsilon_1 = 13.1\epsilon_0$

We compute only the first three eigenvalues at each given frequency. The average CPU time is about 14 seconds. As the frequency decreases, the waveguide tends to cut off all the guided modes, the fundamental TE (or TE_{11}) and TM (or TM_{11}) mode are cut off at last as shown in figure 3.2. Our calculation for this structure without the use of the inverse power method converges rapidly, and yields a norm residual less than 10^{-11} , where a norm residual is defined as $\|Ax - \lambda x\|$. This norm residual agrees with the prediction from the modified Arnoldi method

[3.9,3.14]. Our results also agree with the previously published results from others using different numerical approaches [3.5-3.7]. Figure 3.3 and Figure 3.4 show the H_x component distributions for the fundamental and first mode respectively. They are well confined in the guided region, and rapidly decaying in the clad layers.

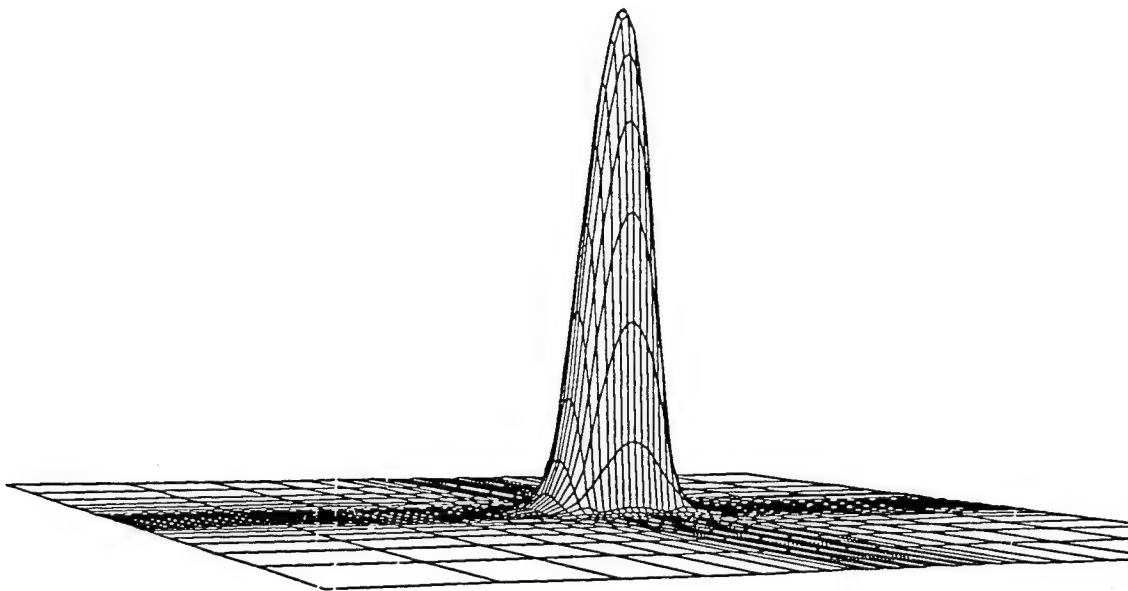


Figure 3.3. The distribution of H_x for the fundamental mode of the square dielectric waveguide.

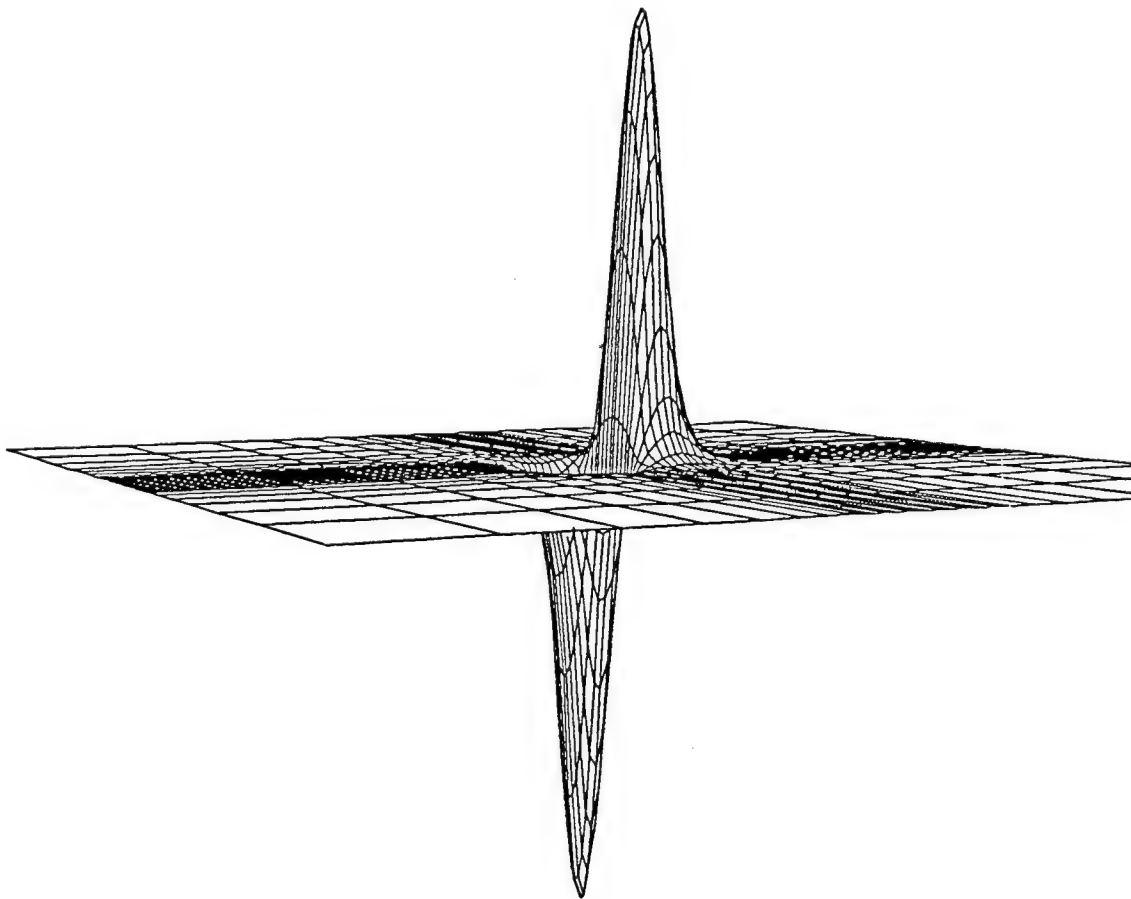


Figure 3.4. The distribution of H_x for the first mode of the square dielectric waveguide.

The second example is a channel waveguide, Figure 3.5 shows the waveguide structure and the normalized propagation constant vs. the normalized frequencies. The first three modes are computed in the wavelength range of micron meters. As the frequency decreases, the propagation constants of the fundamental modes, TE and TM, separate even more, these two fundamental modes evolve nondegeneracy from degeneracy. The higher order mode is cut off first while frequency decreases. Figure 3.6 and Figure 3.7 show the H_x component distribution for the fundamental and first modes. The average CPU time consumed is about 17 seconds for one set of eigenvalues at each given frequency. Our results agree well with previously reported results [3.5,3.7].

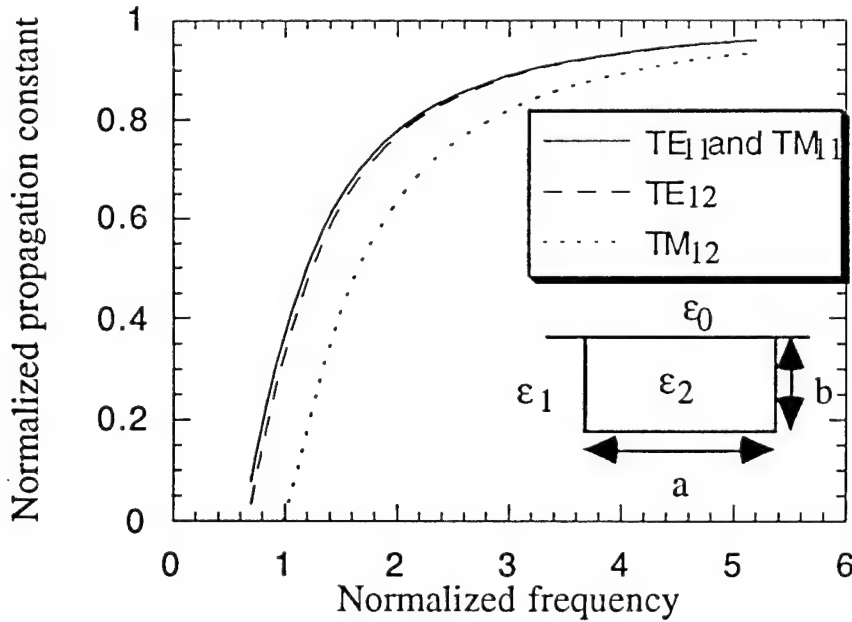


Figure 3.5. A channel waveguide. Normalized propagation constant $B = ((\beta/k)^2 - \epsilon_1) / (\epsilon_2 - \epsilon_0)$ vs. normalized frequency $V = 2b(\epsilon_2 - \epsilon_0)^{1/2} / \lambda$, λ is the free space wave length, $a = 2b = 6\mu\text{m}$, $\epsilon_1 = 2.13\epsilon_0$, $\epsilon_2 = 2.25\epsilon_0$.

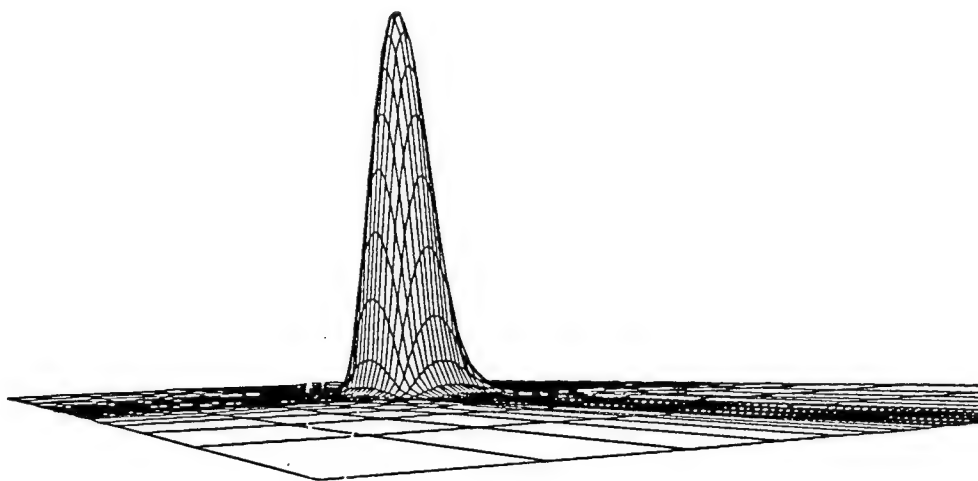


Figure 3.6. The distribution of H_x for the fundamental mode of the channel waveguide.

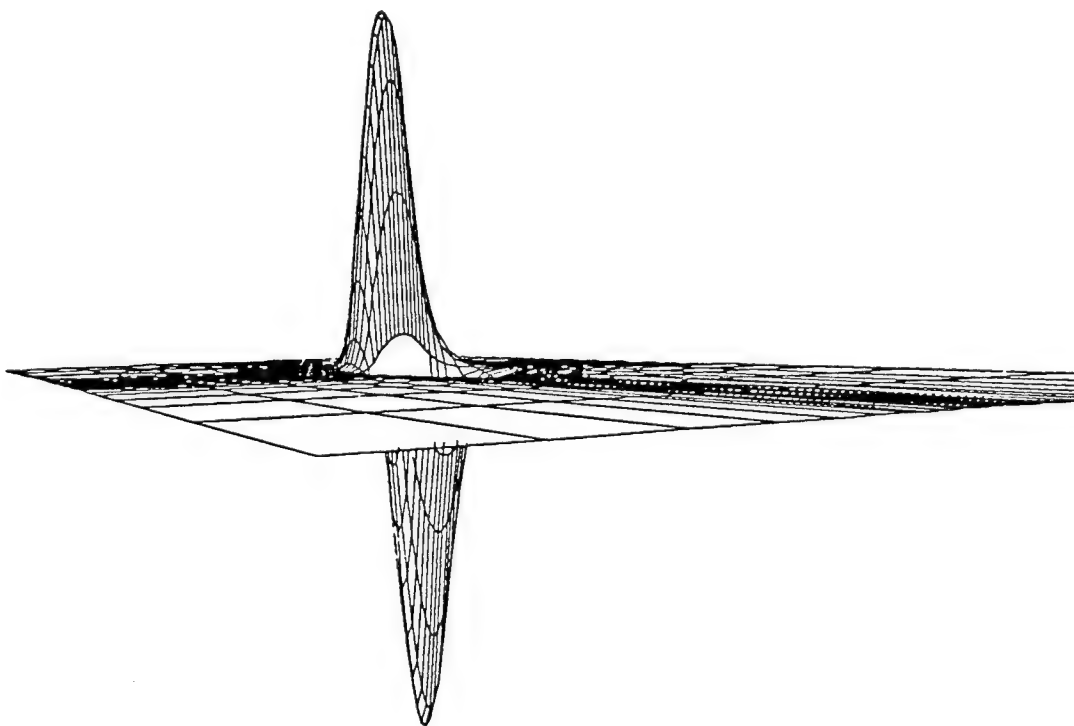


Figure 3.7. The distribution of H_x for the first mode of the channel waveguide.

The two examples show multi-mode behavior with strongly guided modes. The corresponding matrices tend to be diagonally dominant, and the magnitude of the negative eigenvalues is two orders larger than the positive eigenvalues. The convergence of computations for the eigenvalues is fast, even without using an inverse power method.

3.5. Waveguide design for the active optical switches.

The waveguide used for the active optical switches is a single mode multiple quantum well ridge waveguide. The aims of the design for this waveguide are: the waveguide maintains a single mode structure with a wide range of parameters of the ridge structure, the range can be tolerant of fabrication errors; the waveguide is a single mode structure for the range of wavelengths which we are interested in; the waveguide is insensitive to the input signal polarization by ensuring that fundamental TE and TM modes are degenerate.

Figure 3.8 shows the waveguide structure used in the active optical switches, which is a multiple quantum-well single mode ridge waveguide. It is composed of three quantum wells separated by two barrier layers, two confinement layer with 20% of aluminum mole fraction, and two cladding layers with 45% of aluminum mole fraction. The separated confinement layers, quantum wells, and barrier layers under the ridge form the guided region. The transverse confinement is from the difference of refractive indices between cladding layers and guided region. The difference forms strong guiding along the transverse direction. The lateral confinement is from the ridge structure, and determined by the ridge height and width, which is a weak guided structure. The number of guided modes supported by the ridge waveguide and optical field distribution inside the waveguide are basically determined by the two parameters, ridge height and width, with quantum well layer structure (which is usually fixed).

The refractive index of $\text{Al}_x\text{Ga}_{1-x}\text{As}$ ($0 \leq x \leq 1.0$) is the function of the mole fraction of Aluminum and wavelength. The function has been well studied in reference [3.15]. Expression of the refractive index as a function of Aluminum mole fraction and wavelength is given [3.15]:

$$n^2 = 10.906 - 2.92 x + \frac{0.97501}{\lambda^2 - c} - 0.97501 \lambda^2 \quad (17)$$

where x is Aluminum mole fraction, λ is wavelength in micrometer, and c is:

$$\begin{aligned} c &= (0.52886 - 0.735 x)^2 & (0 \leq x \leq 0.36) \\ &= (0.30386 - 0.105 x)^2 & (0.36 < x \leq 1.0) \end{aligned} \quad (18)$$

We assume that the waveguide is a dielectric waveguide with no attenuation to optical signals and thus, the structure is analyzed at transparency. The waveguide width was chosen 3 micrometer, which can be easily fabricated in the Microelectronics Laboratory for Research and Education, University of Minnesota, without the need for developing any further fabrication techniques. We calculated the range of the ridge heights for supporting only the fundamental TE and TM modes, which is from 0.8 micrometer to 1.0 micrometer. The tolerance, of 0.2 micrometer, for single mode structure is much larger than the error which may occur during the fabrication. We chose 0.9 micrometer ridge height as the designed height as shown in figure 3.8. The optical field

confinement of the structure is about 9%. With 0.9 micrometer ridge height, we calculated the parameter range of ridge width for single mode structure, which is from 3 micrometers to 5 micrometers. The 2 micrometer tolerance is extremely larger, and more than adequate for errors in fabrication.

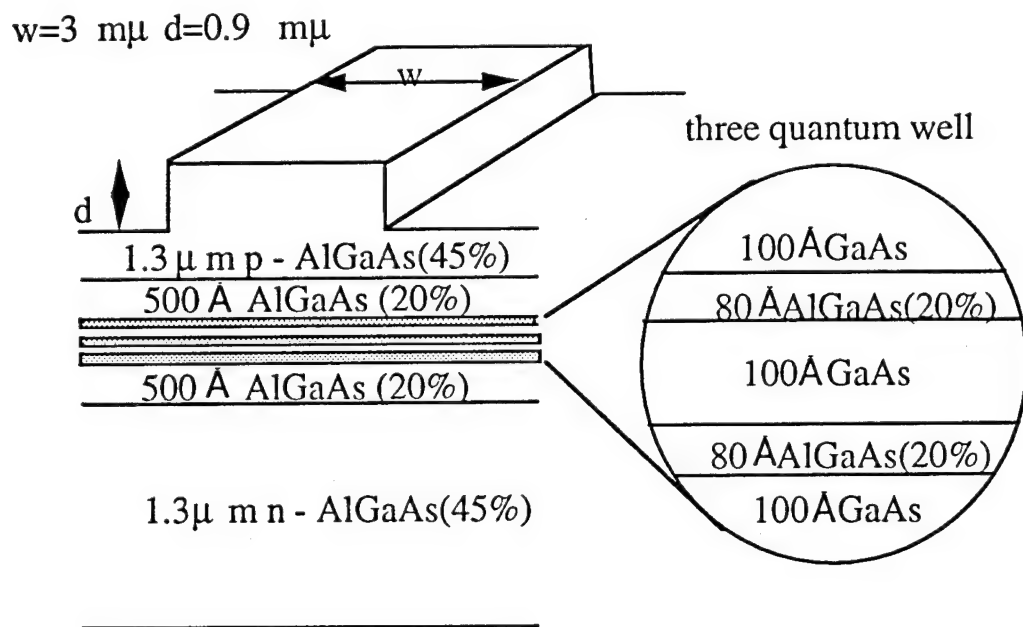


Figure 3.8. A multiple quantum well single mode ridge waveguide, $w=3\mu\text{m}$, $d=0.9\mu\text{m}$.

With 3 micrometer width and 0.9 micrometer height for the ridge waveguide structure, we analyze the propagation constants as a function of frequency to reveal the insensitivity of the waveguide to the TE and

TM modes. The numerical results are shown in Figure 3.9, as the normalized propagation constant vs. normalized frequency. The fundamental TE and TM modes have approximately same propagation constant until the normalized frequency reaches to 1.5. The position of the 860nm wavelength, which is approximate laser wavelength, is marked in Figure 3.9.

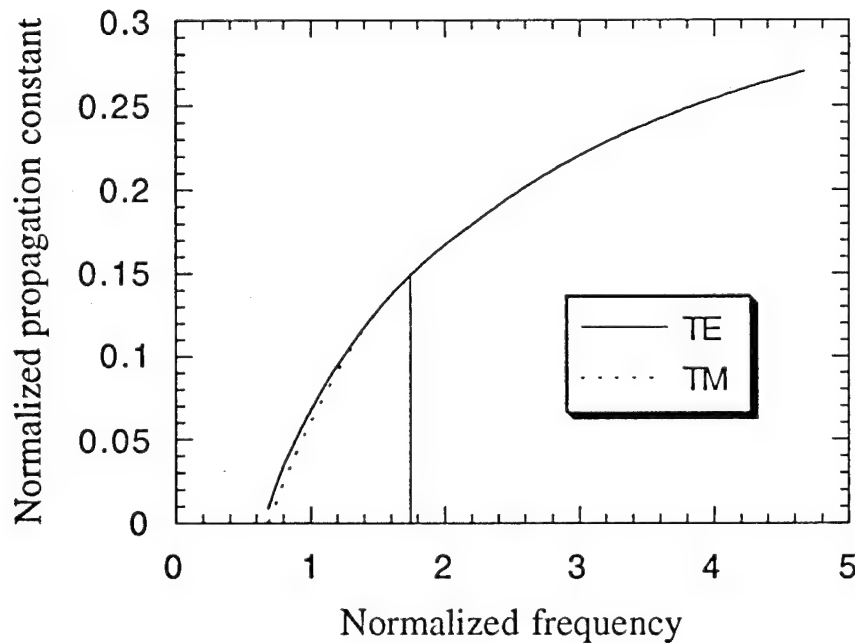


Figure 3.9. Normalized propagation constant $B = ((\beta/k)^2 - \epsilon_{\text{clad}}) / (\epsilon_{\text{core}} - \epsilon_{\text{clad}})$ vs. normalized frequency $V = dk(\epsilon_{\text{core}}^2 - \epsilon_{\text{clad}}^2)^{1/2}$, k is the free space wave vector, ϵ_{clad} is the maximum dielectric constant in the clad layers, the ϵ_{core} is the maximum dielectric constant in the guided region, and d is the thickness of the core.

Figure 3.10 shows the H_x component distribution of the fundamental mode. The field is weakly confined in the lateral direction. Our calculation for this structure needs the acceleration provided by the inverse power method [3.11] to improve the convergence. The maximum norm of the residual is less than 10^{-8} for the first two modes. The average CPU time on a CRAY X-MP for the calculation is about 1 minute. In this calculation, we have neglected the dependence of refractive index on the injected current, as we expect this change is not to be significant.

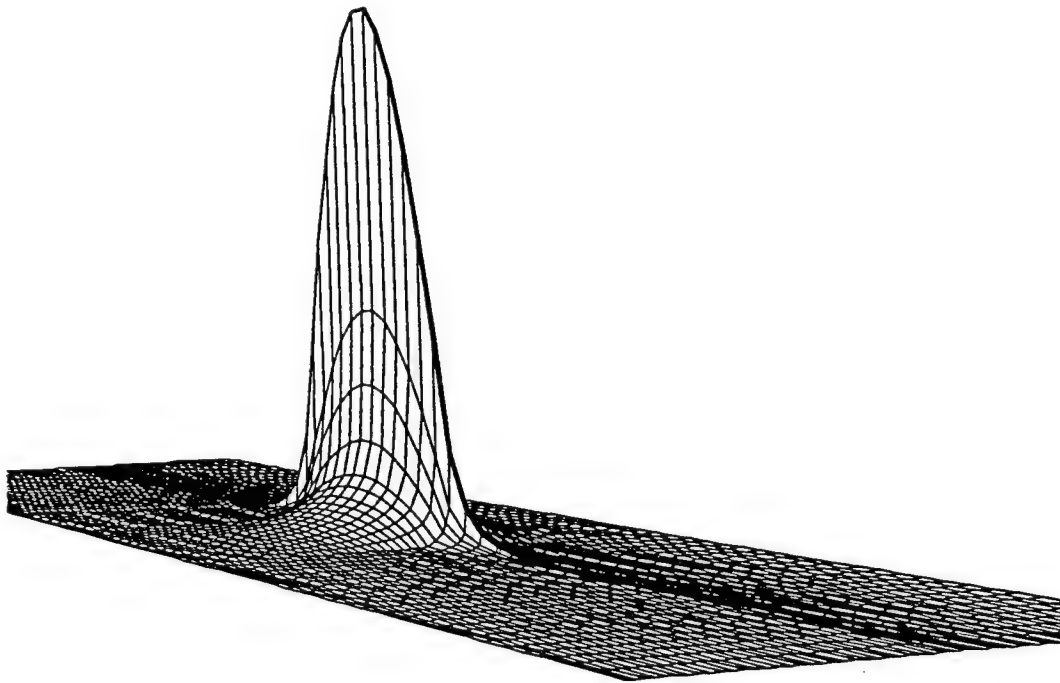


Figure 3.10. The distribution of H_x for the fundamental mode of the quantum well single mode waveguide.

References

- [3.1] E. Goell, 'A circular-harmonic computer analysis of rectangular dielectric waveguides,' *Bell Syst. Tech. J.*, vol. 48, pp. 2133-2160, 1969.
- [3.2] B. M. A. Rahman and J. B. Davies, 'Penalty function improvement of waveguide solution by finite elements,' *IEEE Trans. Microwave Theory Tech.*, vol. MTT-32, pp. 922-928, 1984.
- [3.3] K. Hayata, 'Vectorial finite-element method without any spurious solutions for dielectric waveguiding problems using transverse magnetic-field component,' *IEEE Trans. Microwave Theory Tech.*, vol. MTT-34, pp. 1120-1124, 1986.
- [3.4] Z. Abid, K. Johnson, and A. Gopinath, 'Analysis of dielectric guides by transverse magnetic field finite element,' to appear in *J. Lightwave technol.*
- [3.5] K. Bierwirth, N. Schulz, and F. Arndt, 'Finite-difference analysis of rectangular dielectric waveguide structure,' *IEEE Trans. Microwave Theory Tech.*, vol. MTT-34, pp. 1104-1114, 1986.
- [3.6] N. Schulz, K. Bierwirth, and F. Arndt, 'Finite-difference analysis of integrated optical waveguide without spurious solutions,' *Electron. Lett.*, vol. 22, pp. 963-965, 1986.
- [3.7] A. Galick, T. Kerhoven, and U. Ravaioli, 'Iterative solution of the eigenvalue problem for a dielectric waveguide,' *IEEE Trans. Microwave Theory Tech.*, vol. MTT-40, pp. 699-705, 1992.
- [3.8] R. Varga, Matrix iterative analysis, Prentice-Hall, Englewood Cliff. HJ: Prentice-Hall, 1962.
- [3.9] W. E. Arnoldi, 'The principle of minimized iterations in the solution of the matrix eigenvalue problem,' *Quart. Appl. Math.*, vol. 9, pp. 17-29, 1951.
- [3.10] Y. Saad, Partial Eigensolutions of Large Nonsymmetric matrices Research Report, YALEU/DCS/RR-397, 1985.
- [3.11] G. Golub and C. van Loan, Matrix computations, Baltimore: John Hopkins University Press, 1989.
- [3.12] A. T. Chronopoulos, 's-step iterative methods for (non)symmetric (in)definite linear systems,' *SIAM J. on Num. Anal.*, vol. 28, No. 6, pp. 1776-1789, 1991.
- [3.13] J. S. Hornsby and A. Gopinath, 'Numerical analysis of a dielectric-loaded waveguide with a microstrip line -finite

- difference methods,' *IEEE Trans. Microwave Theory Tech.*, vol. MTT-17, pp. 684-690, 1960.
- [3.14] K. Kim and A. T. Chronopoulos, 'An Efficient Parallel Algorithm for Extreme Eigenvalues of Sparse Nonsymmetric Matrices', *The Int. J. on Supercomputing*, Vol.6, No.1, pp. 98-111, 1992.

CHAPTER 4

FABRICATION

Since the first semiconductor lasers were fabricated [4.1-4.4], their commercial use has been growing very rapidly. The applications of lasers and other optoelectronic devices drive technology to continually find ways to improve the device characteristics, fabrication techniques, and testing procedures. Current technology provides the opportunity for better understanding of semiconductor physics, materials growth and characteristics, and device design, processing and characteristics. The fabrication of active optical switches is based on semiconductor laser fabrication. In this chapter we present the fabrication techniques which have been developed in Microelectronics Laboratory for Research and Education (MLRE) in the University of Minnesota for this project. An overview of material growth and device fabrication will be given in section 4.1. Following this, a few primary techniques will be presented for ohmic contacts, reactive ion etching, gold plated airbridged interconnects, and antireflection coatings.

4.1 Overview of the fabrication

The lattice parameter difference between GaAs and $\text{AlGa}_{1-x}\text{As}$ ($0 \leq x \leq 1.0$) is very small (less than a few percent at 300K). Single-crystal wafers of GaAs with the 100 plane are used as the seed to grow several

layers of materials with the same lattice constant, but of different composition, to provide a heterostructure for carrier confinement and optical field confinement. Epitaxial growth is the technique of getting chemicals in either the liquid or gas phase to react, condense, or precipitate onto a substrate, growing a crystal atomic layer by atomic layer, that continues the substrate's crystal lattice. The difficulty lies in growing a layer of crystal that is nearly defect-free, of a precise thickness, and of a particular composition. The growth technique first developed was liquid phase epitaxy (LPE). In spite of its success in growing a good crystal structures, the liquid phase epitaxy process has a multitude of interactions that must be precisely controlled. Molecular beam epitaxy (MBE) is basically an evaporator with heated crucible of the crystal components and suitable shutters in an ultra high vacuum system. The thermally evaporated molecules travel by line of sight to the substrate, where they condense to grow additional crystal layers. The crystal composition is controlled by the temperatures of the crucibles, and thus by the relative evaporation rates.

The active optical switches were fabricated on wafers of GaAs semi-insulating substrate, and MBE was used to grow the layer structure. Sixteen pairs of AlGaAs/GaAs (20nm/20nm) super lattice were grown to minimize the defects migration from the substrate, and subsequently the designed structure was grown. The dopants were Si and Be for n-type and p-type respectively. The substrate temperature was 580°C, 600°C, and 650°C for GaAs, Al_{0.2}Ga_{0.8}As, and Al_{0.45}Ga_{0.55}As, respectively. Since highly doped p-type GaAs (5×10^{19}) layer was used as the last layer

for better ohmic contact, the wafer had a hazy appearance. All the wafers used in our device fabrication were grown in the MBE system at the University of Minnesota.

The goals of device processing are to provide electronic and optical confinement, electrical contacts, isolation, and mounting surfaces. The processing sequence depends on the device structure, and here we focus on the simple ridge structure, shown in Figure 4.1.

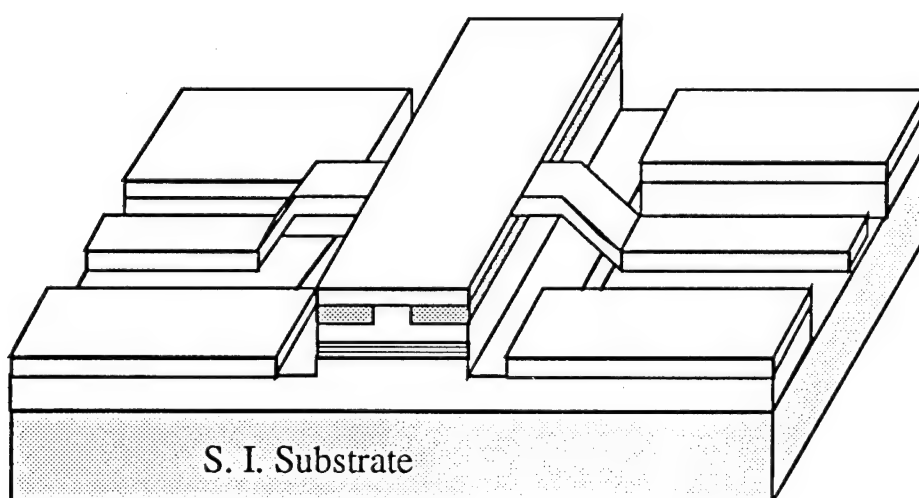


Figure 4.1. The device structure corresponding to the fabrication flow chart.

The size of mask layout for the switches was 1 cm square. The waveguides were in lengths of 8 mm, and thus fitted into an 8 mm square, with four sets of alignment marks at each corner. The ohmic contact test patterns and etching depth test patterns filled out the remaining space

around the 8 mm square. Figure 4.2 shows the mask layout of p-type and n-type ohmic contacts, and ridge etching.

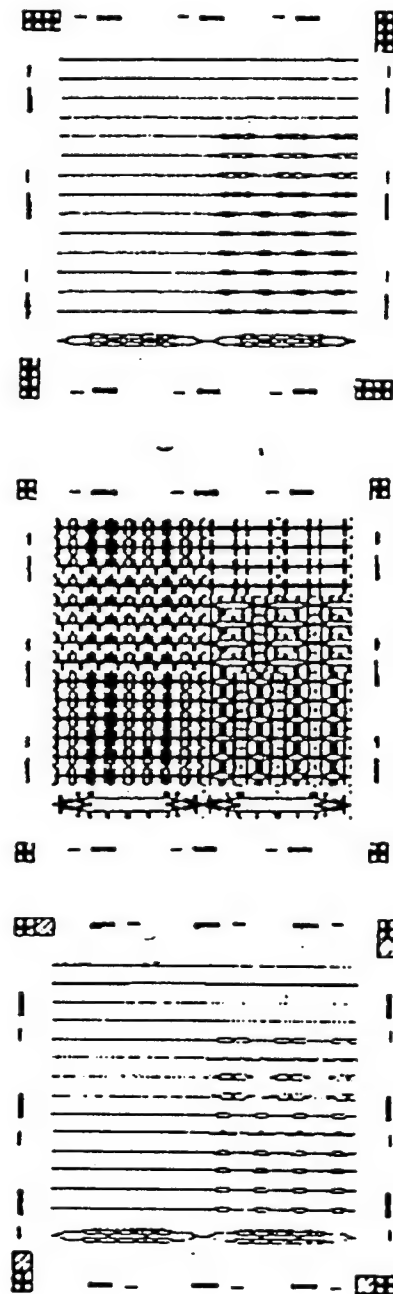


Figure 4.2. Mask layout for p-type and n-type ohmic contacts, and ridge etching.

Figure 4.3 shows the fabrication flow chart. It shows the processing for p-type and n-type ohmic contacts, ridge etching, device etching, isolation etching, and gold plating for the bridges. The fabrication started with the p-type ohmic contact which has the smallest dimension with a 2 μm wide stripe of the p-type ohmic contact metal on the flat wafer. Lift-off was used to form the Mn/Au p-type ohmic contact pattern (see figure 4.3(a)). Then, plasma-enhanced chemical vapor deposition (PECVD) was used to deposit 2000Å of SiO_2 film for the ridge etching mask. The mask pattern was defined by photolithography and formed by buffered HF etching of the SiO_2 film (see figure 4.3(b)). The ridge was next etched by reactive ion etching (RIE) with BCl_3 (see figure 4.3(c)). The device area was next etched out by the wet chemical etching of $\text{N}_4\text{HOH}/\text{H}_2\text{O}_2/\text{H}_2\text{O}$ (see figure 4.3(d)). Then n-type ohmic contact pattern of AuGeNi was formed by liftoff (see figure 4.3(e)). The isolation of the switches was accomplished by the wet chemical etching (see figure 4.3(f)). The gold plating technique was used to build the air bridge for the interconnect between the ridge and contact pads on the semi-insulating substrate (see figure 4.3(g)).

After the gold plating, the wafer was thinned down to about 150 μm thick, and then cleaved. The antireflection (AR) coating of single layer SiO was deposited on all facets by electron beam deposition.

The techniques used in our fabrication and discussed here are ohmic contact, RIE, gold plating, and AR coating.

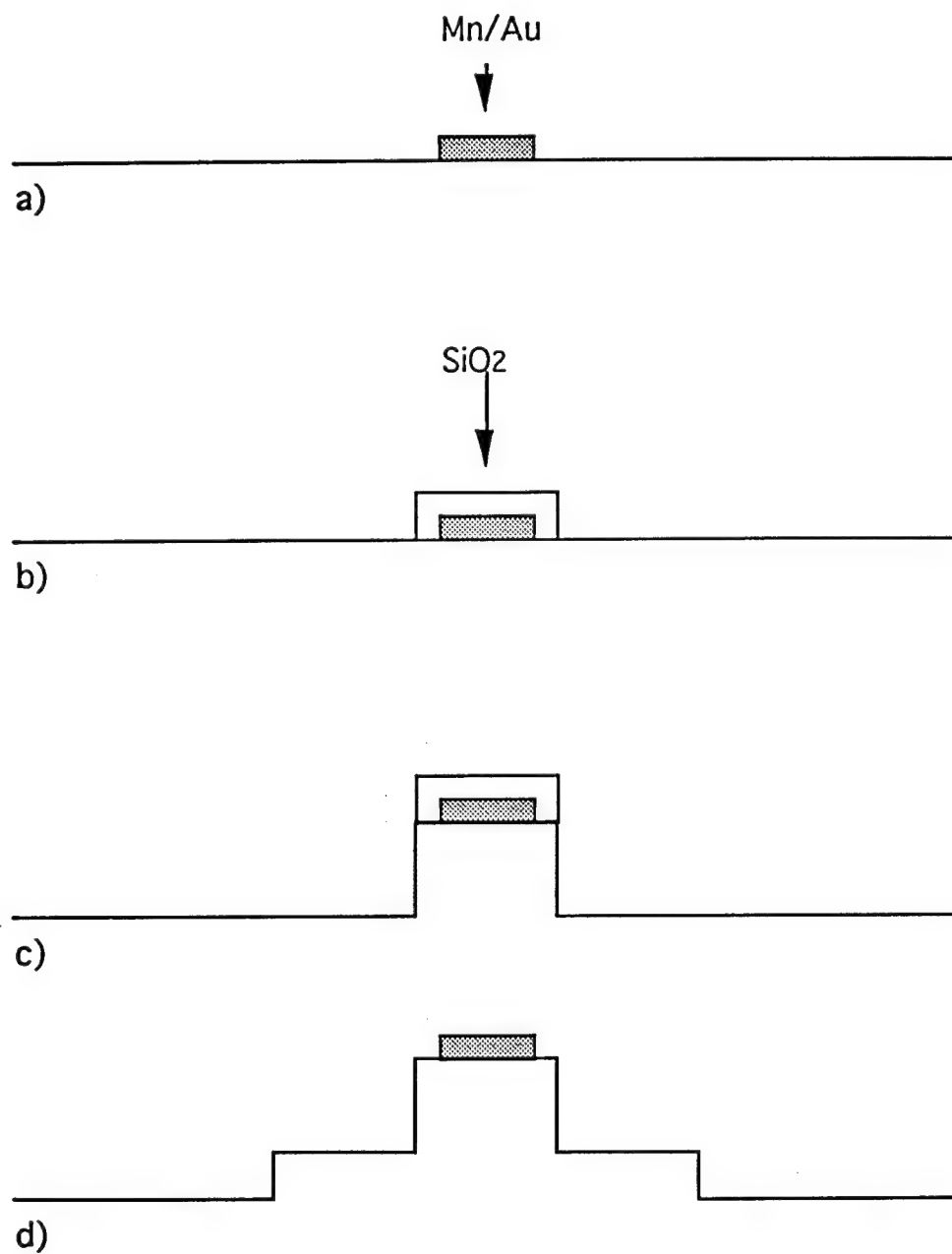


Figure 4.3. Fabrication flow chart.

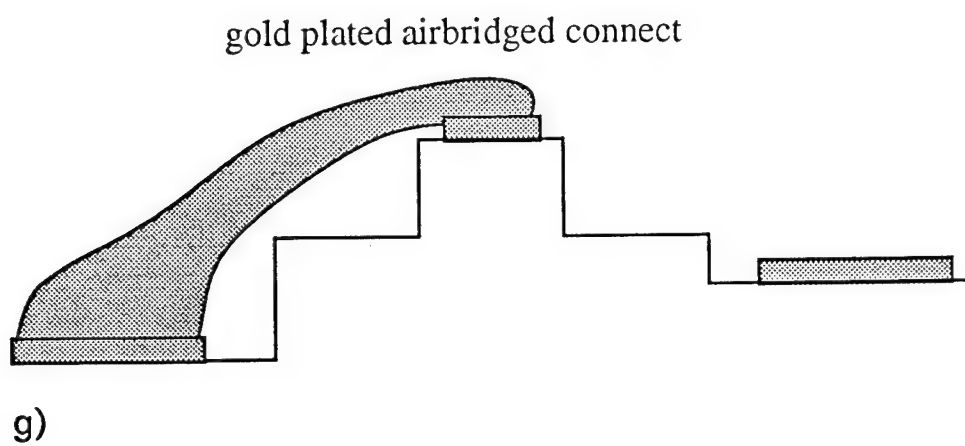
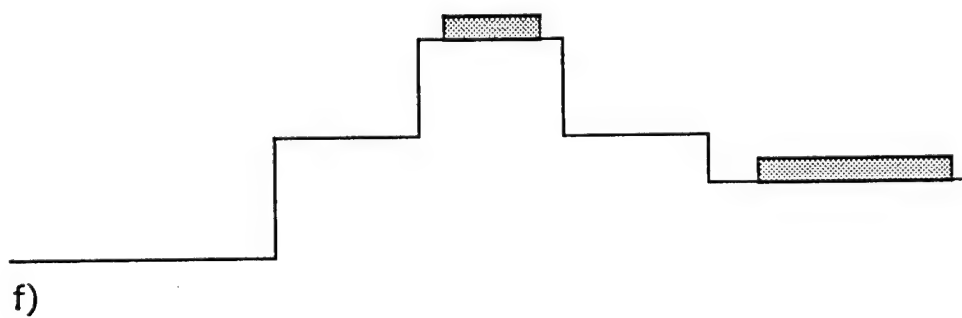
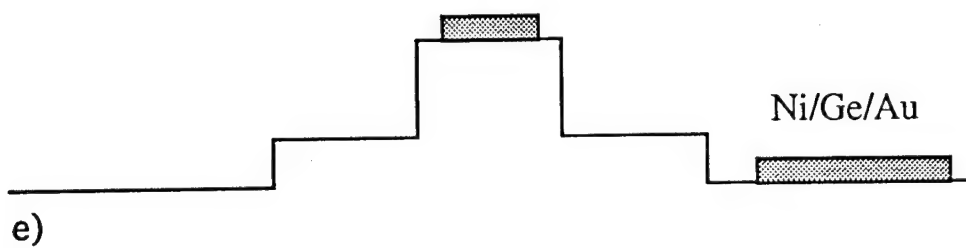


Figure 4.3. continued

4.2. Ohmic contacts

The function of an ohmic contact on a semiconductor device is to provide electrical conduction in or out of the device. Therefore, the contact should have a linear I-V characteristic with little resistance for DC current and small parasitics for radio frequency (RF). Intuitively, the idea of the fabrication for the ohmic contact is rather simple. However, simply placing a metal in contact with a III-V semiconductor such as GaAs generally results in a rectifying contact (a diode) rather than an ohmic contact. Thus, the technology of obtaining low resistance ohmic contacts has received a great amount of research and development effort. A general overview can be found in various references [4.5-4.11]. For our active optical switch fabrication of ohmic contacts, we have to fabricate the p-type ohmic contact first by taking advantage of the planar surface of the wafer since the p-type contact strip has the smallest width. The best alloy temperatures for p-type and n-type ohmic contacts are 350°C and 400°C respectively. The p-type ohmic contact cannot be alloyed before alloying n-type ohmic contact due to the higher alloy temperature of n-type ohmic contact. Therefore, the p-type and n-type contacts have to be alloyed at the same time, and at a same temperature suitable for both types of ohmic contacts.

The principal strategy employed to achieve an ohmic contact is to dope the surface of semiconductor sufficiently high to ensure that the dominant conduction mechanism is by field emission (tunneling). The contact resistance is a strong function of the doping concentrations. In

order to reduce the contact resistance, ion-implantation or a highly doped GaAs epitaxial layer (also called cap layer) is generally used. For laser fabrication the latter is the better choice, since ion-implantation is a complicated process. The most common approach to fabricate an ohmic contact on GaAs is to deposit an appropriate metallization to the wafer (usually patterned by photolithography) and alloy the metals into GaAs. Deposition of the metals to the surface for the wafer is usually performed by evaporation or sputtering. Either a thermal evaporator or an electron-beam evaporator can be used for this purpose.

To obtain reliable and reproducible contacts, the surface of the GaAs wafer must be kept clean, and free from oxidization before the deposition of the metals is performed. This is usually achieved by wet chemical etching, for example dipping the patterned wafer into chemical solution of $\text{NH}_4\text{OH}:\text{H}_2\text{O}$ (1:5) for a few seconds to remove the oxide layer immediately before the wafer is loaded into the evaporator.

For the p-type ohmic contact, a Mn/Au system was used. The thickness ratio between Mn and Au is given by 4% Mn:96% Au weight ratio, which is the optimum metal composition ratio reported previously [4.12]. 150Å of Mn and 1100Å of Au have been used for the p-type ohmic contact.

The n-type ohmic contact was formed by depositing 50Å of Ni, 300Å of Ge, 500Å of Au, 75Å of Ni, and 1000Å of Au sequentially. The Ni(50Å) is used as a wetting agent to prevent the AuGe from "balling up" during contact alloying, and to help the diffusion of Ge into the GaAs [4.13]. The Ge layer acts as the donor layer for the n-type doping during

alloying. The second Ni (75Å) is deposited to act as a diffusion barrier during alloying process. The deposition of thick Au (1000Å) facilitates the probing or bonding.

After the metallization and before the alloy stage, the wafer is usually soaked in acetone for a liftoff process. An airbrush is sometimes used with acetone to assist the process. This process washes out the metal on unwanted areas as well as photoresist on the wafer. If a thin layer of photoresist (the thickness ratio between photoresist and metal is 3:1) is used, Chlorobenzene soaking is needed before the exposure of photoresist for the enhancement of the liftoff process.

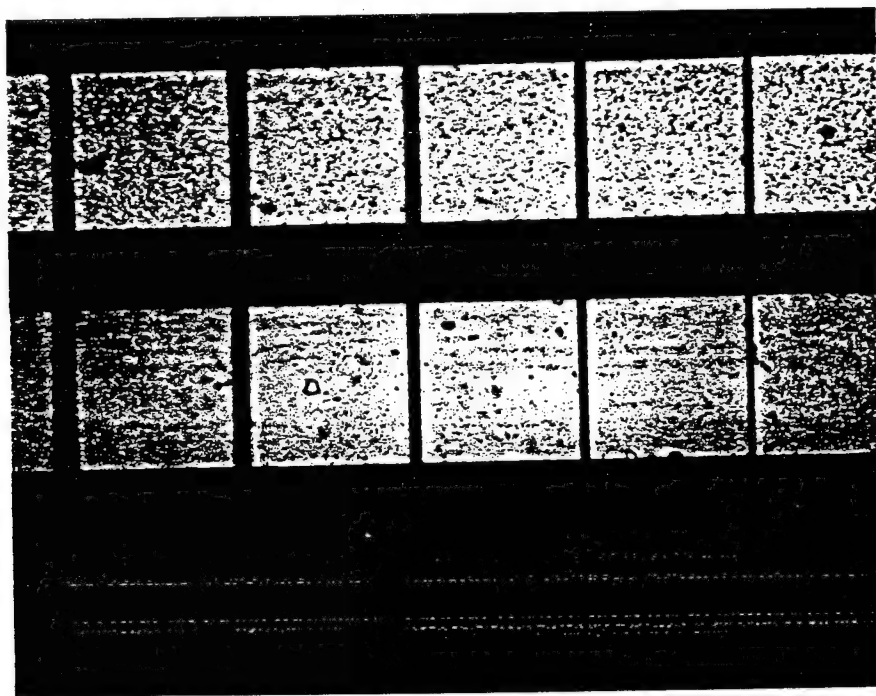


Figure 4.4. The alloyed ohmic contact test pattern for the p-type (top) and n-type (bottom).

The alloy procedure involves heating the wafer until the metallization layers alloy into the GaAs. This is a very complex process which is still not completely understood. The alloying was performed in a Heatpulse 210T RTA system made by A. G. Associates in the forming gas (95% N₂ and 5% H₂). The samples were placed on a 4 inch Si wafer, and put close to a thermocouple to measure the sample temperature accurately. Both types of ohmic contact were alloyed together at 380°C for 10 seconds. The temperature of 380°C is not the best alloy temperature for the both of ohmic contact, and Figure 4.4 shows the alloying differences between them. The top set of micrographics is for the p-type, and appears slightly over-alloyed, and the low set is the n-type, which is under alloyed. The 380°C is the best temperature for the both contacts to obtain reasonably good ohmic contacts simultaneously.

4.3. Reactive ion etching

Reactive ion etching belongs to the dry etching category of etching processes. The basic principle of dry etching is to utilize plasma driven chemical reactions and/or energetic ion beams to remove materials. The advantages of dry etching over the wet etching is that it can provide greater control at reduced cost and offers substantial directionality and etch anisotropy, because etching can proceed more quickly in the vertical direction than the horizontal. The lateral etch rates are very close to zero in some conditions, so undercutting of masking patterns can be greatly reduced. For the cases where the lateral dimensions of etching geometry

are comparable to the etching depth such as in the waveguide structures in our active optical switches, wet chemical etching is not possible due to serious undercutting. Dry etching is essential, since for GaAs processing unlike Silicon processing, there are no liquid etchants that can etch GaAs with little or no undercutting of masking pattern. Dry etching is able to produce much smaller features than wet chemical etching, as well. Dry etching is a rather complex process compared to wet chemical etching, and the quality of the etching is more sensitive to the processing parameters.

RIE and plasma etching are very similar and there is no sharp difference between them. The issues which are applicable to plasma etching are applicable to RIE as well. The principal distinguishing feature for RIE from plasma is that the RIE emphasizes the directionality, which consequently changes with pressure, and configuration of electrodes. The fundamental etching process of RIE is directional ion bombardment, and the reactants are directional. The directionality of RIE can be enhanced by operating the system at lower pressure.

The RIE system which we used in the MRLE at the University of Minnesota is Plasmatherm RIE system. BCl_3 was used as the etching gas. Low pressure (less than 1 mTorr) was maintained during the etching process, and the RF power was kept between 100 and 150 watts.

The etching process which we developed for our RIE system involves low etching rate ranging from approximately 400 Å/min to 600 Å/min, and low sensitivity to wafer size and RF power. After the wafers were etched by the RIE system, wet chemical etching was then

used to polish and stabilize the etched surface. Figure 4.5. shows etched ridge.

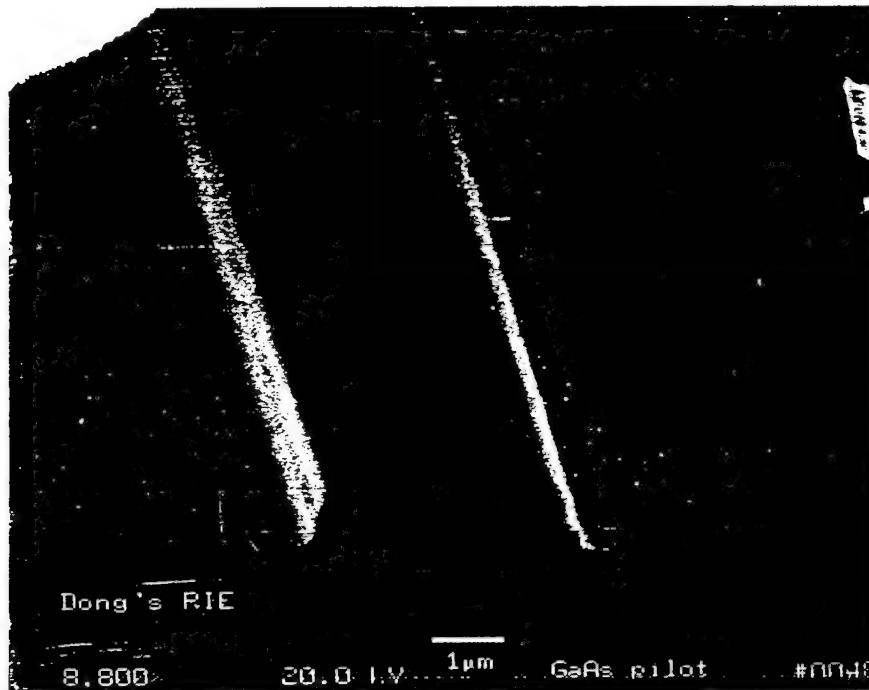


Figure 4.5. Etched ridge by RIE system.

4.4 Airbridged interconnects by gold plating

The interconnects between the ridge top of the p-type contact and the electrode pad are a crucial step for the switch fabrication. The interconnects have to allow current flow into the switches from the top with small resistance. They also have to have low parasitic for RF

signals. Airbridged interconnects were used in our switches to meet these requirements, and they were fabricated by gold plating.

The plating processing provides the interconnects with a thick layer of metal, offering very good conductivity, and the plated electrode pads have a desirable surface for wire bonding. Since the plated interconnects may be several micrometers thick, they may have a small lateral profile along the wafer surface. The parasitics from this type of connection are small, and are not the major limitation on the bandwidth of the switches. Gold metallization has many advantages: it can be plated, has high conductivity, resists oxidation and most acids, and is easily soldered and bonded to.

Gold plating has been a subject of much research, and enormous engineering development [4.14] Here, we only present the gold plating technique which has been developed in MRLE of the University of Minnesota.

The basic idea of electroplating is shown in figure 4.6. There are two basic parameters, current efficiency and throwing power, which are used in electroplating. The current efficiency is the ratio of the weight of deposited metal to that which would be deposited if all the current had been utilized in depositing the metal. Part of the total current might be involved in depositing gases or reducing the ion species due to the electrochemical reaction other than metal deposition. For the bath types which are used in microelectronics the current efficiency usually is close to 100%. The ability of the plating bath to produce deposits of uniform thickness on the arbitrary shape of cathode is called the throwing power.

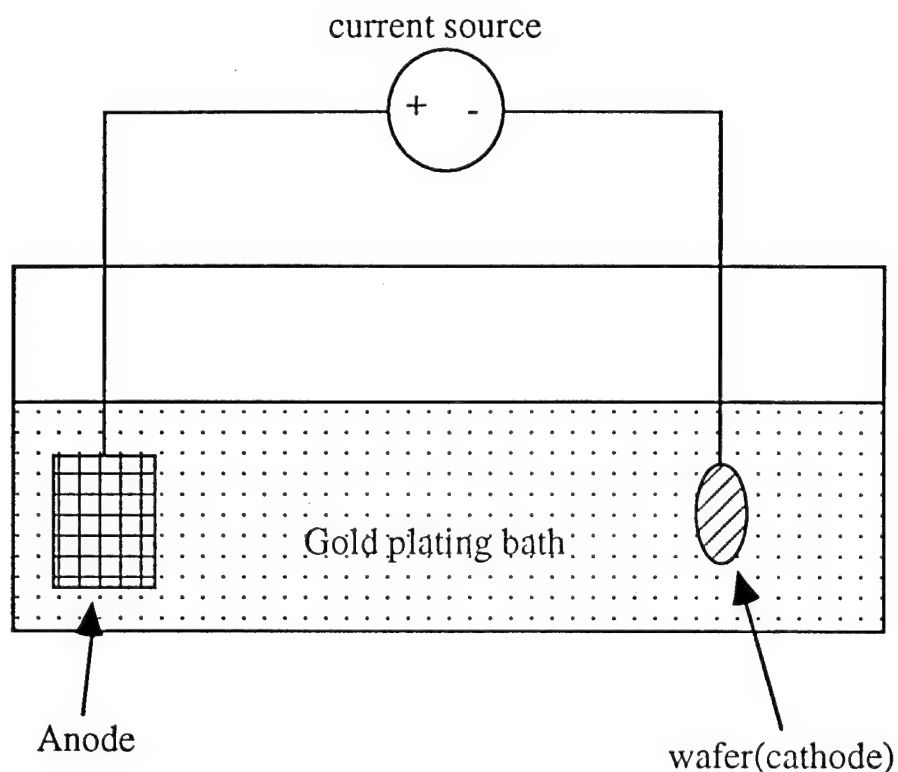


Figure 4.6. Basic concept of gold plating

The gold plating bath which we used in our fabrication is the HMD commercial gold plating bath. Such a plating bath is intended to produce pure gold (>99.99%) and operates at nearly 99% current efficiency. The optimized temperature is about 50°C. The pH and specific gravity have to be maintained constant since the quality of the gold plating is very sensitive to these parameters. These should always be manufactured within the recommended range. Platinum has been chosen as the material of the anode, and the current density was kept on the order of 5mA/cm².

The airbridged connects formed by gold plated air bridges are illustrated in figure 4.7. The two metal pads are at different levels, and the top of the ridge is usually a few micro meters higher than the other. A layer of photoresist is spun and patterned on open areas over the metal pads. Then, a thin layer of metal, Ti/Au:300Å/300Å, is evaporated by an electron beam evaporator over all the patterned surface (see figure 4.7(a)). A second layer of photoresist is coated and patterned for the connects (see figure 4.7(b)). The wafer is baked to assure adequate adhesion for the plating, and then, the open areas are plated (see figure 4.7(c)). After the plating, the top layer of photoresist is removed by the oxygen asher. The thin layer of metal is etched away by ion milling (see figure 4.7(d)). The last layer of photoresist is dissolved by acetone. The plated gold surface is usually rough and soft, and therefore, it is easily wire-bonded to. The plated airbridge may be operated at high current, because of the thick metal bridge. Low parasitics results from the large spacing and low dielectric constant of the intervening medium. Figure 4.8 shows the top view of the ridge waveguide laser with airbridged contacts. The bridge is 75 micrometer wide, the wire-bonding pads are 100×150 micrometer square each, and 150 micrometer apart, which matches a high speed RF probe, and the ridge is 3 micrometer wide, and 500 micrometer long. The gold-plated metal contact on the ridge is 20 micrometer wide, and the thickness of the gold-plated contacts is about 2 micrometers.

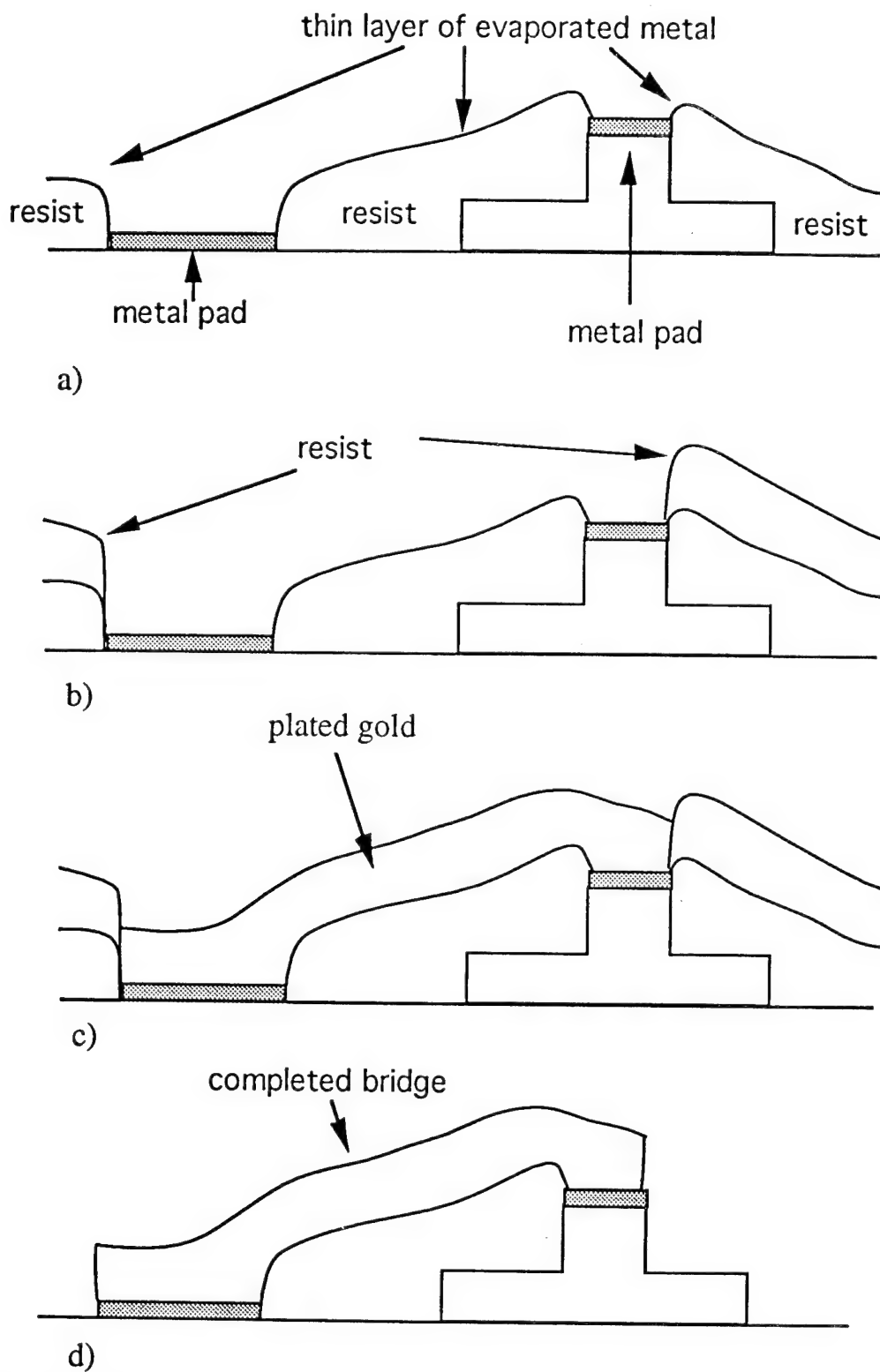


Figure 4.7. Airbridged connect by gold plating.

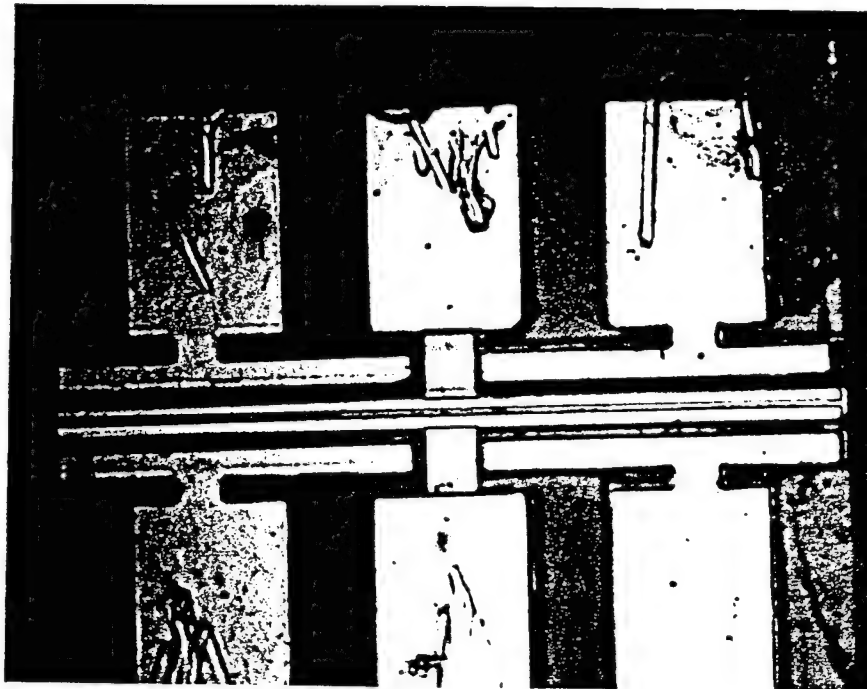


Figure 4.8. Top view of the ridge waveguide laser.

4.5 Antireflection coating

Semiconductor laser amplifiers are semiconductor lasers with antireflection (AR) coatings on their facets, and our optical switches are made in a similar manner. The loss from each facet of the optical switches can be reduced selectively over narrow wavelength bands by applying appropriate thin-film coatings or by using sophisticated design techniques to tailor spectral reflectivity over a broad range of wavelengths. Here, we only consider single layer thin film AR coating, and narrow band operation of simplicity.

When light strikes a thin film coated the surface, the system can be described by applying Maxwell's equations and appropriate boundary conditions. Although this concept is straightforward, the calculations are complicated and can be tedious. A matrix approach has been presented in numerous publications (e.g., [4.15-4.16]). The matrix approach uses Maxwell's equations and properties of optical impedance and admittance. By equating the tangential components of electric and magnetic field vectors on both sides of a thin boundary and by expressing the change in the admittance as a function of layer depth, even the most complex thin-film structure can be represented in a compact form that is easily programmed.

A single-layer thin-film has been used in our system. The coated film acts like a quarter-wave impedance transformer. Its refractive index satisfies

$$n_2 = (n_1 n_3)^{1/2} \quad (1)$$

where n_1 and n_3 are the refractive indices of the materials on both sides of the thin film, respectively. n_2 is the refractive index of the coated film. The thickness of the coating is

$$d = (2n + 1) \lambda / 4 \quad (n=0,1,2,\dots) \quad (2)$$

where λ is the wavelength.

Thin-film coatings are prepared by evaporating the source material to be deposited on target surface. Physical vapor deposition (PVD) and sputtering (SPT) are two primary methods used to achieve this. Chemical vapor deposition (CVD) and reactive plasma deposition (RPD) use a vapor transport mechanism but have gaseous or liquid sources containing the desired atomic or molecular species. The gaseous reactants decompose and recombine to form the desired thin film. The decomposition and reaction is assisted by elevated substrate temperature in the case of CVD and by an RF plasma in the case of RPD. The electron beam evaporator can be used to evaporate materials requiring higher temperatures, and currently, this is the only method which can be used in our laboratory.

SiO is a popular material for GaAs optoelectronics device coatings, and an electron beam evaporator has been used to perform the coatings. The evaporation of the AR coating requires high vacuum, usually 4×10^{-7} Torr, and low evaporation rate for obtaining reproducible index of refraction. SiO is a nonconductive material, which makes the power control of electron gun crucial. At low power, the beam cannot vaporize the material, and at high power, may deposit a film with a low index of refraction. The thickness monitoring has to be calibrated for each run.

Figure 4.8 shows the measured reflectivity vs. the wavelength. The measured refractive index is 1.86, and thickness is 1800Å, and the minimum reflectivity is about 0.1 % at 0.86 micrometer. The measured results from each run always have slight differences, and the errors for index of refraction and thickness of the AR coating are under 5%.

However, this task is difficult and these results are not always easy to replicate.

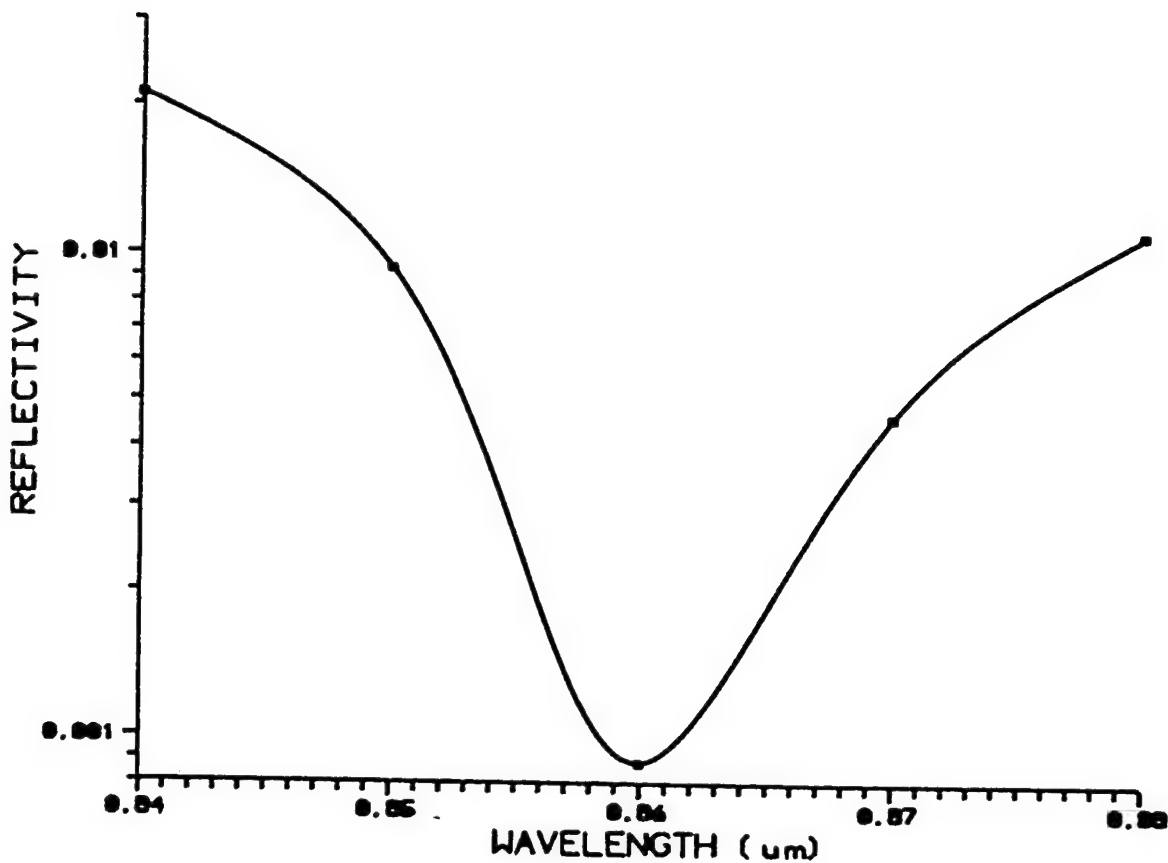


Figure 4.9. Measured reflectivity vs. wavelength.

References

- [4.1] R. N. Hall, G. E. Fenner, J. D. Kingsley, T. J. Soltys, and R. O. Carlson, *Phys. Rev. Lett.* 9, p. 366 (1962).
- [4.2] M. I. Nathan, W. P. Dumke, G. Burns, F. H. Dill, Jr., and G. Lasher, *Appl. Phys. Lett.* 1, p. 62 (1962).
- [4.3] T. M. Quist, R. H. Rediker, R. J. Keyes, W. E. Kray, B. Lax, A. L. McWhorter, and H. J. Zeiger, *Appl. Phys. Lett.* 1, p. 91 (1962).
- [4.4] N. Holonyak, Jr., and S. F. Bevacqua, *Appl. Phys. Lett.* 1, p. 82 (1962).
- [4.5] A. G. Milnes and D. L. Feucht, Heterojunction and metal-semiconductor junctions, New York: Academic Press, 1972.
- [4.6] B. L. Sharma and R. K. Purohit, Semiconductor heterojunctions Oxford: Pergamon, 1974.
- [4.7] V. L. Rideout, *Solid-state Electronics*, 18, p.541 (1975).
- [4.8] B. Schwarzs, ed., Ohmic contacts to semimetals, Electrochem. Soc. New York, 1968.
- [4.9] W. D. Edwards, W. A. Hartman, and A. B. Torrens, *Solid-state Electronics*, 15, p. 387 (1972).
- [4.10] B. L. Sharma, in Semiconductor and semimetals, vol. 15, p.1, 1981.
- [4.11] S. M. Sze, Physics of Semiconductor Devices, chapter 1. John Wiley&Sons, 1984.
- [4.12] C. Dubon-Chevallier, A. M. Chenois, J. F. Bresse, and D. Ankri, Reproducible low-resistivity AuMn ohmic contacts for p-type GaAs, *Electro. Lett.*, vol. 21, p. 614 (1985).
- [4.13] R. E. Williams, Gallium Arsenide Processing Techniques, Artech House, MA, p235, 1984.
- [4.14] F. A. Lowenheim, Electroplating, New York: McGraw-Hill, 1978.
- [4.15] O. S. Heavens, Optical Properties of Thin Solid Films, Butterworth, London, 1955.
- [4.16] H. A. MacLeod, Thin Film Optical Filters, American Elsevier, New York, p. 19, 1969.

CHAPTER 5

MEASUREMENTS

This chapter discusses the tests and measurements on the active optical switches. These tests on the performances of the active optical switches are in two parts: laser characterization, and switch characterization. The first part focuses on characterization of a multiple quantum-well ridge waveguide laser. The lasers are fabricated at the same time and on the same wafer as the active optical switches, and it has same ridge structure as the switches. The results of the laser measurements determine the quality of the wafer, fabrication processing, the parasitics of the devices, the current loading and dynamic response of the switches. The second part characterizes the 1×1 , 1×2 , 2×2 , 1×4 , and 4×4 switches, and the small signal modulation response was also examined on the 1×1 switch.

Section 5.1 presents the laser characterization, which is divided into DC characterization and measurements of small signal modulation response. Section 5.2 presents the switch characterization for 1×1 , 1×2 , 2×2 , 1×4 , and 4×4 switches.

5.1. Laser characterization

5.1.1. DC characterization

DC characterization of semiconductor lasers includes the measurement of the laser light vs. current (L-I curve), and its spectral response.

Semiconductor lasers are extremely easy to damage. An electrostatic discharge will cause the devices to be inoperable, and excessive current drive causes the devices to fuse. Power supplies should be regulated to a limit all time, and current limiting element, a resistor, should be connected in series with the device under test (DUT). The parameter ranges need to be carefully considered before the tests. The variables of the measurements are current, voltage, light output, and device temperature. Since the number of photons emitted depends on the number of electrons injected into the active volume, the current is the independent parameter. The voltage drop across the laser, and light power versus current are very instructive in revealing the characteristics of the lasers. Operating the laser with current pulses less than 1 ms at duty cycles under 1% gives the characteristics of the laser independent of the heat sink properties.

5.1.1.1. Test setup

Figure 1 shows the measurement setup of a laser diode for DC and small signal modulation response. The laser diode under test is a multiple quantum-well single mode ridge waveguide laser, which has a 3 μm wide ridge and 500 μm length cavity (see Figure 2.8 in Chapter 2), and the layer structure was described in Chapter 2 in detail. The laser was attached to an Aluminum (Al) block by silver epoxy, and this Al block was directly attached to a thermoelectric cooler. A thermal compound was used in order to enhance the thermal conductivity between the Al block and the cooler. The diode was directly probed by a high speed probe, which was connected to a bias-T.

DC and RF sources were connected to the laser diode by a bias-T. The light emitted from the diode was collimated and coupled into an optical power meter, and a spectrum analyzer, respectively, by three lenses and a beam splitter. For DC test, only the DC source and optical power meter were used. The RF source and the spectrum analyzer were for the measurements of small signal modulation response. A pellicle was used to split one optical beam into two in the test.

The thickness of the quantum wells and barrier layers are 80 Å and 100 Å, respectively, so that the laser light diffraction is along the transverse direction, with a numerical aperture (NA) of 0.52. The collimating and coupling lens must have similar NA or larger to minimize optical loss.

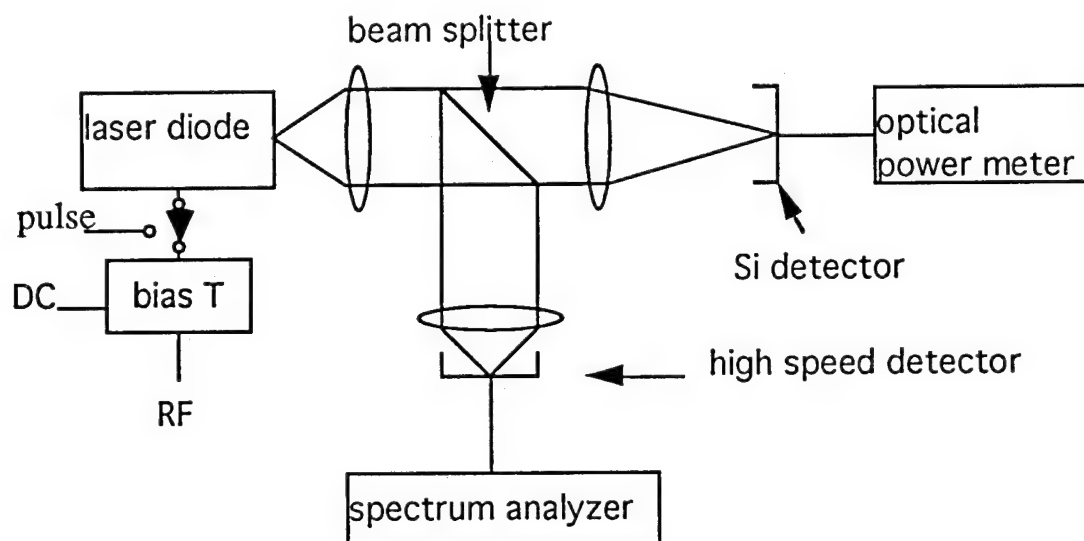
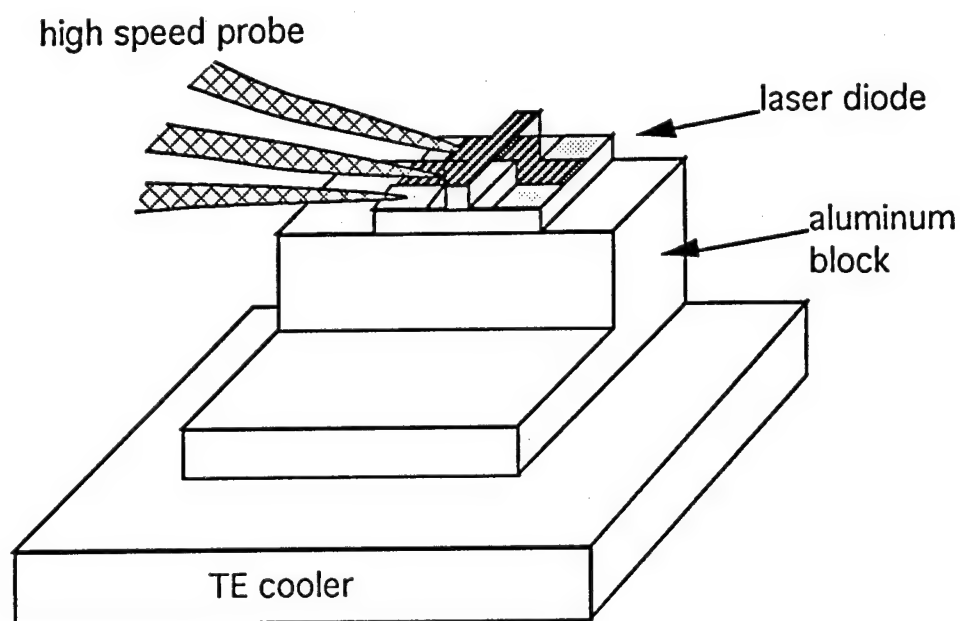


Figure 5.1. Test setup for the ridge waveguide laser diode.

5.1.1.2. I-V characterization

A laser diode is a forward biased p-i-n diode which emits light. Therefore, the I-V characteristics provides an additional source of information for the diode.

An HP4145B semiconductor parameter analyzer was used to measure data. Figure 5.2 shows the measured current through the laser diode versus forward bias voltage across the diode. The turn-on voltage is about 1.4V, which is comparable with $E_g/q = 1.42\text{V}$, and the series resistance was 3.72 ohm.

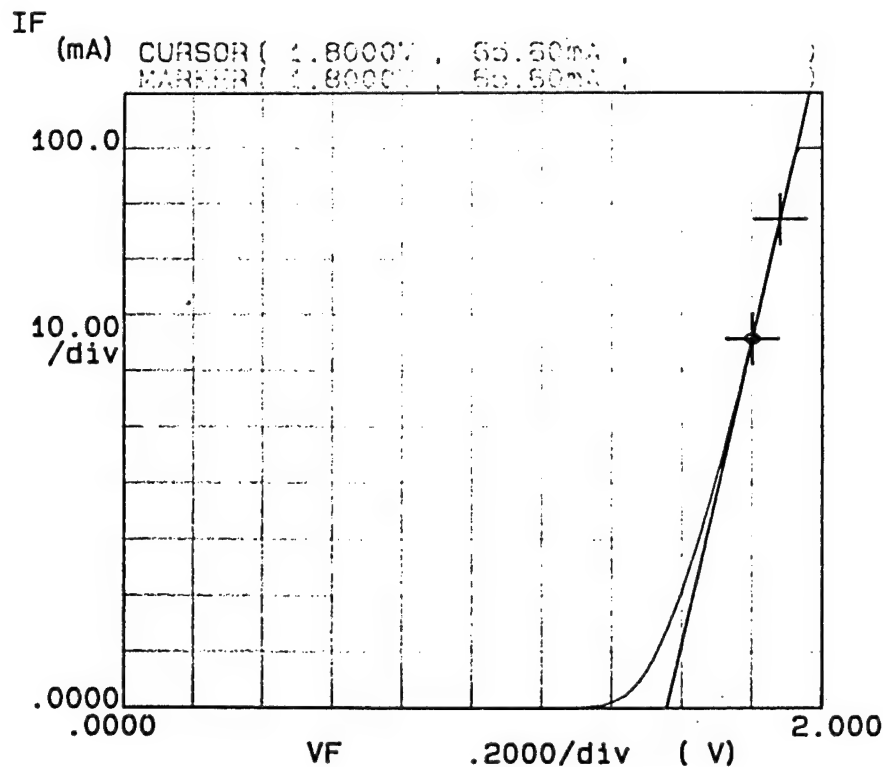


Figure 5.2. Measured current through the ridge waveguide laser diode vs. forward bias voltage across the diode.

When a high reverse bias voltage is applied to a diode, breakdown occurs, and thus breakdown voltage is another parameter used to examine the quality of the diode. Low breakdown voltage implies that there may be a problem in fabrication. High leakage current indicates that the quality of the junction is not good. Figure 5.3 shows the measured current through the laser diode versus reverse bias voltage across the diode. The top curve shows an I-V curve for the diode under reverse bias, and the breakdown voltage is about 5 V because the high doping profile was used in this laser diode, and the corresponding current is in nA range.

The reverse biased laser diode can be used as a photodetector. This is a quite useful function for signal detection in integrated circuits. The set of curves in Figure 5.3 show I-V response to different input optical signals. Light from a similar laser diode, with biasing at $I = 0$, $1.1I_{th}$, $1.15I_{th}$, and $1.2I_{th}$ was coupled into the DUT. The corresponding photo currents of the DUT vary with the input optical signals. When the reverse-bias is less than 4 V, the photo currents increase with the input optical power at each reverse-bias of the DUT, and the each photo current curve from top to bottom is corresponding to the light power of the laser source at $I = 0$, $1.1I_{th}$, $1.15I_{th}$, and $1.2I_{th}$, respectively. Therefore, the reverse-biased laser diode performs as a fairly good photodetector.

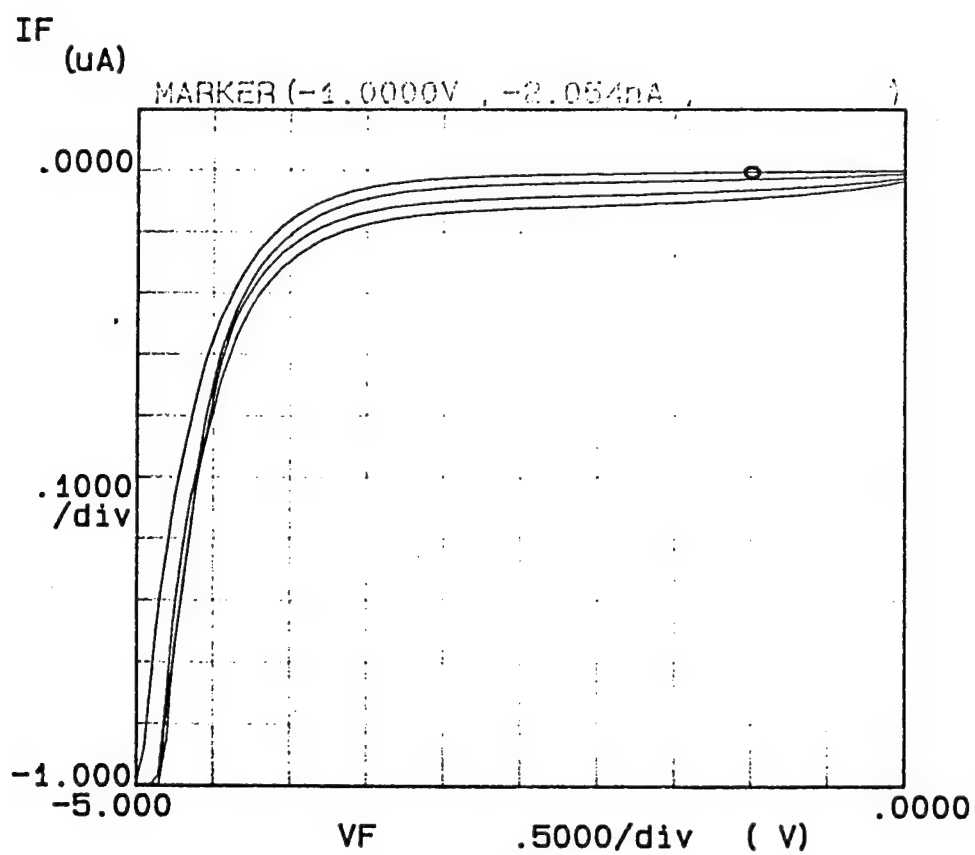


Figure 5.3. Measured currents through the laser diode vs. the reverse bias voltage across the diode.

5.1.1.3. L-I characterization

The light emitted from a laser diode is initially spontaneous emission before the drive current reaches the laser threshold. As drive current increases, the light emitted from the laser diode increases proportionally with current after threshold determined by the quantum efficiency of the device. Light power versus drive current (L-I) characterizes the lasing performance related to the drive current.

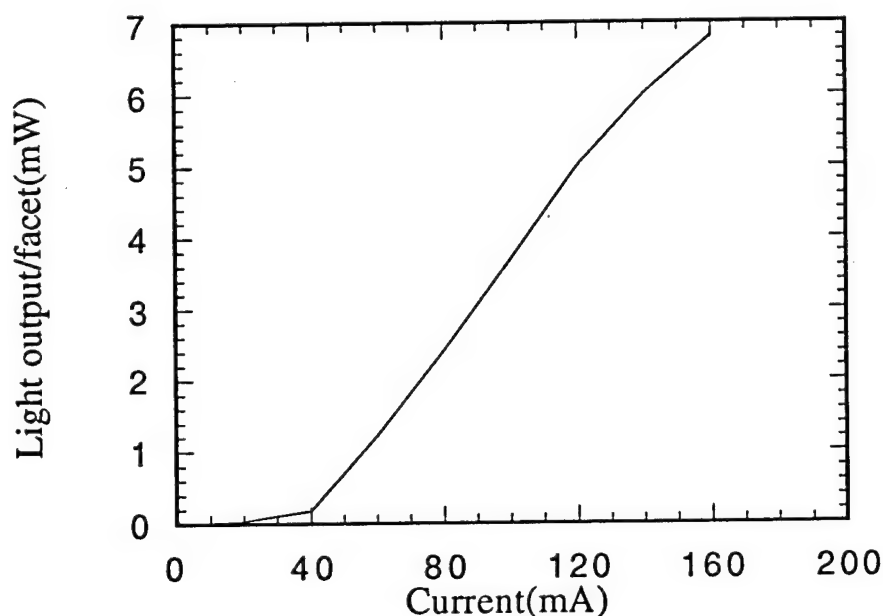


Figure 5.4. Measured light power emitted from the laser diode vs. pulse current through the laser.

For L-I characterization, the measurement was started with pulsed biasing. The laser diode was biased by a pulse generator at 1 ms with 1%

duty cycle, and the current was scanned from 0 to 160 mA. Figure 5.4 shows the measured light power from laser diode versus the drive current through the diode. Initially, the output is spontaneous emission to a threshold current of 45 mA. After threshold, there is a rapid increase in stimulated laser light. The quantum efficiency is about 5%, and the material loss is about 387 cm^{-1} , which is as forty times larger than usual material absorption and results in the high threshold current.

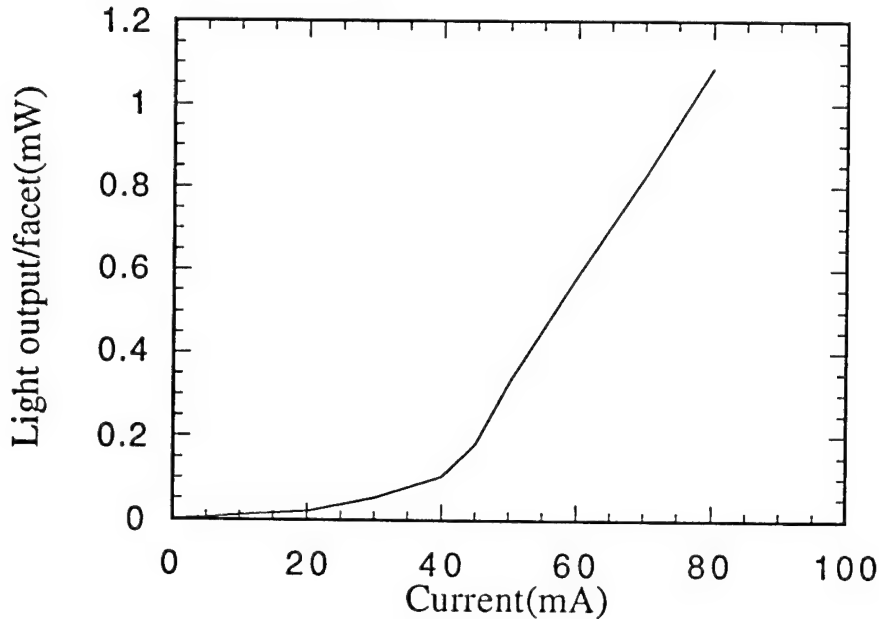


Figure 5.5. Measured light power emitted from the laser diode vs. CW current through laser.

Figure 5.5 shows the CW performance of the same laser diode L-I characteristics. The laser diode was placed on a thermoelectric cooler to maintain the diode at room temperature. The threshold current is about

same as the pulsed case, but the slope of the light versus current curve is not as steep as in the pulsed situation. The turn-on region is much softer than in the pulsed situation due to the heating effect. The quantum efficiency is about 2%, and worse than that under pulsed-bias, because the heating effect under CW operation induced more material absorption [5.1], and also increases the threshold current.

5.1.1.4 Spectrum

The laser diode facets form a Fabry-Perot cavity, and the resonance line spacing corresponds to the cavity modes. Thus, the spectrum close to threshold should be represented by the convolution of the gain bandwidth of the active guide and the cavity filter response function. The laser emission spectrum is the product of the portion of the junction emission peak above threshold times the cavity modulation function.

The output spectrum of the laser was measured by a SPEX 1702/04 Spectrometer. Figure 5.6 shows the spectrum of the ridge laser for different bias currents. Just above threshold ($I = 1.33I_{th}$), most of the longitudinal modes are active, but at high current ($I = 1.8I_{th}$), only a few of them dominate. Although the number of longitudinal modes is reduced under high bias, at least three modes are still present.

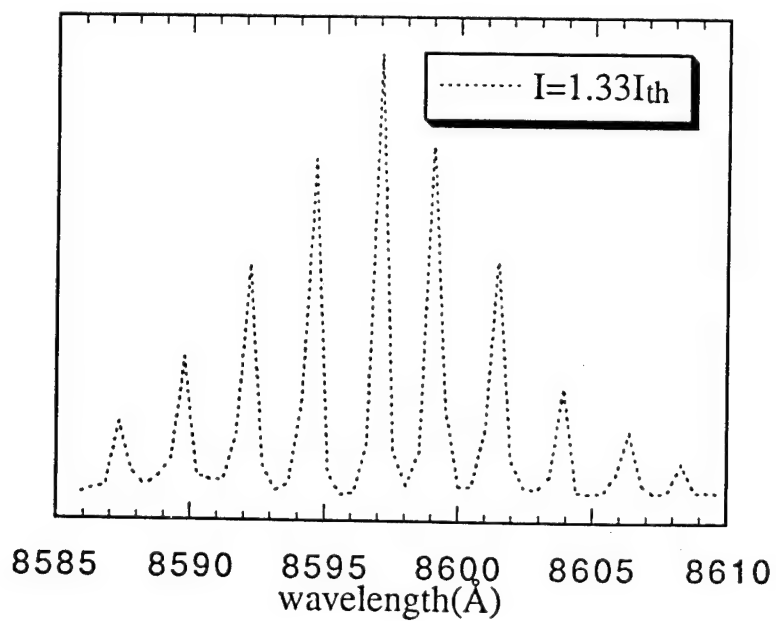
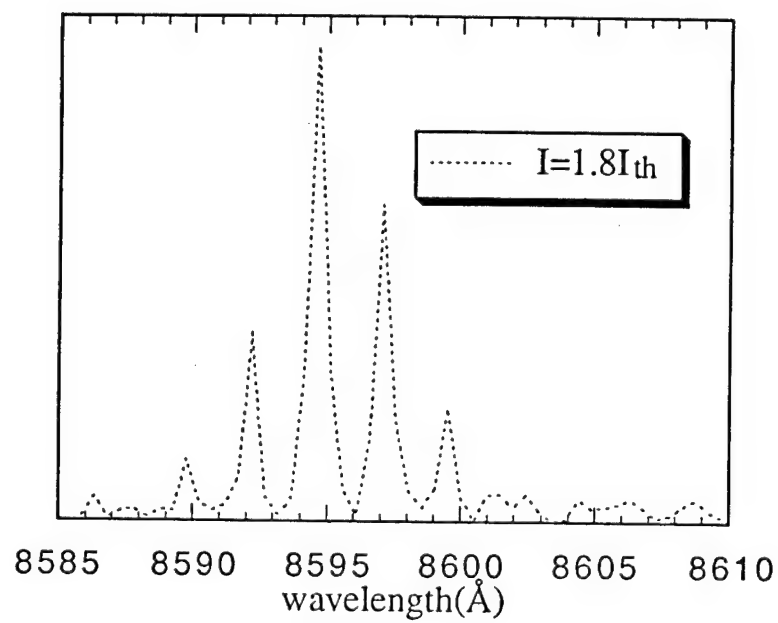


Figure 5.6. Optical spectrum of the ridge laser.

The laser light is emitted from the facets near the active region in a pattern called the laser near field. The near field pattern reveals the distribution of the optical field in the transverse direction across the laser cavity. Figure 5.7 shows the near field of the transverse mode at $I = 1.5I_{th}$, which shows there is only one transverse mode present, which confirms the single mode waveguide design.



Figure 5.7. Near field mode of the laser diode at $I = 1.5I_{th}$.

5.1.2. High frequency measurement

The frequency response characteristics are determined by the natural resonance frequency of the laser and parasitics of the device structure. The resonance frequency can be very high, and usually may not be the fundamental limit of the high frequency response. The major limitation may be from the parasitics of the device structure, and packaging configurations.

We utilized a RF probe of 40A-GSG-150-P (Picoprobe) to measure the frequency response of the laser diode, and this reduced the parasitics associated with the wire bonding. To characterize the parasitics of the laser diode, we use the simplest circuit model necessary to describe the diode. The circuit is composed of an inductance in series with the parallel combination of a resistance and a capacitance (see figure 5.8). This model is valid for weakly guided structures such as ridge waveguide and heteroepitaxial ridge regrown lasers, as well as strongly guided structures that use dielectric layers as the predominant means of current confinement.

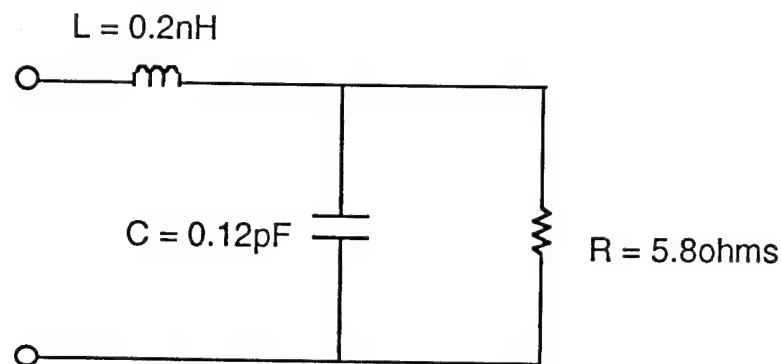


Figure 5.8. Equivalent circuit model for the diode.

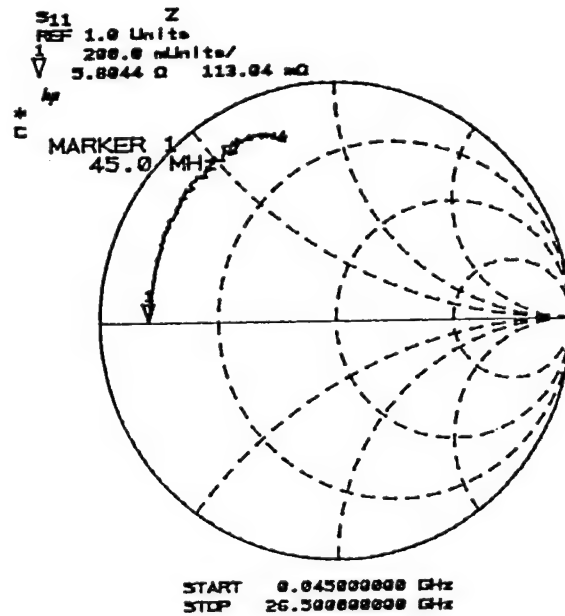


Figure 5.9. Measured S_{11} parameter vs. frequency from 45MHz to 26.5GHz for the laser diode at $I = 1.33I_{th}$.

The simple circuit model with a diode resistance of 5.8 ohms, parallel capacitance of 0.12pF, and series inductance of 0.2nH was derived from the scattering parameters measured using an HP8510A network analyzer. Figure 5.9 shows the measured S_{11} as function of frequency.

The measured S_{11} was used to calculate the small signal response of the laser diode. The response of the laser diode is given by the ratio between output power P_{out} and input power P_{in} . The output power P_{RF} from the RF source is known. Therefore P_{in} can be calculated by

$$P_{in} = (1 - |S_{11}|^2) P_{RF} \quad (15).$$

Then the transfer function for small signal modulation is

$$P_{out}/P_{in} = \frac{P_{out}}{(1 - |S_{11}|^2) P_{RF}} \quad (16).$$

In order to obtain the small signal response, the laser diode was biased above the threshold current and an RF signal was added on the DC bias, as shown in the test setup in Figure 5.1, with the RF signal from an HP8340A Synthesized sweeper. The light output of the laser diode was measured by a high speed PIN photo detector connected to an HP 8593A Spectrum Analyzer. The frequency response of the laser diode at $1.1 I_{th}$, $1.5 I_{th}$ and $1.8 I_{th}$ is presented in Figure 5.10. The relaxation oscillation frequency increased from 16GHz to 19GHz when the biasing current was increased from $1.1 I_{th}$ to $1.8 I_{th}$. After the biasing current reached $1.5 I_{th}$, the relaxation frequency changes slightly, and we suspect this due to poor heat sink. When the heat created by the diode is not removed efficiently, the temperature of the device increases so that the threshold current increases. As we note in the equation (2.16) in Chapter 2, the increasing

the threshold current reduces the relaxation frequency. Therefore, even when the device current increased from $I = 1.5 I_{th}$ to $I = 1.8 I_{th}$, the relaxation frequency had almost no change.

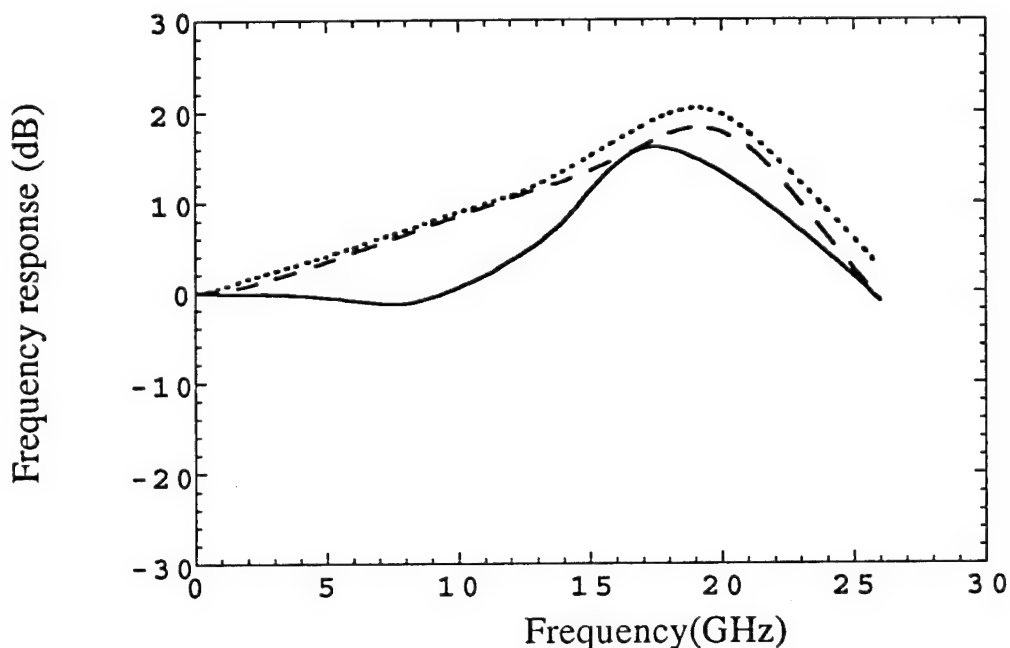


Figure 5.10. Small signal modulation response of the ridge waveguide laser at $1.1 I_{th}$ (solid line), $1.5 I_{th}$ (dash line) and $1.8 I_{th}$ (dotted line).

5.2. Switch Characterization

Switch measurements were made on the 1×1 , 1×2 , 2×2 , 1×4 and 4×4 switches. Figure 5.11 shows the setup for the test. A laser from the

same wafer as the optical switches is used as the light source. The light emitted from the laser is collimated and coupled into a switch with a pair of identical lenses. With bias, the switch emits incoherent spontaneous emission light which is monitored by the left CCD camera for alignment purposes, along with the light of the laser diode reflected by a facet of the switch. The output light from the switch is collimated and sent to a detector and the second CCD camera. This setup was used for all test of our optical switches. The DUT, an active optical switch, is sitting on a TE cooler keeping it at room temperature. Figure 5.12 shows a top view of the 1×1 , 1×2 , 2×2 , 1×4 and 4×4 switches. The 1×4 and 4×4 switches are connected together.

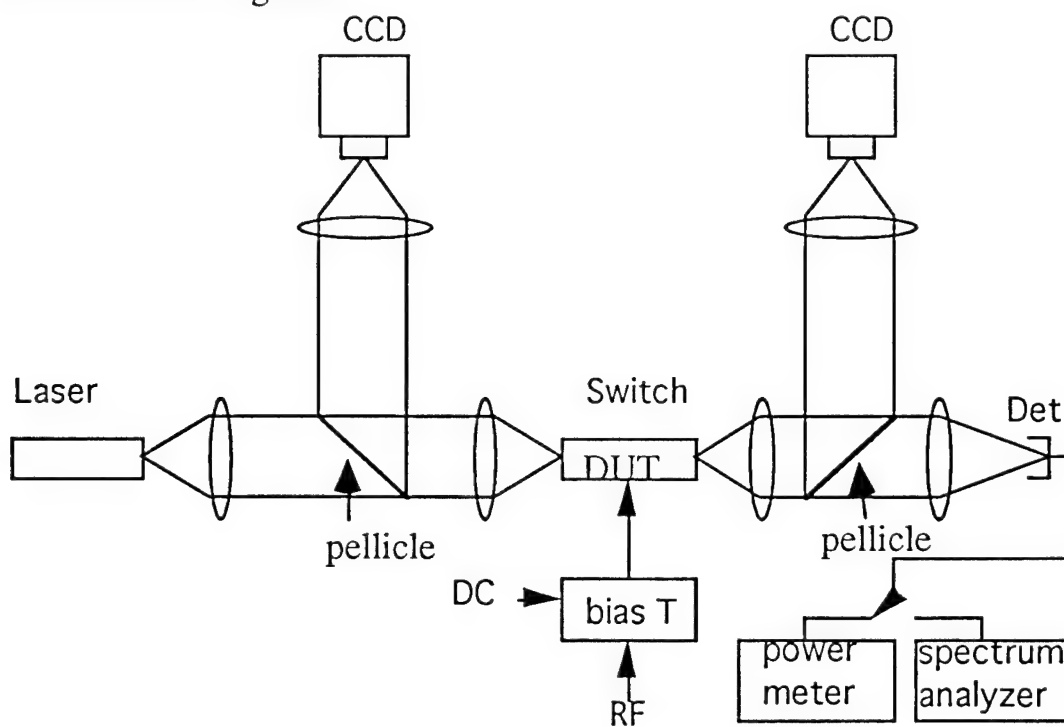
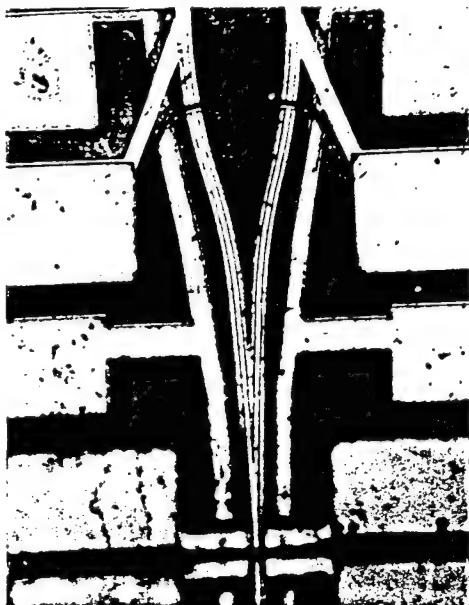
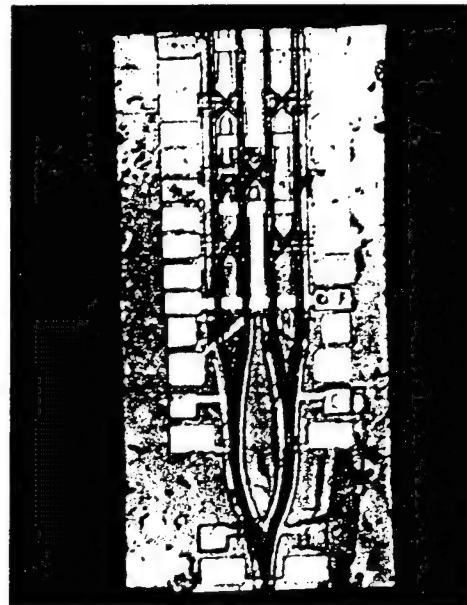


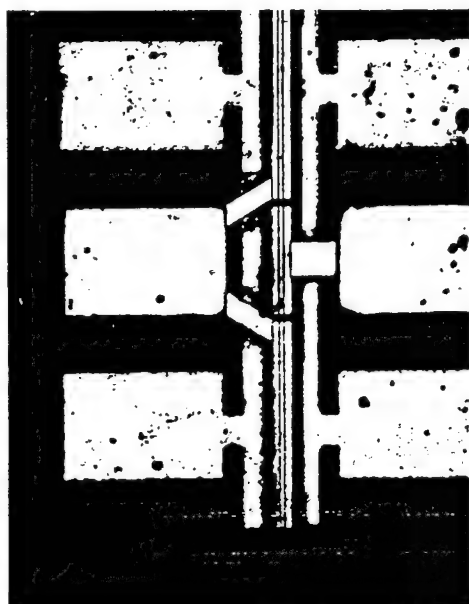
Figure 5.11. Setup of DC and RF characterization for optical switches.



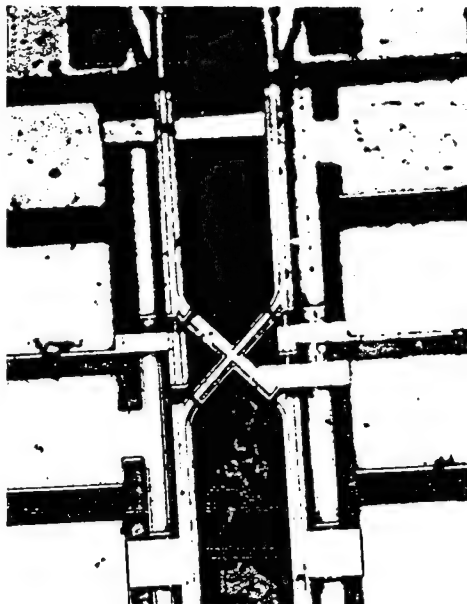
1X2 SWITCH



1X4 and 4X4 SWITCHES



1X1 SWITCH



2X2 SWITCH

Figure 5.12. A top view of 1x1, 1x2, 2x2, 1x4 and 4x4 switches.

5.2.1. 1×1 switch - gate switch/amplifier/modulator

The 1×1 switch is basically a semiconductor optical amplifier with multiple electrodes. It can amplify or attenuate optical signals by controlling the current through the device. This device also can modulate optical signals by modulating the current through the device. It can be used in optical networks for point-to-point gate connection without attenuation, restoring optical signals, or encoding by modulating optical signals.

The 1×1 switch has the 3 micrometer ridge width and 500 micrometer long structure discussed in Chapter 2. The length of the central switch arm is 75 micrometers, and the gap between the switch arm and DC arms is 5 micrometers. Before AR coatings of its facets, the switch behaves as a laser diode, and the threshold current was measured, and found to be the same as the laser diode, with similar structure described in Section 5.1. With AR coatings on both facets of the 1×1 switch, the threshold current for lasing is dramatically increased. Before any test for the gate switch/amplifier/modulator, the device was tested as a laser to find the threshold current. This threshold current revealed the quality of the AR coating and dynamic range of the device operation.

A 1KHz pulse with a 1% duty cycle was used to bias the device to obtain the L-I curve, and the test setup is shown in Figure 5.11. The measured threshold current was about 400% greater than the laser diode without any AR coating. Figure 5.13 shows the measured L-I curve for the switch, note that the threshold current was 180 mA.

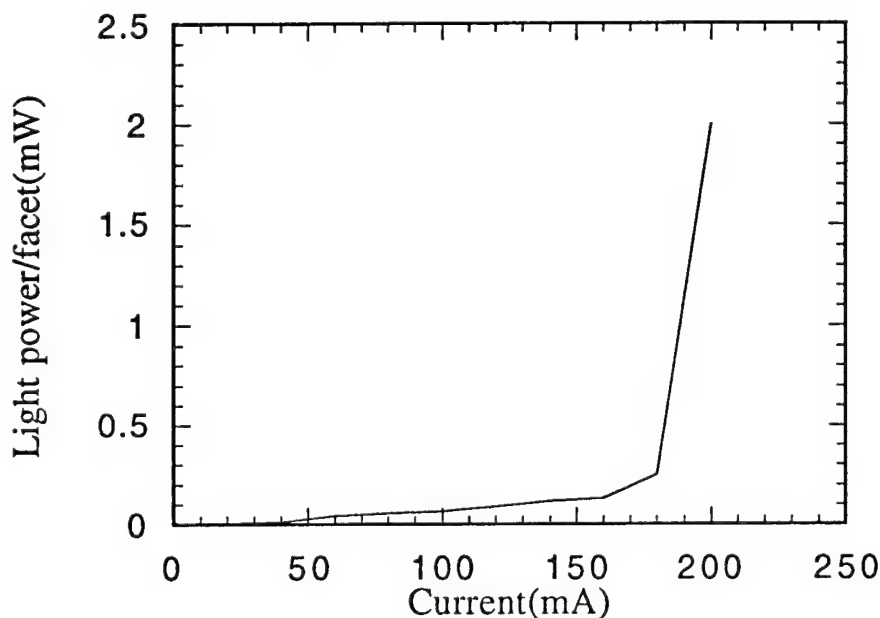


Figure 5.13. Measured light power emitted from the 1×1 switch vs. pulse current at 1KHz with 1% duty cycle through the device.

For the gate switch/amplifier test, the switch was biased from 0 to 150 mA. In order to achieve the largest possible extinction ratio of output power for the device, we biased all the contacts, instead of biasing the only central section (see figure 2.9), and the device was biased through a pair of RF probes. The gain/attenuation characteristics of the switch with CW biasing are shown in Figure 5.14. The gain value includes the insertion loss and the loss from the lenses which is about 10 dB, and the maximum gain including the loss was 10 dB. The lowest attenuation achieved in this test was about -22 dB, which was limited by the dynamic

range of the test setup. The difference between maximum gain and lowest attenuation was about 30 dB.

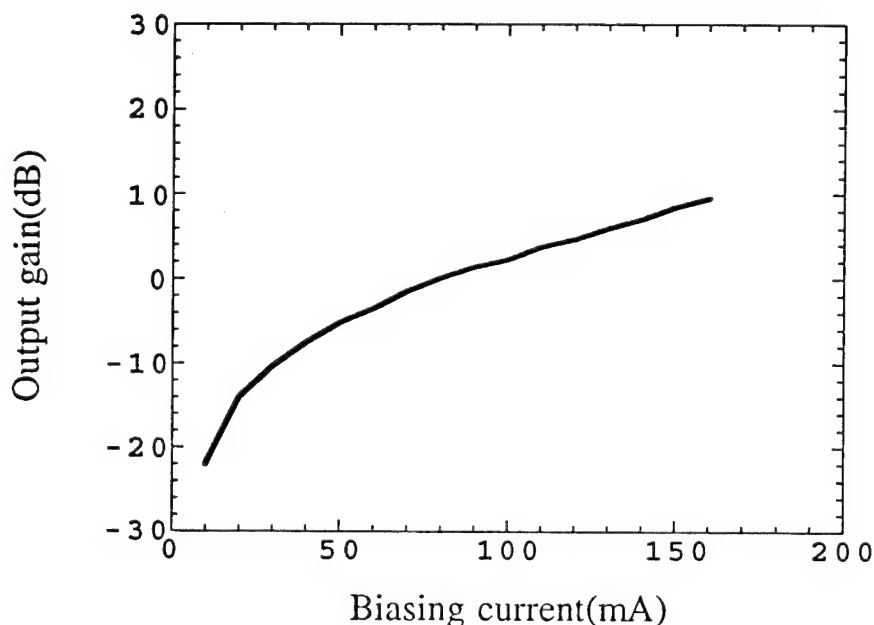


Figure 5.14. Power gain/attenuation as a function of bias current for a 500 micron long 1×1 optical switch/modulator.

For the measurement of the small signal modulation response, the device was biased just above the transparency, and an RF signal from an HP8340A Synthesized sweeper was added to the DC bias through a bias-T for the modulation. The output signal was detected by a high-speed detector, and then sent to an HP8593A Spectrum Analyzer. The S_{11} parameter was measured by an HP8510A, and used to calculate the input power of the device by same method as that used for small signal modulation response of a laser diode in Section 5.1.

The measured frequency response of small signal modulation of the switch is shown in Figure 5.15, and note that the 3dB response was around 19GHz, and the peak frequency of the response is at about 17 GHz, which was slightly less than the laser diode with similar structure shown in Section 5.1.

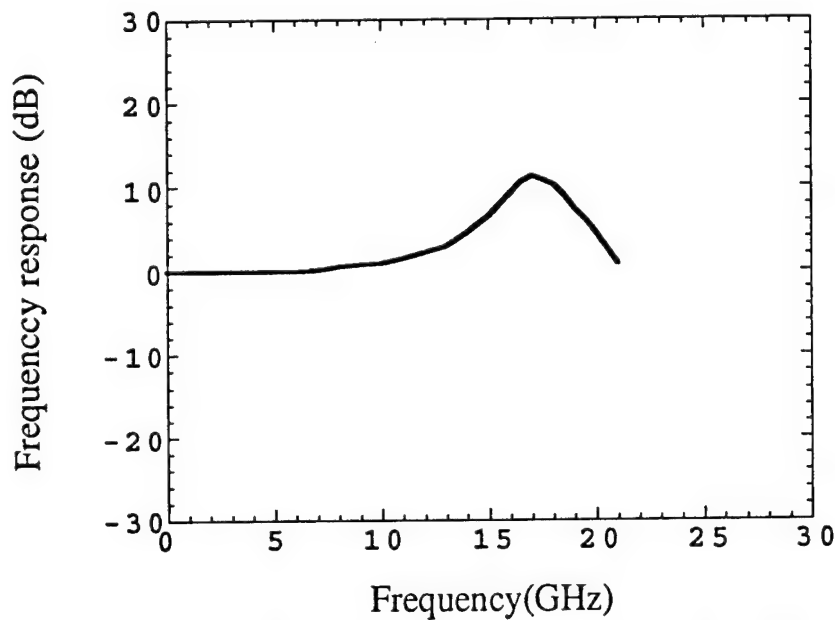


Figure 5.15. Small signal frequency response of a 1×1 switch/modulator biased at 60 mA.

The device was not operated like a semiconductor laser amplifier since the DC bias ($I = 60 \text{ mA}$) was far below the threshold ($I_{th} = 180 \text{ mA}$) for lasing. The AR coating which we used in our switches had a reflectivity of about 0.1%. This reflection reduces the photo life time dramatically, which tends to move the peak frequency higher provided

the I/I_{th} ratio remains the same. But when the photon density in the device increases due to the input signal, the effective threshold current was reduced. Since the rate equations still hold for the laser amplifier, because of stimulated emission, we expect to see a relaxation oscillation gain peak. This is a new result, not discussed elsewhere with literature.

5.2.2. 1×2 switch

The 1×2 switch performs optical signal branching. The device can be operated in either the point-to-point or the broadcast mode. Optical signals from one terminal port can be equally distributed either to one of the two branches or to both branches simultaneously with 0 dB loss or gain. The optical signals from two different branches can be combined together and sent out to a simple port. Therefore, this device performs two-dimensional optical signal splitting or combining.

The 1×2 switch has a 3 micrometer wide ridge, and is 500 micrometer long, and the switch arms are 100 micrometers. The gap between the switch arms and the DC arm is 5 micrometer, and the spacing between the two switch arms is 100 micrometers. This device was tested for 1×2 switching function, and Figure 5.16 shows the diagram of the measurement. The laser diode was biased by a pulse generator at 1KHz with a 1% duty cycle, and the switch was directly probed by RF probes.

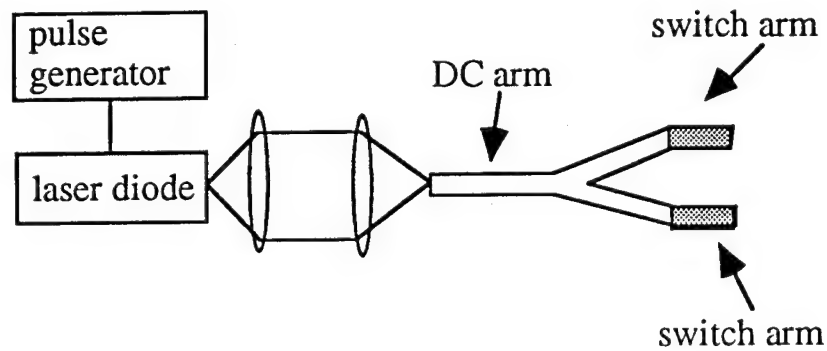


Figure 5.16. Diagram of 1x2 switch test setup.

The switch arms were alternately biased in CW by a current source, and the DC arm was biased in pulse and CW, respectively (see Figure 5.16). Figure 5.17 shows the gain/attenuation characteristics of the switch for pulse bias of the DC arm at 1 KHz with a 10% duty cycle, and two cases were tested with the DC section biased at 100 mA and 120 mA. For each biasing condition of the DC arm, the current through one switch arm was scanned from 0 to 45 mA, and the other one was unbiased. The extinction ratio of the maximum gain and lowest attenuation was 15 dB and 10 dB for $I = 100$ mA and 120 mA, respectively. The maximum gain was increased from 10 dB to 12 dB with the DC section biased from 100 mA to 120 mA. But the extinction ratio was decreased as the current increased.

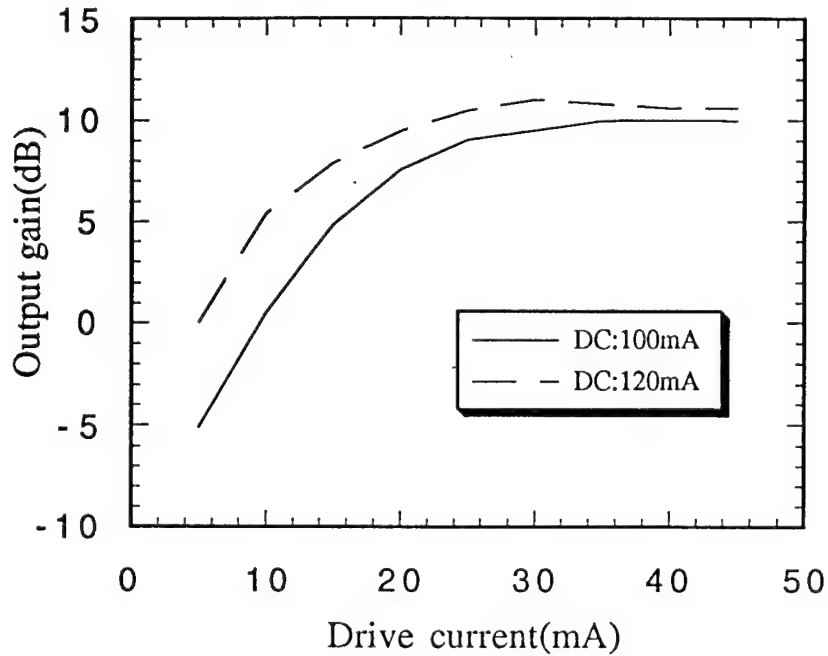


Figure 5.17. Output gain of the 1x2 switch with DC arm pulsed-biased (1KHz and 10% duty cycle) vs. the (CW) current through one of the switch arms. The solid line is for $I = 100$ mA, and dashed line is for $I = 120$ mA.

With a high bias on DC section, this section created more signal gain and emitted more photons into the switch section. Thus, the part of the switch section, which is next to the DC arm, was partially saturated by the photons, and the overall attenuation on the switch arm reduced. Therefore, the corresponding extinction ratio was reduced. For $I_{DC} = 100$ mA, the maximum extinction ratio was achieved.

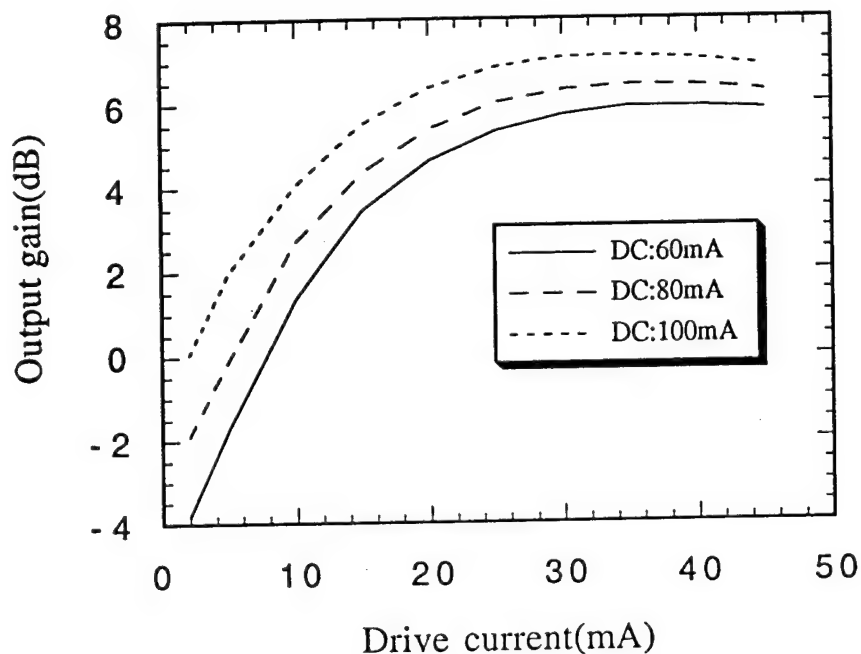


Figure 5.18. Output gain of the 1×2 switch with CW biased DC arm vs. the (CW) current through one of the switch arms. The solid line is for $I = 60$ mA, dashed line is for $I = 80$ mA, and dotted line is for $I = 100$ mA.

Figure 5.18 shows the output gain characteristics for the switch with a CW bias of the DC arm. Similar to the above measurement, one of the switch arms was biased from 0 to 45 mA, and the other was unbiased. The DC section was biased at $I = 60$ mA, 80 mA, and 100 mA, respectively. The maximum output gain was increased from 5.9 dB to 7.12 dB and the extinction ratio was decreased from 10.5 dB to 7 dB when the biasing current of the DC section was increased from 60 mA to 100 mA.

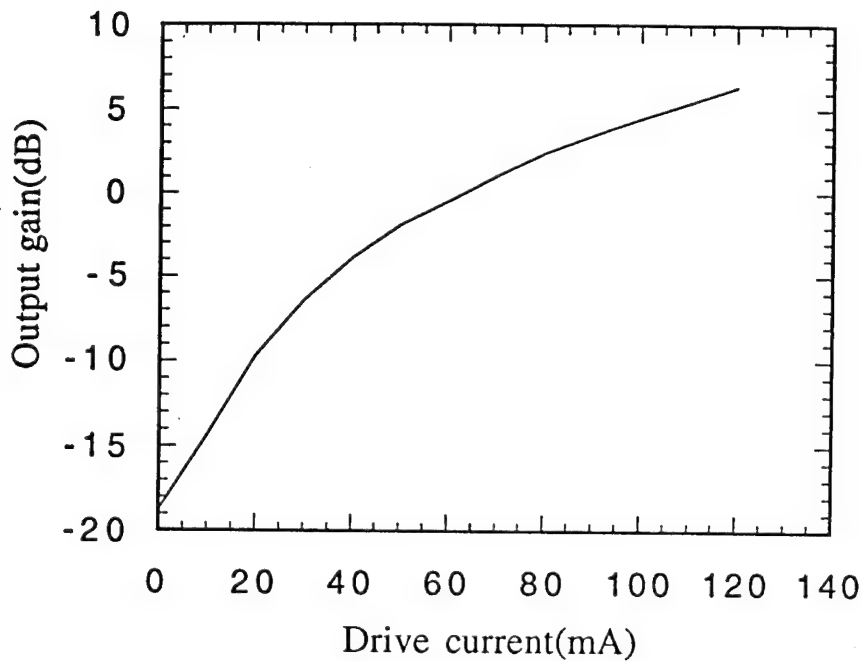


Figure 5.19. Output gain of the 1×2 switch vs. the current through one of the switch arms and DC arm simultaneously.

The final measurement of the 1×2 switch was to obtain the maximum extinction ratio between the maximum gain and lowest attenuation. The DC arm was connected with one of the switch arms. They were biased together for the measurement. Figure 5.19 shows the measured result for gain/attenuation of the switch with CW bias. The extinction ratio was about 27 dB, which was close to the result for the 1×1 switch. Since there were curved waveguides in this switch, more photons were scattered out from these sections of the waveguide than the straight parts. Therefore, the gain per unit area in a 1×2 switch (5.6 dB/100 μm) was not as large as the one in a 1×1 switch (6 dB/100 μm).

Figure 5.20 shows the top view of the switch for two test cases. The first was with the DC arm biased and both switch arms unbiased. The emitted light was from spontaneous emission. The second was with the DC arm biased and one of the two switch arms biased, and the other was unbiased.



Figure 5.20. Top view of the 1×2 switch with biased DC arm and biased/unbiased one of the switch arms.

Figure 5.21 shows the end view of output guides of the switch with biased DC arm (pulsed 100 mA) for three different biasing conditions of the switch arms. The top one shows that the left switch was on ($I = 40$ mA) and the right one was off. The power output ratio between them was 15 dB. The middle one shows both switch arms were off. The low one shows the left switch arm was off and right was on ($I = 40$ mA). The corresponding ratio between output power was the same as the opposite situation above.



Figure 5.21. The end view from output guides of the 1×2 switch with DC arm biased at 100 mA pulsed and 40 mA biased/unbiased switch arms.

5.2.3. 2×2 switch

The 2×2 switch is an optical crossbar switch structure. Point-to-point or broadcast operation may be performed by this device. It can simultaneously connect two input optical signals to any combinations of two outputs with 0 dB loss or gain. Any $n \times m$ optical switch array may be built using a suitable number of 2×2 switches. This device can be used to form reconfigurable multiple-dimensional switch network in local area and long distance optical networks.

The 2×2 switch has the same ridge guide structure, discussed earlier, with two 3 micrometer wide ridge and is 500 micrometer long, and the two parallel waveguides are 100 micrometers apart. The length of the switch arms is 75 micrometers, and the gap between the switch arms and DC arms is 5 micrometers.

The routing of optical signals of the 2×2 crossbar switch was tested. The laser light source was pulsed at 1kHz with a 1% duty cycle, and the light was coupled into a 1×2 switch, and the two output signals from this were coupled into the two parallel waveguides of the 2×2 switch. The parallel through and crossed routing performance of the switch were measured for different biasing conditions.

Figure 5.22 shows a packaged 2×2 switch with a 1×2 switch together. This package allowed us only to measure the relative output power from the switch due to our inability to collect all the output light from the output guides of the 2×2 switch, because of the packaging constraints. Figure 5.23 shows a diagram of the measurements, and as in

the previous tests, the DC arms were pulse-biased at 1KHz with a 10% duty cycle, and the switch arms were biased at CW.



Figure 5.22. A packaged 2×2 switch with a 1×2 switch together.

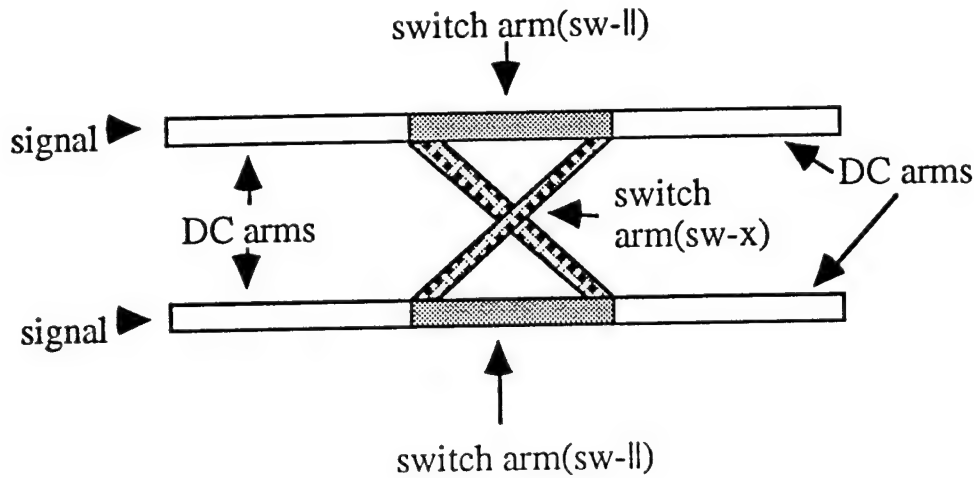


Figure 5.23. Measurement diagram for 2×2 switches.

Figure 5.24 shows the measured results of the switch with CW biasing of the switch arms. The switch arms, sw-ll and sw-x, (see Figure 5.23) were biased sequentially by a current source. The solid lines and dashed lines were for DC section bias at $I = 100$ mA and 150 mA, respectively. The output power for the 'on' state of sw-ll was about 2 dB larger than the that of the "on" state for sw-x, because of the bifurcation loss at the waveguide junctions at 'x' regions, for each bias of DC section. With increase of pulse amplitude for the DC arms from 100 mA to 150 mA, the difference between sw-ll and sw-x was decreased, and the extinction ratio of output power was increased. For the parallel arms, the extinction ratio increased slightly. But for the cross arms, the extinction ratio increased more, since the longer arms and bending loss make these sections less easy to saturate, than the parallel arms.

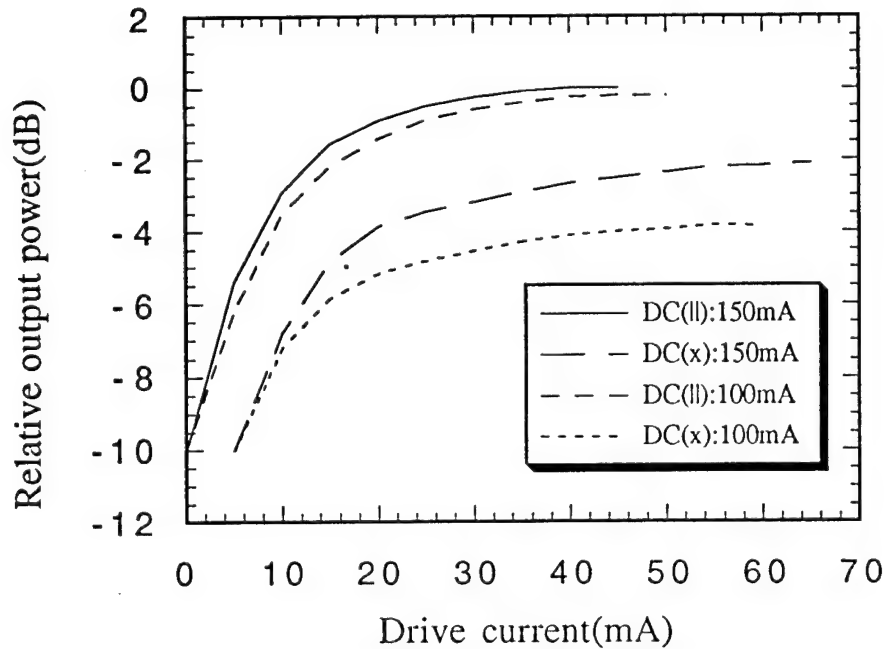


Figure 5.24. Relative output power vs. current through the switch arms of parallel section and cross section, respectively, for DC arms biased at $I = 100$ mA and 150 mA. The top two curves are for parallel switch arms, and low two are for cross switch arms.

Figure 5.25 shows the top view of the 2×2 switch for two different conditions. The first one is with the switch biased for the cross routing condition. The input optical signals were coupled into the two waveguides in the DC sections, and with biasing on the 'x' shape section, the two signals were cross routined. The second picture was with the 'x' section in the off-state, and one of the parallel section was in the on-state.

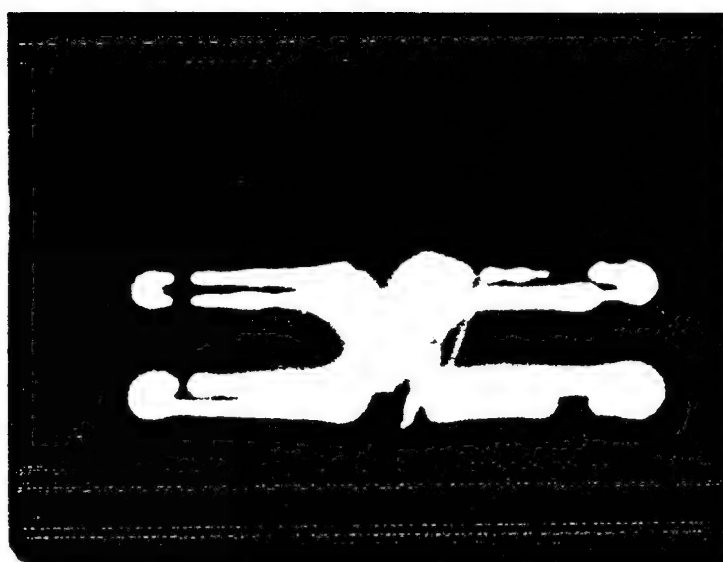
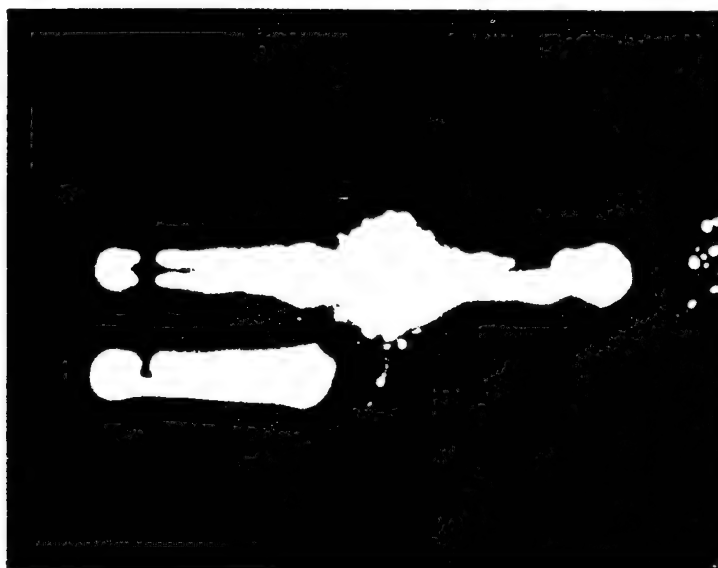


Figure 5.25. Top view of a 2×2 switch for parallel through and exchange routine switching.

5.2.4. 1×4 and 4×4 switches

The 1×4 switch acts as a 1×4 splitter for optical signals, with 0 dB loss or gain, formed by three 1×2 switches. It links one port to any combination of four ports. The 4×4 switch is a switch matrix structure formed by five 2×2 crossbar switches. It simultaneously links any combination of four input/output ports, on one side input, to any combination of ports, on other outputs. The 1×4 switch is used in our case, for signal distribution in the 4×4 test. These 1×4 and 4×4 switch structures may be used to form reconfigurable optical networks.

The 1×4 switch has the same structure discussed earlier, the 3 micrometer wide ridges and is 1mm long. the spacing between any two adjacent waveguides is 100 micrometers. Similarly, the 4×4 also has 3 micrometer wide ridges, and is also 1 mm long, and here also the waveguides are 100 micrometers apart, and all of the gaps between the switch arms and DC arms are 5 micrometers long in both structures. The test diagram of these discuss is shown in Figure 5.26. The signal was coupled into a 4×4 switch through a 1×4 switch, then was consecutively switched into the four output guides. All of the DC arms and switch arms were pulse-biased at 1KHz with a 1% duty cycle. Figure 5.27 shows a photograph of packaged 4×4 switch with a 1×4 switch together. This package has sixteen leads so that only a limited sets of functions can be tested. The device package in front the output terminals of the 4×4 switch does not allow full access to the guide output, and therefore the measurement is relative power. The most serious problem with the

package was inefficient heat dissipation so that the devices could not be operated properly. Even with TE cooler underneath the package, the devices still could not survive our tests. We are currently working on the packaging these devices for better thermal dissipation. Here, we only show a few pictures that were taken during the test, before failure.

Figure 5.28 shows the bonded 1×4 and 4×4 switches. Each one of them is 1 mm long, and 0.5 mm width. Figure 5.29 shows a top view of the 1×4 switch with pulsed bias at 1KHz, with a 1% duty cycle. The income signal was coupled into the input terminal of the 1×4 switch, and sent to four other waveguides connected to the 4×4 switch. Note that the light was observed from the top of the chip was spontaneous emission from the device. Figure 5.30 shows a cross switching case of the 4×4 switch. With a pulse bias at 1KHz with a 1% duty cycle, the signal was switched from low at waveguide up to the top most waveguide. As before, the light seen was spontaneous emission from the guides.

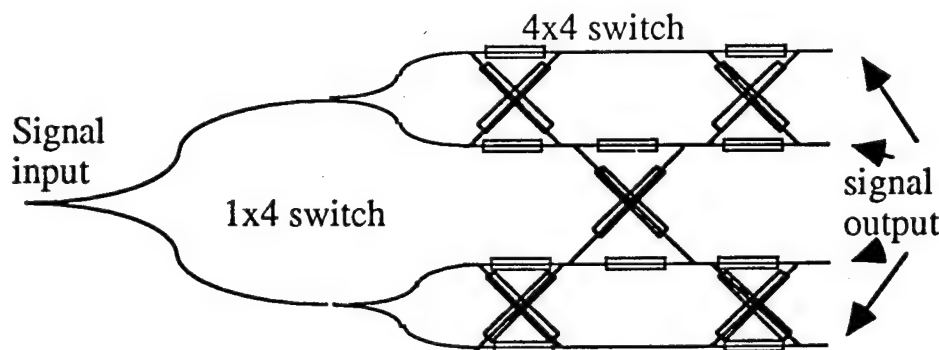


Figure 5.26. Diagram of signal distribution for the test of 1×4 and 4×4 switches.



Figure 5.27. Packaged 1×4 and 4×4 switches.

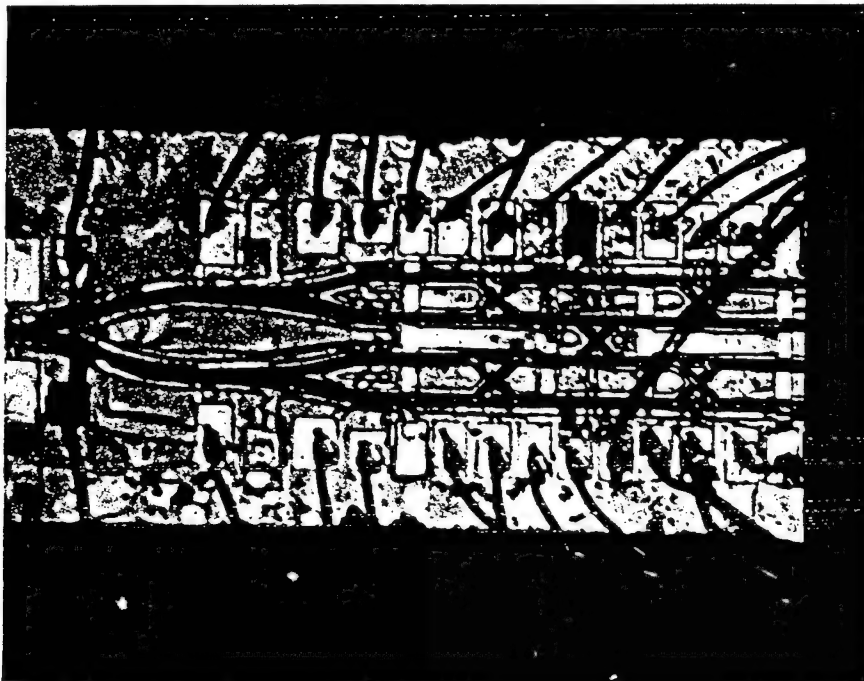


Figure 5.28. Wire bonded 1×4 and 4×4 switches.

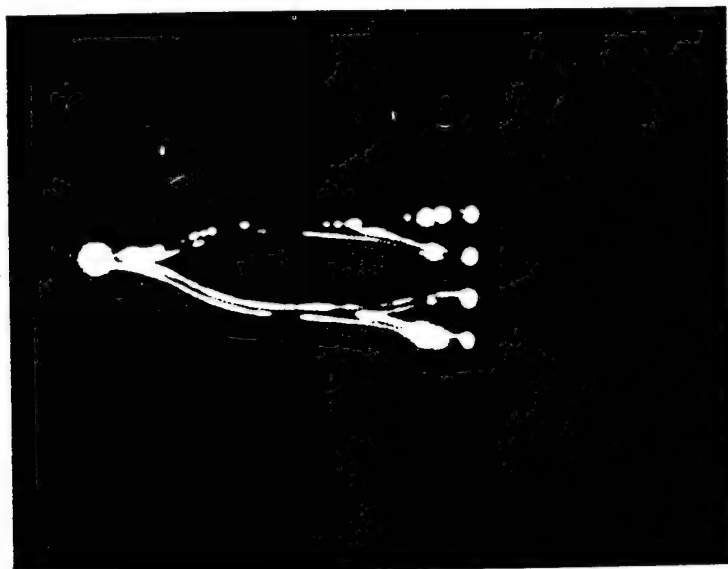


Figure 5.29. Top view of the 1x4 switch with a proper bias.



Figure 5.30. Top view of the 4x4 switch with a proper bias.

REFERENCES:

- [5.1] G. H. B. Thompson, Physics of Semiconductor Laser Devices, Wiley, New York, 1980.

CHAPTER 6

CONCLUSION AND SUGGESTIONS FOR FURTHER STUDIES

The active optical switches based on a multiple quantum well single mode ridge waveguide semiconductor optical amplifier have been investigated in this report for the feasibility of photonic switches. The 1×1 (gate switch/amplifier/modulator), 1×2 (bifurcation switch), 2×2 (photonic crossbar), 1×4 (four-way power splitter), and 4×4 (reconfigurable switch matrix) active optical switches have been designed, fabricated, and tested.

In Chapter 2, we presented the principles of our active optical switches and switch design, respectively. A set of rate equations has been used to characterize the small signal modulation response of a single mode ridge waveguide laser, and the derivation revealed the parameters which determine the bandwidth of the modulation response. We also presented a simple model for the gain recovery dynamics of semiconductor laser amplifiers, and showed that the separate-confinement barriers act as a reservoir to rapidly replenish the carriers into the quantum wells during the gain recovery process. A new model which may describe the two different types of dynamics is needed. We have designed a separate-confinement multiple quantum well structure and a single mode ridge waveguide structure for the active optical

switches. The length of the switch arms in our switches was 50 μm , 75 μm , and 100 μm , respectively, and have not been optimized with performance of the active switches. Based on our test results, the length of the switch arms needs to be increased for the enhancement of the switch extinction ratio.

The integrated finite-difference method for the analysis and design of a dielectric waveguide has been developed, and presented in Chapter 3. Combined with the Arnoldi method, this numerical technique efficiently and reliably performs the analysis and design of the single mode ridge waveguide. In our waveguide design, we assumed that the waveguide is a dielectric waveguide at transparency, with no attenuation or gain to optical signals. This numerical technique needs to be further developed for handling complex value calculations so that the gain/attenuation cases for the waveguide can be analyzed and designed.

The fabrication of our active optical switches was carried out in Microelectronics Laboratory for Research and Education (MLRE), University of Minnesota. The processing for the switches requires nine masks and eleven principle processing steps without accounting for the cleaving and packaging steps. Mn/Au was used for the p-type ohmic contacts which is not the best type of p-type ohmic contact for the active optical switches, but the best type which we were able to make at the time of the fabrication in MLRE. Further improvements for p-type ohmic contact are available, and these alternative choices for p-type ohmic contacts, for example Au-Zn, should be investigated. The ridge etching was carried out by reactive ion etching using BCl_3 , and the etching rate

and etching quality are reproducible. However, the etching chamber was easily contaminated after two or three sequential etching runs, so that the chamber had to be cleaned by Ar gas mixed with Cl_2 . This dry etching technique needs further development for efficient processing. The gold plating of the airbridged interconnects plays a critical role, and remains a difficult processing step. An alternative choice for the interconnects is using polyimide supported bridges for the interconnects.

Our active optical switches have been characterized for proper switching function. The extinction ratio of the 1×1 switch is about 30 dB, making a practically device for use in the optical networks. The small signal modulation response of the 1×1 switches demonstrates that the active switches with proper device design can be operated at very high frequencies and further study of this response for a broad parameter range is needed. For the 1×2 switches, the signal splitting was tested for zero loss and gain, but the test for combining optical signals has not been carried out. We have characterized the 2×2 switch as a crossbar switch, and 2 dB difference between parallel through and cross routing was obtained. But only relative output power from the switch has been characterized due to the packaging problems. Due to thermal dissipation problems with the current package, the test for the 1×4 and 4×4 switches has not been completed.

The characterization of the active optical switches have been performed using only one optical signal source. The characterization of the switches using variable light frequency and different polarization should be investigated. The noise characterization and the temperature

dependence of the switches should be measured after resolving the packaging problem. The packaging of the active optical switches is a major problem to be resolved in carrying out further characterization of these switches. A package with efficient heat dissipation, simpler mounting process, and easy optical alignment needs to be developed. All of the active optical switches were tested on an optical test table, and since the sizes of the devices were small, the optical alignment was very difficult and sensitive. During the measurement, the switches were tightly surrounded by collimating/coupling lenses and electrical connections. A package with optical fiber connections is highly desirable.

The wafers for the active optical switches were grown by a MBE in MLRE. The quality of the wafers determined the switch performance. Currently, we have fabricated working devices from these wafers, but the material loss was high, about forty times larger than we expected. The photoluminescence tests were never carried out on these wafers. The optimization of growth condition in the MBE for the layer structure of the switches should be carried out.

The semiconductor materials used for the active switches were $\text{Al}_x\text{Ga}_{1-x}\text{As}$ ($x=0, 0.2, 0.45$). The switches which we designed and fabricated are suitable for optical communications systems in local area networks. The principle and design of the switches is transferable to a wavelength of $1.3\text{ }\mu\text{m}$ using the proper materials, suitable for long distance optical communications systems.

Our investigations in this report show that the active optical switches are promising devices for high-speed photonic switching systems in all-optical networks, and we have proved their feasibility. The switches, we designed, fabricated, and tested are basic elements for photonic switching networks, and may form any complicated switching system by a proper combination. Further studies on these switches are needed to enable them to be used in communications systems.

CHAPTER 7

PERSONNEL and PUBLICATIONS

This section lists the personnel supported by this project, some in part, and the publications that have resulted from the project.

7.1 Personnel

The following were involved with the project, some full time, and others part time:

Principal Investigator: Anand Gopinath

Research Assistants/Graduate Students

Zine-Eddine Abid (part-time)
Haozhe Dong
W. Freking (part-time)
R. Freking (part-time)
Klein Johnson (part-time)
M. Nisa Khan (part-time)
Sangin Kim (part-time)
Barry Koch (part-time)
Wei Yang
Mark Yu (part-time)

7.2 Publications in Journal and Refereed Conference Proceedings

1. M. Nisa Khan, A. Gopinath, Investigation of single-mode structures in heterostructure ALGaAs/GaAs ridge waveguides, Integrated Photonics Research Meeting, March 1993, Palm Springs, CA, paper IMB13, pp 51-55, 1993..

2. Z. Abid, K. L. Johnson, A. Gopinath, Vector finite element modeling of dielectric guides by transverse magnetic field formulation, Integrated Photonics Research Meeting, March 1993, Palm Springs, CA, paper ITuC1, pp 220-224, 1993.
3. H. Dong, A. Chronopoulos, A. Gopinath, Vectorial integrated finite-difference analysis of dielectric waveguides, Integrated Photonics Research Meeting, March 1993, Palm Springs, CA, paper ITuC2, pp. 225-228, 1993.
4. Klein L. Johnson, A. Gopinath, Non-uniform finite difference analysis of quantum layer dielectric ridge waveguide structures, Integrated Photonics Research Meeting, March 1993, Palm Springs, CA, paper ITuC4, pp. 233-237, 1993.
5. M. Nisa Khan, W. Yang, A. Gopinath, Directional coupler electro-optic modulator in AlGaAs/GaAs with low voltage-length product, Integrated Photonics Research Meeting, March 1993, Palm Springs, CA, paper ITuA5, pp 184-187, 1993.
6. Mark Yu, A. Gopinath, Velocity-matched resonant slow-wave structure for optical modulator, Integrated Photonics Research Meeting, March 1993, Palm Springs, CA, paper ITuH7, pp. 365-369, 1993.
7. Wei Yang, A. Gopinath, Time-domain simulation of ultrashort pulse process in semiconductor lasers, Integrated Photonics Research Meeting, March 1993, Palm Springs, CA, paper IWE3, pp. 503-505, 1993.
8. M. Khan, A. Gopinath, J. Bristow, J. P. Donnelly, Technique for velocity- matched traveling-wave electrooptic modulator in AlGaAs/GaAs, IEEE Trans. Microwave Theory and Tech., Vol. MTT-41, pp.244-249, 1993.
9. M. Nisa Khan, Wei Yang, Anand Gopinath, Directional coupler electrooptic modulator in AlGaAs/GaAs with low voltage-length product, Appl. Phy. Lett., Vol 62, pp.2033-2035, 1993.

- 10.. Z. Abid, K. L. Johnson, A. Gopinath, Analysis of dielectric guides by vector transverse magnetic field finite elements, J. Lightwave Technol., Vol. 11, pp. 1545-1549, 1993.
11. H. Dong, A. Chronopoulos, J. Zou, A. Gopinath, Vectorial integrated finite-difference analysis of dielectric waveguides, J. Lightwave Technol., Vol. 11, pp. 1559-1563, 1993.
12. W. Yang, A. Gopinath, Study of mode-locking of semiconductor lasers using time-domain modeling, Appl. Phys. Lett., Vol. 63, pp. 2717-2719, Nov 15, 1993.
13. Mark Yu, A. Gopinath, A new resonant slow-wave electrode design for optical modulators, 1993 Int. Microwave Symposium, June 1993, Atlanta, GA, paper OF1-07, 1993.
14. A. Gopinath, M. Silveira, Vector finite element analysis of optical guides with transverse magnetic fields, Invited talk, 1994 Integrated Photonics Research Meeting Technical Digest, pp 214-215, paper FD1, OSA, 17-19 February 1994, San Francisco, CA.
15. B. Koch, K. Johnson, H-Z Dong, Anand Gopinath, Investigation of single mode geometries for GaAs/AlGaAs planar ridge waveguides, 1994 Integrated Photonics Research Meeting Technical Digest, pp 99-101, paper ThF8, OSA, 17-19 February 1994, San Francisco, CA.
16. W. Freking, W. Yang, A. Gopinath, Study of the stability of passive mode-locked lasers using numerical simulation, 1994 Integrated Photonics Research Meeting Technical Digest, pp 360-361, paper SaD6, OSA, February 17-19, 1994, San Francisco, CA.
17. H. Dong, A. Gopinath, AlGaAs/GaAs Active Optical ridge waveguide switch/modulator on a semi-insulating substrate, 1994 Integrated Photonics Research Meeting Technical Digest, paper PD4, OSA, February 17-19, 1994, San Francisco, CA.

18. H. Dong, A. Gopinath, AlGaAs/GaAs laser on a semi-insulating substrate with airbridges contacts, with 21 GHz modulation response, 1994 International Microwave Symposium, San Diego, CA, May 23-27, 1994.
19. W. Freking, W. Yang, A. Ghiasi, A. gopinath, External cavity semiconductor laser for modulation beyond its relaxation oscillation frequency, 1994 International Microwave Symposium, San Diego, CA, May 23-27, 1994.
20. H. Dong, A. Gopinath, AlGaAs/GaAs active waveguide switches, 1994 Device Research Conference, paper II-A, Boulder, CO, June 1994.
21. A. Gopinath, Finite elemnt and rate equation modeling of semiconductor lasers, Invited Paper, 1994 OSA Annual Meeting, Dallas, TX, October 1994.
22. K. L. Johnson, A. Gopinath, Non-uniform implementation of Stern's semi-vectorial finite difference method for dielectric waveguide structures, J. Lightwave Technol., Vol. 12, 1995, to be published.
23. M. Silveira, A. Gopinath, Analysis of dielectric guides by transverse magnetic field finite element penalty method, J. Lightwave Technology, to be published.

DISTRIBUTION LIST

addresses	number of copies
RL/EROC DR. RICHARD SOREF 80 SCOTT DRIVE HANSCOM AFB, MA 01731-2909	10
ATTN: H. DONG, A. GOPINATH UNIVERSITY OF MINNESOTA 200 UNION ST., SE MINNEAPOLIS, MN 55455	5
RL/SUL TECHNICAL LIBRARY 26 ELECTRONIC PKY GRIFFISS AFB NY 13441-4514	1
ADMINISTRATOR DEFENSE TECHNICAL INFO CENTER DTIC-FDAC CAMERON STATION BUILDING 5 ALEXANDRIA VA 22304-6145	2
ADVANCED RESEARCH PROJECTS AGENCY 3701 NORTH FAIRFAX DRIVE ARLINGTON VA 22203-1714	1
NAVAL WARFARE ASSESSMENT CENTER SIDEP OPERATIONS CENTER/CODE QA-50 ATTN: E RICHARDS CORONA CA 91718-5000	1
AFIT/LDEE 2950 P STREET WRIGHT-PATTERSON AFB OH 45433-6577	1

WRIGHT LABORATORY/MLPD ATTN: D.L. DENISON WRIGHT-PATTERSON AFB OH 45433-6533	1
WRIGHT LABORATORY/MTEL WRIGHT-PATTERSON AFB OH 45433	1
AUL/LSE BLOG 1405 MAXWELL AFB AL 36112-5564	1
COMMANDING OFFICER NAVAL AVIONICS CENTER LIBRARY D/765 INDIANAPOLIS IN 46219-2189	1
COMMANDING OFFICER NCCOSC ROTE DIVISION CODE 02748, TECH LIBRARY 53560 HULL STREET SAN DIEGO CA 92152-5001	1
CMOR NAVAL WEAPONS CENTER TECHNICAL LIBRARY/C3431 CHINA LAKE CA 93555-6001	1
CDR, U.S. ARMY MISSILE COMMAND REDSTONE SCIENTIFIC INFO CENTER AMSMI-RD-CS-R/ILL DOCUMENTS REDSTONE ARSENAL AL 35898-5241	2
ADVISORY GROUP ON ELECTRON DEVICES ATTN: DOCUMENTS 2011 CRYSTAL DRIVE, SUITE 307 ARLINGTON VA 22202	2
REPORT COLLECTION, RESEARCH LIBRARY MS P364 LOS ALAMOS NATIONAL LABORATORY LOS ALAMOS NM 87545	1

COMMANDER/USATSC 1
ATTN: ASDP-DD-TL
BLDG 61801
FT HUACHUCA AZ 85613-5000

SOFTWARE ENGINEERING INST (SEI) 1
TECHNICAL LIBRARY
5000 FORBES AVE
PITTSBURGH PA 15213

NSA 1
ATTN: D. ALLEY
DIV X911
9800 SAVAGE ROAD
FT MEADE MD 20755-6000

DDO 1
R31
9800 SAVAGE ROAD
FT. MEADE MD 20755-6000

DIRNSA 1
R509
9800 SAVAGE ROAD
FT MEADE MD 20775

DEFENSE TECHNOLOGY SEC ADMIN (DTSA) 1
ATTN: STTD/PATRICK SULLIVAN
400 ARMY NAVY DRIVE
SUITE 300
ARLINGTON VA 22202

Rome Laboratory
Customer Satisfaction Survey

RL-TR-_____

Please complete this survey, and mail to RL/IMPS,
26 Electronic Pky, Griffiss AFB NY 13441-4514. Your assessment and
feedback regarding this technical report will allow Rome Laboratory
to have a vehicle to continuously improve our methods of research,
publication, and customer satisfaction. Your assistance is greatly
appreciated.

Thank You

Organization Name: _____(Optional)

Organization POC: _____(Optional)

Address: _____

1. On a scale of 1 to 5 how would you rate the technology
developed under this research?

5-Extremely Useful 1-Not Useful/Wasteful

Rating_____

Please use the space below to comment on your rating. Please
suggest improvements. Use the back of this sheet if necessary.

2. Do any specific areas of the report stand out as exceptional?

Yes___ No_____

If yes, please identify the area(s), and comment on what
aspects make them "stand out."

3. Do any specific areas of the report stand out as inferior?

Yes___ No___

If yes, please identify the area(s), and comment on what aspects make them "stand out."

4. Please utilize the space below to comment on any other aspects of the report. Comments on both technical content and reporting format are desired.

***MISSION
OF
ROME LABORATORY***

Mission. The mission of Rome Laboratory is to advance the science and technologies of command, control, communications and intelligence and to transition them into systems to meet customer needs. To achieve this, Rome Lab:

- a. Conducts vigorous research, development and test programs in all applicable technologies;
- b. Transitions technology to current and future systems to improve operational capability, readiness, and supportability;
- c. Provides a full range of technical support to Air Force Materiel Command product centers and other Air Force organizations;
- d. Promotes transfer of technology to the private sector;
- e. Maintains leading edge technological expertise in the areas of surveillance, communications, command and control, intelligence, reliability science, electro-magnetic technology, photonics, signal processing, and computational science.

The thrust areas of technical competence include: Surveillance, Communications, Command and Control, Intelligence, Signal Processing, Computer Science and Technology, Electromagnetic Technology, Photonics and Reliability Sciences.